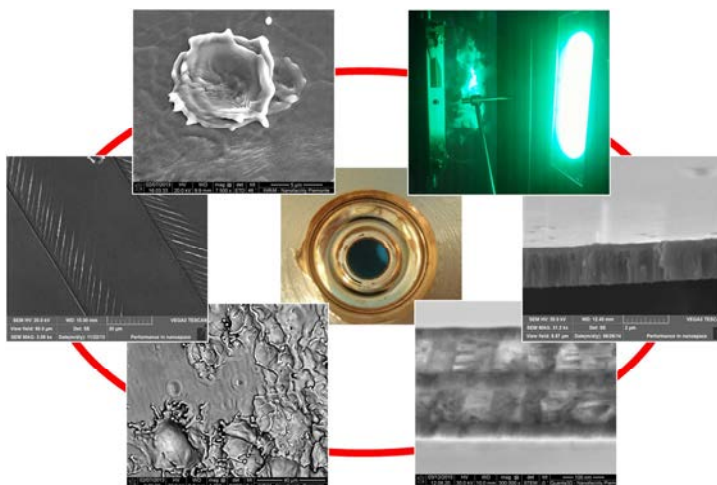




Doctoral School: Materials, Mechatronics and Systems Engineering

DEVELOPMENT OF MULTILAYER FOR PROTECTION FROM INTENSE ELECTRIC FIELDS

MATTEO CAMPOSTRINI



November 2017

DEVELOPMENT OF MULTILAYER FOR PROTECTION FROM INTENSE ELECTRIC FIELDS

MATTEO CAMPOSTRINI

E-mail: matteo.campostrini@unitn.it

Approved by:

Prof. Gianantonio Della Mea,
Department of Industrial Engineering
University of Trento, Italy.

Dot. Valentino Rigato,
National Institute of Nuclear Physics,
National Laboratory of Legnaro
Padua, Italy.

Ph.D. referee:

Prof. Gino Mariotto,
Department of Informatic
University of Verona, Italy.

Dot. Espedito Vassallo,
Institute of Plasma Physics
IFP-CNR Milano, Italy.

Ph.D. Commission:

Prof. Gian Domenico Sorarù,
Department of Industrial Engineering
University of Trento, Italy.

Dott.ssa Fabiana Gramegna,
National Institute of Nuclear Physics,
National Laboratory of Legnaro
Padua, Italy.

Prof. Ettore Vittone,
Department of Physics,
University of Torino, Italy.

University of Trento,
Department of Industrial Engineering

November 2017

**University of Trento - Department of
Industrial Engineering**

Doctoral Thesis

**Matteo Campostrini - 2017
Published in Trento (Italy) – by University of Trento**

ISBN: - - - - -

Alla Mia Famiglia...

Abstract

The experimental work presented in this thesis is done to develop an innovative procedure to create a protective nanostructured coating inside the X-band radio frequency cavity, a key component in future particle accelerator.

The scope of the multilayer coating is to prevent the breakdown due to high electric and magnetic field. In fact the electrical discharges damage, in irreversible way, the internal surface of the cavity and compromise the final operation of the device.

The keen interest on the topic is due to decrease the length and the cost of the next generation linear accelerator. To do this it is essential to enhance the performance of X-band Linacs up to 100MV/m accelerating gradient and to maintain, high as possible, the electrical breakdown reliability.

Several studies are made on different materials in order to develop these cavities [1] [2], but the use of physical vapor deposition technique (PVD), to obtain nanostructured coating directly on internal wall of these small sized cavities is not reported in literature.

The size of the cavities is of order of few millimeters and the iris aperture ranges from 2 to 6mm: for this reason the direct PVD coating is not possible. Hence a mandrel, that is the negative shape of the cavity, is first coated using PVD technique and finally chemically dissolved after copper electroforming[3].

The novel nanostructured coating is a multilayer composed by two high purity and immiscible metals. One is Copper to guarantee electrical conductivity of the cavity and the second is Molybdenum because it is a refractory metal. Moreover the choice of immiscible materials is important, because these materials do not form alloy during the deposition phase.

Keeping a well-defined interface is important to guarantee a barrier effect to the motion of the defects inside the cavity's material[4][5].

The experimental part of the thesis is divided in three different parts: design and setup of the PVD deposition system, plasma discharge analysis and, finally, the characterization of the coatings.

This work is a collaboration between Industrial Engineering Department (University of Trento) and the National Laboratory of Legnaro (National Institute of Nuclear Physics LNL-INFN), but this research involves several institutes in different countries: SLAC (USA), KEK (Japan) and UCLA (Los Angeles USA).

Table of contents

Abstract	V
Table of contents	VII
List of Figures	XI
List of Tables	XIX
I Chapter I	21
X-band linear accelerator	21
1.1 Application	23
1.1.1 CLIC (Compact Linear Collider)	23
1.1.2 Commercial applications	24
1.1.3 Medical applications.....	27
1.1.3.1 Inter-operative Radiation Therapy	27
1.1.3.2 Stereotactic Radiosurgery	28
1.1.3.3 Photonuclear reaction of radioisotope production	29
1.1.3.4 X-ray medical diagnostic and treatment	30
1.2 X-band cavity production technology: state of art 31	
1.3 X-band cavity: problems and failure	35
1.3.1 High cycle fatigue.....	35
1.3.2 Thermal fatigue caused by RF pulsed heating	39
1.3.3 Surface damage caused by thermal fatigue in RF	
component.....	42
1.3.4 Breakdown phenomenon in RF cavity	44
1.3.5 Protective nanostructured multilayer coating	51
II Chapter II	55
PVD Magnetron Sputtering	55
2.1 PVD Magnetron sputtering technique	55
2.2 HiPIMS technique	60
2.2.1 HiPIMS power supply.....	62

2.2.2	HiPIMS discharge	64
2.2.3	HiPIMS deposition rate	71
2.2.4	HiPIMS coating feature	76
2.2.4.1	Effect on film densification and microstructure ..	76
2.2.4.2	HiPIMS coating on complex geometry substrate	77
2.2.4.3	HiPIMS substrate pretreatment	78
III	Chapter III	80
	Cavity iris inspection	80
3.1	Overview	80
3.2	Results	81
3.2.1	Iris thermal fatigue damage	81
3.2.2	Iris breakdown damage	86
IV	Chapter IV	90
	Chamber setup	90
4.1	PVD Deposition Chamber	90
4.2	Mechanical component design	94
4.2.1	Sample holder	94
4.2.2	Sample holder shaft	95
4.2.3	Shaft alignment component	99
4.2.4	Magnetron motion component	100
4.3	Bias circuit box	104
V	Chapter V	107
	HiPIMS discharge diagnostic	107
5.1	Instrumentation setup	107
5.2	Results	108
5.2.1	RC bias circuit	108
5.2.2	Copper target HiPIMS discharge characterization	112
5.2.3	Molybdenum target HiPIMS discharge characterization	126

VI	Chapter VI	142
	Optical Emission Spectroscopy in HiPIMS Discharge.	142
6.1	Introduction.....	142
6.2	Optical emission spectroscopy.....	144
6.2.1	OES Instrumentation setup	144
6.2.2	OES results.....	146
6.3	Instrumentation setup OES time resolved	154
6.3.1	OES time resolved setup.....	154
6.3.2	OES time resolved results.....	157
VII	Chapter VII	166
	Thin film characterization	166
7.1	Techniques.....	166
7.1.1	AFM analysis	166
7.1.2	SEM analysis	167
7.1.3	Rutherford backscattering spectrometry	169
7.2	Sample preparation and deposition parameters..	171
7.3	Single layer analysis results	178
7.4	Multilayer analysis results	182
7.4.1	Multilayer in first configuration.....	183
7.4.2	Multilayer in second configuration.....	187
7.4.2.1	Multilayer in second condition and low sample holder bias (-50V) results	190
7.4.3	Multilayer in second configuration and high bias (-100V)	199
7.4.4	Bias effect on coating, low and high voltage bias multilayer comparison	207
VIII	Chapter VIII	215
	Different Analysis Technique Correlation	215
IX	Chapter IX	220
	General conclusions and Future perspectives	220

References.....	224
X Appendix.....	239
10.1 Instrumentations Details	239
10.1.1 PVD sputtering chamber	239
10.1.2 Pumping system	239
10.1.3 Power supply.....	239
10.1.4 Pressure Gauge	240
10.1.5 Optical emission spectroscopy.....	240
10.1.6 Discharge diagnostic	240
10.1.7 Thin film analysis instrumentation.....	241
10.2 Binning software	241
<i>Publications on peer reviewed journals</i>	267
<i>Participation to congresses, schools and workshops</i>	268

List of Figures

Figure I-1. Accelerating field limits	21
Figure I-2. CLIC linear collider final layout	23
Figure I-3. Cost of Circular & Linear Accelerators.....	24
Figure I-4. Example of commercial X-ray scanner [16].....	25
Figure I-5. Example of commercial portable X-ray scanner [16].....	25
Figure I-6. Linac and Array set-up X-ray scanner.....	26
Figure I-7. Example of cargo X-ray image.....	26
Figure I-8. Mobetron (Intraop).....	27
Figure I-9. Cyberknife (Accuray).....	28
Figure I-10. normal production (1); linac distributed production (2)[23]....	29
Figure I-11. Hard X-ray source a); Bremsstrahlung X-ray source b) [24]... 30	
Figure I-12. Single cell a)[27]; Assembled cavity b)[26].....	31
Figure I-13. Diamond turning mandrel, before a); after b) gold coating	32
Figure I-14. Electroforming technique [26].....	33
Figure I-15. Comparison of different materials [28]	34
Figure I-16. typical σ -log(N) Diagram.....	35
Figure I-17. Schematic Coffin–Manson type fatigue life diagram of copper [35].....	37
Figure I-18. Scheme of (a) initial state, (b) early stage of surface roughening and (c) PSB formation and crack initiation [35].....	37
Figure I-19. Nishijima and Kanazawa concept of twofold S–N curve [36]	38
Figure I-20. One-dimensional model of pulse heating	40
Figure I-21. Not constrained heated element deformation [41].....	41
Figure I-22. examples of different type of PBS [47]	42
Figure I-23. examples of PSB at grain boundary [45].....	43
Figure I-24. examples of PSB at grain boundary [49].....	43
Figure I-25. a) PSB with micro-cracks at the base; b)crack at grain boundary [50].....	44
Figure I-26. Field emission power flow distribution close to a tip [57].....	45
Figure I-27. Schematic of the power flow balance through the tip, in field emission electron "dark current" [57].....	46
Figure I-28. classical breakdown scenario [59].....	47
Figure I-29. a) Large melted area; b) Taylor cone structur [59]	47
Figure I-30. Electromigration breakdown scenario [59].....	48
Figure I-31. number of accumulated breakdowns vs number of pulses [54] 49	
Figure I-32. BDR gradient dependence a) [43]; and material b) [43].....	50
Figure I-33. a)BDR shape dependence; b)cavity shape profile [67].....	50

Figure I-34. a) Iris damage in tested cavity with relative Poynting vector and electric field; and b) SEM image [43]	51
Figure I-35. Relation between strength and grain size in polycrystalline materials [70]	52
Figure I-36. a) micron-scale, dislocation pile-up; b) nano-scale dislocation distribution [4].....	53
Figure I-37. probability of failure in different samples [5].....	54
Figure II-1. Schematic representation of sputtering process [71].....	55
Figure II-2. Circular magnetron sputtering source layout and relative electron race-track [73].....	57
Figure II-3. Potential of plasma.....	57
Figure II-4. Ion impact effect [75].....	58
Figure II-5. Thornton's structure zone diagram for sputtering [78].....	59
Figure II-6. Structure zone diagram applicable to energetic deposition [86]62	
Figure II-7. HiPIMS power supply scheme [88][89].....	63
Figure II-8. Example of HiPIMS discharge [79] (Chemfilt R&D AB Sweden).....	63
Figure II-9. Different HiPIMS operation modes	64
Figure II-10. Fraction of metals ion [90].....	65
Figure II-11. a) Target voltage vs target peak current density in DC and HiPIMS and b) Ion saturation current vs peak target current [83].....	65
Figure II-12. Voltage and current vs. time from initiation of the pulse using different argon gas pressure (a) 0.5, (b) 2, (c) 10 and (d) 20 mtorr [95]	68
Figure II-13. Schematic representation of HiPIMS discharge. a is the probability of ionisation, b is the probability of return to the target, g is the secondary electron emission probability. The t and g subscript mean "target" and "gas" [91].....	68
Figure II-14. Extrapolation of expected rarefaction in HiPIMS discharge [73].....	70
Figure II-15. Representation of self-sustained HiPIMS discharge [73].....	71
Figure II-16. comparison between DC and HiPIMS deposition rate in some metal target, using same power average. The green dots are referred to HiPIMS/DCMS ratio [107]	72
Figure II-17. a) Sputtering Yield function of ion energy. example of Ar and self sputtering of Cu and Ti; b) self-sputter yield of some target materials [96]	73
Figure II-18. HiPIMS/DCMS deposition rate vs pulse length [108]	74
Figure II-19. Comparison of DCMS and HiPIMS deposition rate vs reactive gas flow [109].....	75

Figure II-20. SEM image of dcMS on top and SEM image with XRD patterns of HiPIMS films grown at different peak target current values [114].....	77
Figure II-21. Exemples of coating on complex shepe substrate. Deep groove (left) [116] and flank of cutting insert (right) [119].....	78
Figure II-22. a)Metal implantation profile [120]; b)adhesion comparison [87]	79
Figure III-1. Pictures of analized X-band cavity iris [32].....	80
Figure III-2. Surface damage grain boundaries exposure (INFN-LNL)	81
Figure III-3. Grain boundaries exposure (INFN-LNL) refered to Figure III-2	81
Figure III-4. Different surface damage (INFN-LNL), various defects a); crack b).....	82
Figure III-5. Large melted area (INRIM)	83
Figure III-6. Large melted area close to grain boudary	83
Figure III-7. Rughnessinduced by PSB growth (INRIM).....	84
Figure III-8. Rughnessinduced by PSB growth (INRIM).....	84
Figure III-9. Bulk material defect, SE image a) and c); ion image b); BSEimage d) (INRIM)	85
Figure III-10. Wide field a) and melted area b) (INRIM).....	86
Figure III-11. Melted area by electrical discharge(INFN-LNL)	86
Figure III-12. Exemple of melted spots type 1 INRIM a) INFN-LNL b)....	87
Figure III-13. exemple of localized hot spot type 2 (INRIM)	87
Figure III-14. Type 2 defect inspection befor a) and afterFIB erosion (INRIM)	88
Figure III-15.Type 2 defect inspection befor a) and afterFIB erosion (INRIM)	88
Figure III-16. overlapping of type 2 defects (INRIM).....	89
Figure IV-1. Deposition chamber	90
Figure IV-2. Deposition chamber design	91
Figure IV-3. Main subsystem design for HiPIMS deposition	93
Figure IV-4. gettering subsystem	93
Figure IV-5. final sample a) and sample holder b).....	94
Figure IV-6. Design of upper half shaft	96
Figure IV-7. Bias external block connection design.....	97
Figure IV-8. Bias internalblock connection design	97
Figure IV-9. Final upper half shaft.....	98
Figure IV-10. Final lower half shaft.....	98
Figure IV-11. Allignment component design a) and reletive mechanical component assembled under the chamber b).....	99
Figure IV-12. Static magnetron holder extended flange.....	100

Figure IV-13. magnetron motion component in retracted configuration. Distance magnetron-sample holder 21cm.....	101
Figure IV-14.magnetron motion component in extracted configuration. Distance magnetron-sample holder 6cm.....	102
Figure IV-15.Completex magnetron motion component, just finisced and assembled on chamber.....	103
Figure IV-16. Bias circiute scheme	105
Figure IV-17. realized bias circuit with DC power supply	106
Figure V-1. Electrical Monitoring scheme	108
Figure V-2. Bials voltage recovery between two pulses using two capacitors	110
Figure V-3.Bials voltage recovery between two pulses using three capacitors	111
Figure V-4. Bias voltage recovery.....	111
Figure V-5. Cu discharge HiPIMS voltage a) and current b) and corresponding sample holder pick-up voltage b) and current d) with 210mm sample-magnetron distance	113
Figure V-6. Cu discharge HiPIMS voltage a) and current b) and corresponding sample holder pick-up voltage b) and current d) with 150mm sample-magnetron distance	114
Figure V-7. Cu discharge HiPIMS voltage a) and current b) and corresponding sample holder pick-up voltage b) and current d) with 110mm sample-magnetron distance	115
Figure V-8. Pulse Energy [J] for different configuration referred to	117
Figure V-9 Magnetroncharge absorpion [mC] for different configuration referred to Table V-3.....	118
Figure V-10. Peak current density for different configurations.....	119
Figure V-11. Peak power density for different configurations	119
Figure V-12. sample holder current evolution as function of magnetron- sample distance. a) 750V and 50us pulse width; b) 750V and 75us pulse width; c) 750V and 100us pulse width;	120
Figure V-13. sample holder current evolution as function of magnetron- sample distance. a) 800V and 50us pulse width; b) 800V and 75us pulse width; c)800V and 100us pulse width;	121
Figure V-14. sample holder current evolution as function of magnetron- sample distance. a) 850V and 50us pulse width; b) 850V and 75us pulse width; c) 850V and 100us pulse width;	122
Figure V-15. Sample holder pulse charge absorpion in different related to configuration	123
Figure V-16.Sample holder pulse charge absorpion related to HiPIMS pulse energy.....	123

Figure V-17. bombardment ion current density.....	125
Figure V-18. Mo discharge HiPIMS voltage a) and current b) and corresponding sample holder pick-up voltage b) and current d) with 210mm sample-magnetron distance	127
Figure V-19. Mo discharge HiPIMS voltage a) and current b) and corresponding sample holder pick-up voltage b) and current d) with 150mm sample-magnetron distance	128
Figure V-20. Mo discharge HiPIMS voltage a) and current b) and corresponding sample holder pick-up voltage b) and current d) with 110mm sample-magnetron distance	129
Figure V-21. Pulse Energy [J] for different configuration referred to Table V-6	132
Figure V-22. Magnetron charge absorption [mC] for different configuration referred to Table V-5.....	132
Figure V-23. Peak current density for different configurations	133
Figure V-24. Peak power density for different configurations.....	133
Figure V-25. Voltage pulse shapes related to different input Vac.....	134
Figure V-26. Current pulse shapes related to different input Vac	135
Figure V-27. Current pulse ignition time delay.....	135
Figure V-28. Sample holder current pickup configurations 1 a), 2 b), 3 c).....	136
Figure V-29 Sample holder current pickup configurations 4 a), 5 b), 6 c)	137
Figure V-30. Sample holder current pickup configurations 8 a), 9 b), 10 c)	138
Figure V-31. Sample holder current pickup configurations 11 a), 12 b), 13 c)	139
Figure V-32. Sample holder pulse charge absorption in different related to configuration	140
Figure V-33. Sample holder pulse charge absorption in different related to pulse energy	140
Figure V-34. bombardment ion current density.....	141
Figure VI-1. example of energy-level diagram of neutral helium a) and Bohr model b)[125].....	142
Figure VI-2. example of helium spectrum in visible range	143
Figure VI-3. OES scheme setup	145
Figure VI-4. OES copper spectra: HiPIMS a) and DC b).....	146
Figure VI-5. Coparation between DC and HiPIMS copper spectra.....	147
Figure VI-6. Range 1): CuI lines.....	148
Figure VI-7. Range 2): CuII and ArII lines	149
Figure VI-8. Range 3): CuII and ArI line	149
Figure VI-9. OES molybdenum spectra: HiPIMS a) and DC b).....	150

Figure VI-10. Coparation between DC and HiPIMS Molybdenum spectra	151
Figure VI-11. Range 1) MoI lines	152
Figure VI-12. Range 2) MoII lines.....	152
Figure VI-13. Range 3) ArII and MoI lines.....	153
Figure VI-14. Range 4) ArI lines	153
Figure VI-15. OES time resolved setup.....	155
Figure VI-16. Events recordered by digitizer (left) and the final OES-TR spectra after data processing (right).....	156
Figure VI-17. Example of electrical curves aquired for OES time resolved post processing, the “dt” time delay is determine by the SCA (single channel analyzer) treshold.....	158
Figure VI-18. OES time resolved of Copper HiPIMS discharge close to sample holder, distance 11cm, binning time 2 μ s.....	159
Figure VI-19. OES time resolved of Copper HiPIMS discharge close to sample holder, sample-magnetron distance 21cm, binning time 2 μ s	160
Figure VI-20.OES time resolved of Copper HiPIMS discharge close to magnetron, sample-magnetron distance 21cm, binning time 2 μ s.....	161
Figure VI-21.OES time resolved of Molybdenum HiPIMS discharge close to sample holder,sample-magnetron distance 11cm, binning time 2 μ s .	162
Figure VI-22. OES time resolved of Molybdenum HiPIMS discharge close to sample holder, sample-magnetron distance 21cm, binning time 2 μ s	163
Figure VI-23.OES time resolved of Molybdenum HiPIMS discharge close to magnetron, sample-magnetron distance 21cm, binning time 2 μ s.....	164
Figure VII-1. AFM layout.....	167
Figure VII-2. SEM layout	168
Figure VII-3. Exmple of nuclear interaction, M_1 is the projectile particle (primary ion beam), M_2 is the semple atom.....	169
Figure VII-4. Sample pretreatment effect on Mo coating,	172
Figure VII-5. Sample holder assembly.....	173
Figure VII-6.Real Groove profile and relative mockup with investigated points.....	173
Figure VII-7. Mockup deassembled with sample	174
Figure VII-8. Copper and Molybdenum sputtering yield [136].....	176
Figure VII-9. Example of Arc damage on Copper coating(Tescan).....	177
Figure VII-10. Exemple of Copper single layer coating morphology and profile.....	178
Figure VII-11. Exemple of Molybdenum single layer coating morphology and profile	178

Figure VII-12. a)Copper and b)Molybdenum single layer coating morphology 3D immages	179
Figure VII-13. a)Copper and b)Molybdenum single layer coating cross section (Tescan).....	179
Figure VII-14. Example of Copper Molybdenum bi-layer coating cross section. a) external rough surface; b)smooth coating-substrate surface. 1.4 μ m thick (Tescan).....	180
Figure VII-15.Example of Copper Molybdenum bi-layer coating cross section. 1.4 μ m thick (Tescan)	180
Figure VII-16.a)Copper and b)Molybdenum single layer coating RBS spectra	181
Figure VII-17. RBS spectra of coated vertical wall, measured in different point (referref to Figure VII-6).....	183
Figure VII-18. Oxygen contamination in coating 2mm position.....	184
Figure VII-19. nanostructured multilayer in external position	185
Figure VII-20. RBS spectra after Titanium gettering subsystem installation	189
Figure VII-21.Example penta-layer design	189
Figure VII-22. AFM profile measurement of coating with low sample holder bias	190
Figure VII-23.AFM morphology of coating with low sample holder bias	190
Figure VII-24. STEM sample preparation, a) and b) sample erosion with Ga-ion beam; c) and d) plate handling	191
Figure VII-25. Cross section STEM image of low bias multilayer sample	192
Figure VII-26. Cross section STEM image of low bias multilayer sample	192
Figure VII-27. RBS spectra of – 50V biased sample groove wall.....	194
Figure VII-28.RBS spectra of – 50V biased groove bottom.....	195
Figure VII-29.RBS spectra of – 50V biased of expernal posion	195
Figure VII-30. Layer thickness profile on groove vertical wall (-50V).....	196
Figure VII-31. Layer thickness profile onto the groove bottom (-50V) ...	198
Figure VII-32.AFM profile measurament of coating with high sample holder bias	199
Figure VII-33.AFM morphology of coating with high sample holder bias	200
Figure VII-34. Cross section STEM image of high bias multilayer sample	200
Figure VII-35.Cross section STEM image of high bias multilayer sample	201
Figure VII-36.RBS spectra of – 100V biased sample groove wall.....	202
Figure VII-37. RBS spectra of – 100V biased groove bottom.....	203
Figure VII-38. RBS spectra of – 100V biased of expernal posion	203
Figure VII-39. Layer thickness profile on groove vertical wall (-100V)...	204
Figure VII-40. Layer thickness profile onto the groove bottom (-100V) ..	205

Figure VII-41. External point RBS spectra	207
Figure VII-42. RBS spectra of 2mm and 4mm on groove wall	208
Figure VII-43. RBS spectra of 6mm and 8mm on groove wall	209
Figure VII-44. Molybdenum layers vertical wall thickness	211
Figure VII-45. Copper layers vertical wall thickness profile.....	211
Figure VII-46. Molybdenum layers groove bottom thickness profile	213
Figure VII-47. Copper layers groove bottom thickness profile	213
Figure VIII-1. Different solution of eq.VIII-3) relative to low bias deposition	218
Figure VIII-2. The relative flux composition of singly and doubly ionized Ar and Ti from the HIPIMS plasma [140].....	219

List of Tables

Table II-1. work function, first and second ionization energy of some metals and Argon [96]	69
Table V-1. Resitors configuration with two capacitors	109
Table V-2. Resitors configuration with three capacitors	109
Table V-3. Different power supply parameters and distance configurations	116
Table V-4. Pulse energy [J] for each measure configuration.....	116
Table V-5. Different power supply used for different configurations	130
Table V-6. Pulse energy [J] for each measure configuration.....	131
Table VI-1. Power supplies parameter for copper OES mesuraments.....	146
Table VI-2. Power supplies parameter for Molybdenum OES mesuraments	150
Table VII-1. pretreatment parameters	171
Table VII-2. Copper and Molybdenum HiPIMS power supply parameters	175
Table VII-3. Summary of single layer characteristics	181
Table VII-4. Interest points coating layer thickness	186
Table VII-5. Copper and Molybdenum layer thickness [atoms/cm ²] groove vertical wall position (-50V)	196
Table VII-6. Copper and Molybdenum layer thickness [nm] groove vertical wall position (-50V)	197
Table VII-7. Copper and Molybdenum layer thickness [atoms/cm ²] onto groove bottom (-50V).....	198
Table VII-8. Copper and Molybdenum layer thickness [nm] onto groove bottom	199
Table VII-9. Copper and Molybdenum layer thickness [atoms/cm ²] groove vertical wall position (-100V)	204
Table VII-10. Copper and Molybdenum layer thickness [nm] groove vertical wall position (-100V)	205
Table VII-11. Copper and Molybdenum layer thickness [atoms/cm ²] onto groove bottom (-100V).....	206
Table VII-12. Copper and Molybdenum layer thickness [nm] onto groove bottom (-100V).....	206
Table VII-13. Layer thickness of external point.....	208
Table VII-14. Multilayer Low Bias (-50V) groove wall layer thickness..	209
Table VII-15. Multilayer high Bias (-100V) groove wall layer thickness..	210
Table VII-16. Multilayer Low Bias (-50V) groove bottom layer thickness	212

Table VII-17. Multilayer Low Bias (-100V) groove bottom layer thickness
..... 212

Chapter I

X-band linear accelerator

Since the 80's the development of Normal Conducting (NC) X-band technology for particle accelerators has made significant progress.

The interest of scientific community, on construction of a Multi-TeV electron Linear Collider with reasonable size and cost, drives firstly this field of research. At the same time, a technological transfer of these devices is applied to the common application in security and medical fields.

The advancement of the new generation of X-band linear accelerators is demanded to achieve high accelerating gradients and at the same time to obtain a high reliability.

Improve the acceleration gradient is necessary to realize new type of portable devices and compact accelerator.

Based on Palmers diagram [6], here is reported the state of art about X-band cavities accelerating gradient.

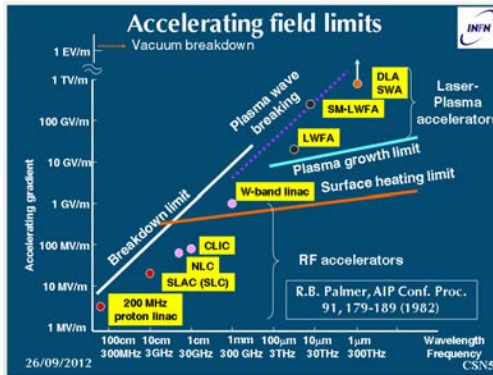


Figure I-1. Accelerating field limits

As shown (Figure I-1) the principal limitations, about RF accelerator technology, are the breakdown and surface heating. In the most of

prototype, the theoretical limit isn't achieved due to intrinsic material problems of the device.

In order to achieve, close as possible, to these limits is necessary an original improvement of the device.

In this chapter will be describe the applications of x-band accelerators, the state of art of cavities manufacturing, the reason of surface damages formation and finally the breakdown discharges ignition and the relative damages.

1.1 Application

1.1.1 CLIC (Compact Linear Collider)

CLIC is the newer linear accelerator developed at CERN. The target of this linear accelerator is reach 3 TeV center-of-mass energy. Such as suggest by the name, the aim of this accelerator is provide elementary particles collision, between electron and positron, in order to obtain detailed information about new particles produced by their annihilations[7][8][9].

This accelerator is a modular project and will be built in three different step, 500 GeV, 1.2 TeV and finally 3 GeV, using high performance (100 MV/m) normal conductivity X-band cavities.

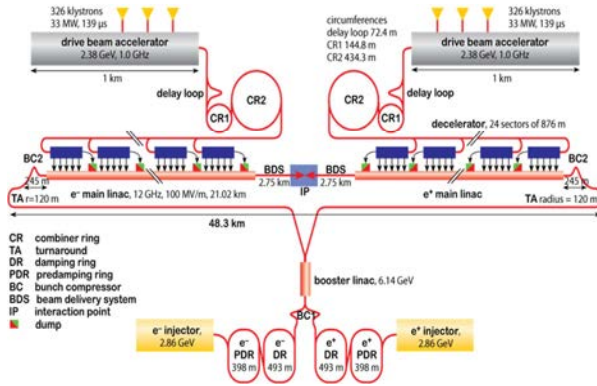


Figure I-2. CLIC linear collider final layout

A linear collider (Figure I-2) essentially is composed by two opposed linear accelerator, whose beams collide in the experimental rooms at the center of the facility.

The main reason to prefer a linac to a circular accelerator (LHC) is due to the building and operation costs[10].

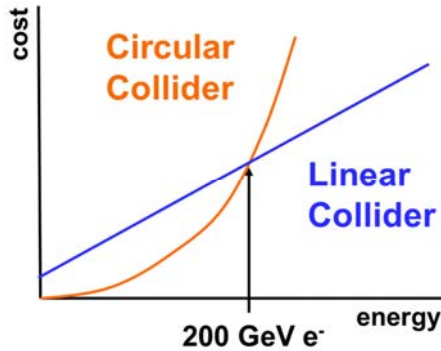


Figure I-3. Cost of Circular & Linear Accelerators

The non-linear trend cost/energy of the circular collider is due to synchrotron radiation losses.

In the linear collider the cost/energy trend, except the initial cost, is linear. The increment of the cost is proportional to the energy and then to the length of the accelerator.

In CLIC was decided to use 12 GHz normal conducting copper cavities with 100 MV/m accelerating gradient, but nowadays there are other cavity designs with higher performance[11].

In Figure I-2, is reported the length of entire linac structure, nearly 50Km. Using cavities with high acceleration gradient can reduce the length of beam line, that means reduce the cost.

1.1.2 Commercial applications

Nowadays compact low energy linear accelerators and portable accelerator devices are commonly used in several applications, like nondestructive testing[12][13] or security controls[14]. In these devices, a X-rays beam is produced by the electrons impact on a high Z target, such as Tungsten. Moreover it's possible obtain gamma or neutron source[15], changing the target material (Cobalt, Iridium, Cesium, Beryllium, Lithium...).



Figure I-4. Example of commercial X-ray scanner [16]



Figure I-5. Example of commercial portable X-ray scanner [16]

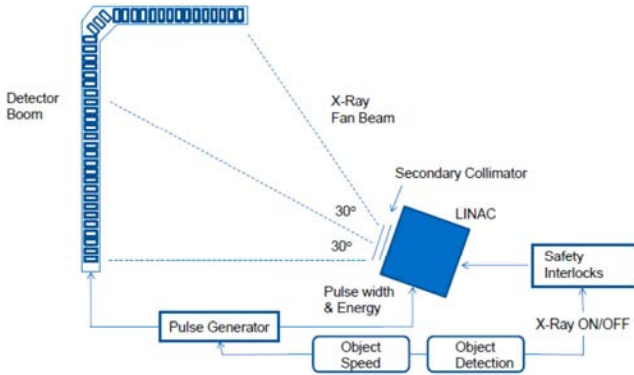


Figure I-6. Linac and Array set-up X-ray scanner

The use of X-band cavity accelerator allows to scale down the electron source system and in same time increase the light intensity. Use high energy electrons, usually in a range 1 to 20 MeV [17], permits also to analyze large component, such as train, TIR and boat cargo in steady way or in movement [18][19].

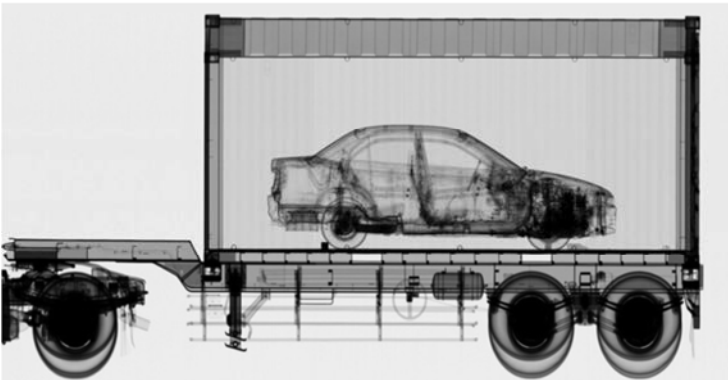


Figure I-7. Example of cargo X-ray image

1.1.3 Medical applications

In the last two decades different devices based on X-band accelerator technology were developed for medical applications.

Mainly there are four different fields:

- Inter-operative Radiation Therapy (IORT) [17][20][21]
- Stereotactic Radiosurgery [17][20][22]
- Radioisotope production [23]
- X-ray medical diagnostic and treatment [24]

1.1.3.1 *Inter-operative Radiation Therapy*

The Inter-Operative Radiation Therapy device uses the release of radiation during an operation using an electron beam.

It has been proven that, this radiation therapy technique increases the survival rates in certain cancer cases.

Generally the old radiation therapy devices are bulky and must be housed in special shielded rooms. That means the patient has to be moved from the operating room in the accelerator room for therapy.

Using a mobile radiation therapy machine, like Mobetron (Intraop) [21], that use X-band cavity technology, it is possible to use the device directly in operating room and treat the cancerous with better precision, moreover the self-shielded structure of the device doesn't need a shielded special room.



Figure I-8. Mobetron (Intraop)

1.1.3.2 Stereotactic Radiosurgery

Stereotactic Radiosurgery is a device that use X-ray radiation to cure tumor directly (ex. “Cyberknife” Accuray) [22].

It uses X-ray high power beam with small spot size, to irradiate the patient at different angles, in order to minimize damage to healthy tissue and get a great focus on the target (tumor).

This therapy has good performance, because the treatment spot is continuous monitored using an X-ray stereoscopic system and led applied on the patient's body. These stereoscopic system permits the monitoring the position of tumor during the patient's breathing and automatically compensate his movements.

The X-band cavity accelerator technology is used for the same reasons of IORT device, because it permits safer and light device, in order to facilitate the positioning and handling.



Figure I-9. Cyberknife (Accuray)

1.1.3.3 Photonuclear reaction of radioisotope production

Nowadays the majority of medical isotopes are produced in the nuclear plant by fission process.

This technique basically has the problem of great amount of the radioactive waste production.

In the last years the number of nuclear plants able to produce medical radioisotopes is decreased, due to a change of political energy program or because the nuclear plant has achieved its time life.

Moreover the request forecast of most used radioisotope for medical treatment (Technetium-99m), grows in order of 15% every ten years [25].

In response to the request of this radioisotope increase, it was propose the photonuclear reaction technique using electron linear accelerator.

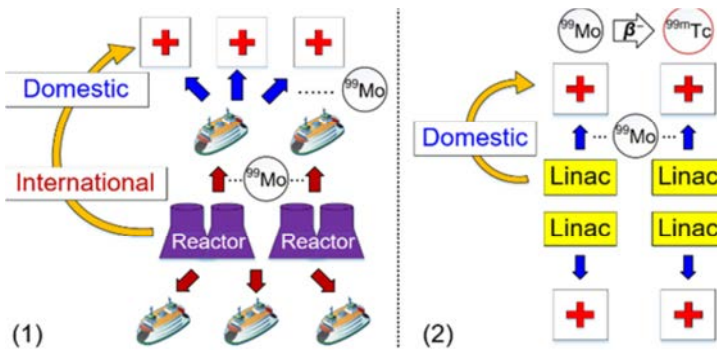


Figure I-10. normal production (1); linac distributed production (2)[23]

Furthermore due to the short lifetime of these radioisotopes using X-band compact linear accelerator, It is possible to obtain the radioisotope directly in the hospital avoid the transport and the decay loses [23].

1.1.3.4 X-ray medical diagnostic and treatment

Another application of electron linear accelerator based on X-band cavity technology, it is the X-ray imaging analysis and treatments.

In this case the X-ray beam is produced using the Compton effect. Where the collision between electrons and laser photons produce a monochromatic hard X-ray beam, that is used for medical inspection, such as Intravenous Coronary Arteriography. Moreover using a target with high Z between the primary beam and the patient is possible produce an high energy Bremsstrahlung X-ray beam, and it is used directly on the patient for the therapy.

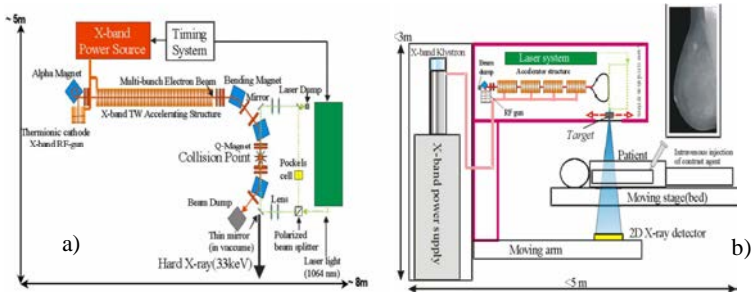


Figure I-11. Hard X-ray source a); Bremsstrahlung X-ray source b) [24]

1.2 X-band cavity production technology: state of art

The realization of X-band cavity isn't easy, due to the restricted geometrical tolerances.

Nowadays are used two different production techniques. The commonly used is the welding (brazing, or electron-beam). The second is the electroforming, but this technique is more complex and expensive.

Basically the choice between the different techniques is due to the accelerating gradient and then to the relative breakdown probability.

Higher accelerating gradient required higher mechanical precision and better surface finishing. This is the main discriminant in the choice of the production technique.

The brazing technology is the most used technology to produce this kind of device[26][27].

The cavity is produced in several parts by mechanical tools, assembled with clamps and finally brazed in a vacuum oven. With this technique is possible to obtain also cavity composed by different materials.



Figure I-12. Single cell a)[27]; Assembled cavity b)[26]

The second way to obtain a cavity is electroforming procedure.

This technique allows to obtain the final cavity in a single component without joints. The cavity is produced in four steps [26][3]:

- The mandrel, that is the negative shape of a cavity, and reproduces the void inside it. This is made by micrometer precision diamond turning and nanometer polishing; this particular machining permits to obtain very smooth surface with a roughness of tens nanometers range.

Generally the mandrel is made in aluminum, because it is easier to process by machine tools.

- The mandrel is coated by 100nm of gold using PVD technique, to prevent the copper corrosion from basic solution (step 4)
- The mandrel is immersed in an electrolytic bath that contains water, soluble copper salts and a copper electrode.

Applying a voltage between the two electrodes, negative voltage to the mandrel and positive to the copper electrode, the copper ions dissolved in the bath are attracted on the mandrel surface and form bulk cavity (some millimeters).

- Using a basic solution, usually sodium hydroxide (NaOH) the mandrel is dissolved.



Figure I-13. Diamond turning mandrel, before a); after b) gold coating

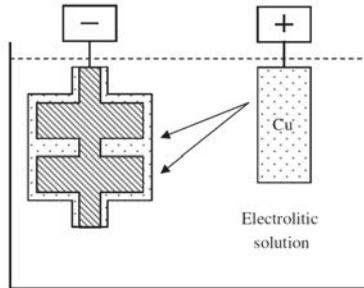


Figure I-14. Electroforming technique [26]

Another important parameter is the material that constitutes the component. The material must be a good electrical conductor in order to reduce the RF losses, thermal conductor to dissipate the RF heating, vacuum and high magnetic field compatible, and fatigue resistant.

Combine all these properties in only one material is practically impossible. For this reason different metals, alloys or engineered compounds were tested in the last decade.

From point of view of electrical and magnetic properties the best material is the oxygen free electronic copper (Figure I-15).

Nowadays OFE-Cu is the most used material to produce RF cavities, but unfortunately it isn't suitable for X-band due to low fatigue resistance. It is used in C-band or S-band, because those work at low frequency and have lower accelerating gradient. In the X-band the fatigue phenomena are very heavy and it is one of possible cause of the device.

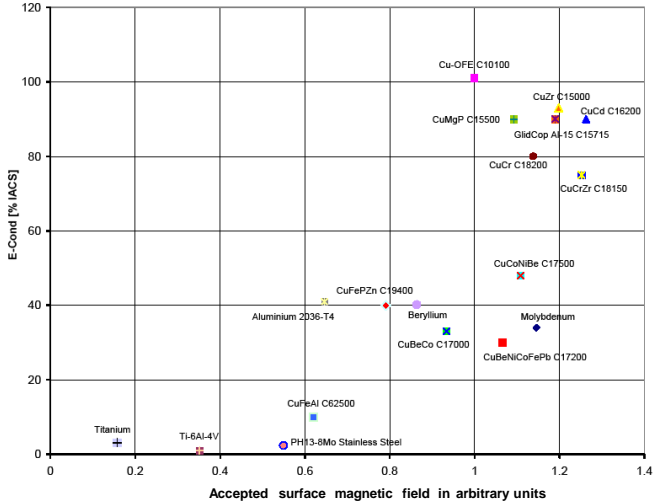


Figure I-15. Comparison of different materials [28]

Figure I-15 shows some pure metals and alloys (mainly Cu alloy) were studied in the past to understand their electromagnetic and mechanical properties [28]. The reason of these studies is understand the physical limitation of these materials in RF application, moreover some compounds [3] was ad hoc designed combine the weakness and the strengths, of different bulk materials, in order to improve the cavity characteristics. The other approach to improve the reliability of the X-band cavity is the surface property modification using engineered coatings. That permits to improve the surface resistance preserving the bulk properties [29][30][31][32].

1.3 X-band cavity: problems and failure

1.3.1 High cycle fatigue

The fatigue is the weakening of a material caused by cycle load. It is cause a progressive structural damage when a material is exposed to cyclic loading. Since the 18th century the fatigue mechanism was studied and proposed by August Wöhler (1819-1914). In his work he proposed a relation between the stress and life time of a component under cyclical load.

A typical stress-lifetime diagram represent the 50% failure probability of a component undergo a cyclical stress. It is possible distingue three different zone with different behavior (Figure I-16), oligo-cycle at low cycle frequency LCF (number of cycles lower 10^{3+4}), Wöhler behavior high cycle frequency HCF (number of cycles 10^{4+6}) and the sub-fatigue limit (SF) in the ultra-high fatigue cycle regime (higher 10^6 cycles).

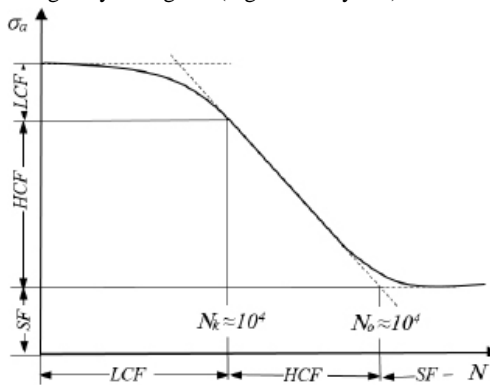


Figure I-16. typical σ - $\log(N)$ Diagram

Generally the most part of metals or alloys have a horizontal asymptotic trend at a defined value of σ_a , that means if the load applied is lower that value the lifetime of the component is infinite.

In the particular case of face-centered cubic structure (FCC) like aluminum, copper, their alloy and other similar materials the asymptotical behavior is

not present. The Wöhler curve value constantly decreases and the fatigue limit is not constant. This effect is due to an easier defects movement (lower energy threshold of shear planes) inside the material's crystal as reported in many textbooks e.g. [33].

Only in the last 50 years, thanks to the technological improvement, it became possible to investigate the behavior at number of cycle higher 10^6 . Using piezoelectric device the time of a fatigue test decrease significantly.

The fatigue phenomenon became very important in order to study the lifetime of specific components like car engine, high speed component, turbine and now for RF cavity.

The fatigue effect in ultrahigh fatigue cycle regime is described by Mughrabi (UHFC) [34][35]. In these works he investigates the physical process that lead to the failure in metals at UHFC regime.

In Figure I-17 is reported the Coffin-Madison fatigue diagram of copper, this diagram is similar to the Wohler diagram, unlike the abscissa unit. In fact the Coffin-Madison diagram is based on plastic deformation instead the stress amplitude.

He investigated the fatigue crack initiation in extended HFC regime, with stress below permanent slip band threshold (PSB), like irreversible slip step of dislocation glide at the surface. As a consequence about the irreversible accumulation of defects, a gradual roughening of surface occurs.

The intrusion and extrusion of the roughness became in second time a crack initiation (Figure I-18).

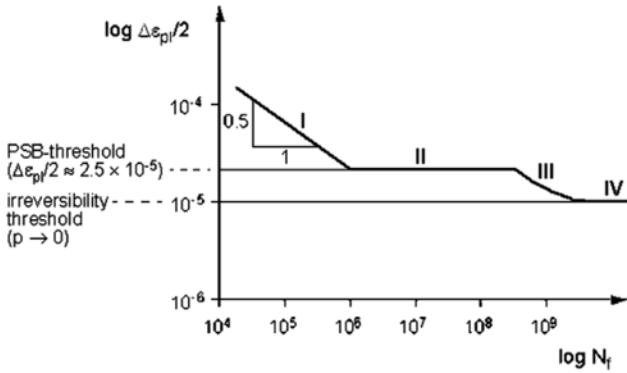


Figure I-17. Schematic Coffin–Manson type fatigue life diagram of copper [35]

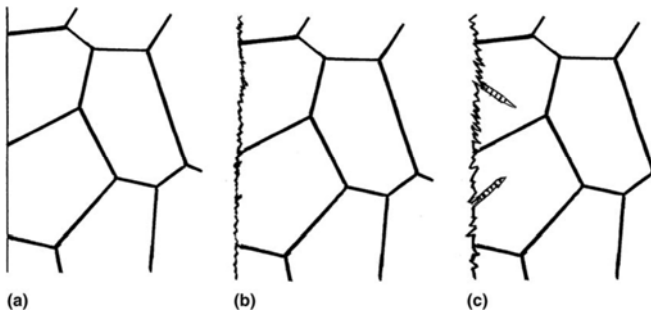


Figure I-18. Scheme of (a) initial state, (b) early stage of surface roughening and (c) PSB formation and crack initiation [35]

Analogously Nishijima and Kanazawa [36] published the Wohler diagram at high cycle regime.

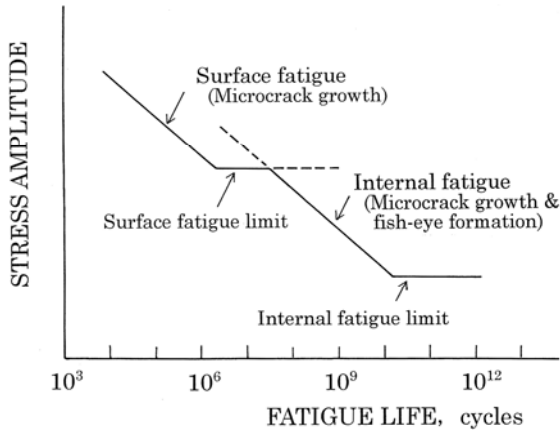


Figure I-19. Nishijima and Kanazawa concept of twofold S-N curve [36]

In Figure I-19 (similarly to Figure I-17) shows four behavior in different cycle range [37]:

- I. Finite fatigue life range, that extend the LCF to HFC, the crack start commonly at the surface
- II. Conventional HCF fatigue limit, that correspond to PSB threshold
- III. VHCF range, where the stress amplitude is below PSB threshold. The cracks start on the surface due to roughness (PSB accumulation) in defect-free ductile metals, or start from internal defects in materials with inclusion.
- IV. VHFC fatigue limit. The presence of this limit is until now debated. There are two theory, in the first Mughrabi (1999) suggest the presence of this limit where the slips are negligible or non-damaging. The second theory, Bathias (1999) suggest a continuously decreasing stress-life [38].

1.3.2 Thermal fatigue caused by RF pulsed heating

Thermal fatigue is a cycle fatigue induced by a cyclical thermal load. In the RF cavities the cyclical load is caused by ohmic heating in the RF skin layer [39], close to the surface. The heat is progressively transmitted, following the thermal diffusion law eq. I-1, to the bulk and dissipate.

$$\left(\frac{\delta\Delta T}{\delta t}\right) - \frac{\lambda_T}{C\rho} \left(\frac{\delta^2\Delta T}{\delta z^2}\right) = \left(\frac{\delta\Delta T}{\delta t}\right) - D \left(\frac{\delta^2\Delta T}{\delta z^2}\right) = 0 \quad \text{I-1}$$

Where λ_T is the heat conductivity, C is the heat capacity and ρ is the material density in one-dimensional approximation.

Assuming a rectangular electromagnetic pulse $q(t)$ with τ duration, the integration of the eq. I-2 define the maximum temperature reach:

$$\Delta T_{MAX} = \frac{2}{\sqrt{\pi}} \frac{q\sqrt{\tau}}{\sqrt{c\rho\lambda_T}} = \frac{2}{\sqrt{\pi}} \frac{\sqrt{D\tau}}{\lambda_T} q \quad \text{I-2}$$

δ_T is the thickness of the heated layer referred to the skin depth (Figure I-17):

$$\delta_T = \sqrt{D\tau} \quad \text{I-3}$$

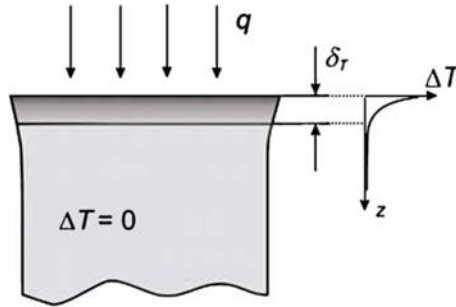


Figure I-20. One-dimensional model of pulse heating

In the particular case of surface heating caused by electromagnetic wave, it is possible to rewrite the eq. I-2 using the tangential component of magnetic field as heating source

$$\Delta T_{MAX} = \frac{1}{\lambda_T} \sqrt{\frac{D\tau}{\pi}} \sqrt{\frac{\mu_0 \omega}{2\sigma}} H_T^2 \quad I-4)$$

Where:

- μ_0 is the permeability of the vacuum,
- ω is RF frequency,
- σ is specific conductance of copper.

In a theoretical component, composed by a single element, the heated surface is not constrained and the element can freely deform (Figure I-21). Instead in a real component the surrounding material hinders the deformation and induces the mechanical stress [40][41].

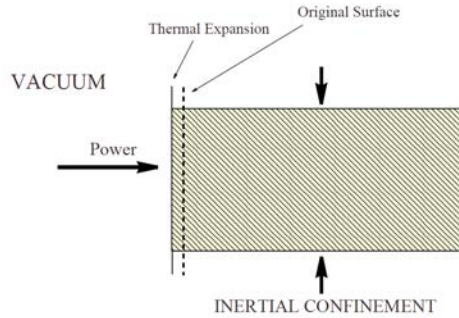


Figure I-21. Not constrained heated element deformation [41]

If it is assumed that the transversal dimension of the heated element is large enough to remain inert during the thermal cycle, the total transverse strain is zero. With the approximation of plane stress condition, the stress is compressive (eq. I-5) in transversal direction of normal plane (irradiated surface):

$$\sigma = -\frac{E\alpha\Delta T_{MAX}}{1-\nu} \quad \text{I-5)}$$

Where:

- σ is compressive stress
- E is elastic modulus
- α is thermal expansion coefficient
- ν is Poisson's ratio
- ΔT is maximum temperature rise

1.3.3 Surface damage caused by thermal fatigue in RF component

As describe in previous paragraphs, a component exposed to high fatigue regime suffer of irreversible surface damage, like cracks and roughness formation.

The damage propagation type in a device depends on several factors, such as material, surface finishing, size and orientation of the grains [42], intensity of irradiance power, cooling system, etc.

In a standard copper X-band cavity the stress causes two type of damage,

- 1) increment of surface roughness
- 2) grain boundary cracks

That depends of s intensity, repetition rate and duration of the RF pulses. Moreover the energy released is not uniform on all cavity's surface but is related to the electro-magnetic field intensity [43][44].

In VHFC regime the main type of damage observed is the roughness formation. Several studies in the last 20 year show the appearance of PSB on tested components [27] [28] [37] [44] [45][46][47][48][49].

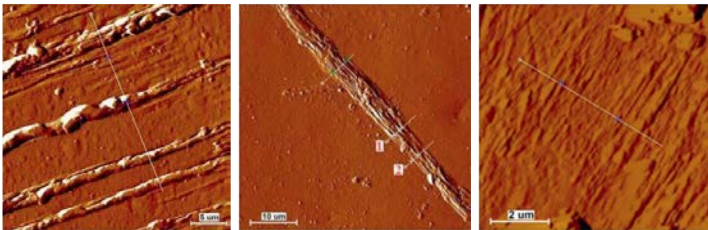


Figure I-22. examples of different type of PSB [47]

Generally PSB start from the grain boundaries, because the discontinuity of the lattice promotes the dislocation pile up, and consequently the roughness growth (Figure I-23, Figure I-24).

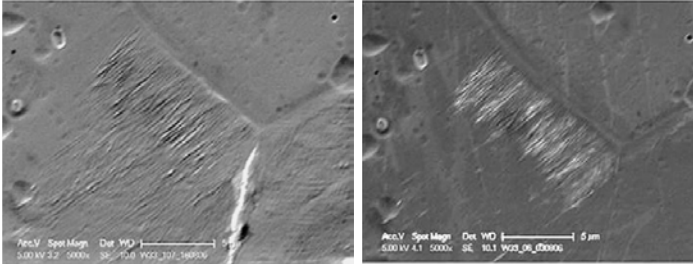


Figure I-23. examples of PSB at grain boundary [45]

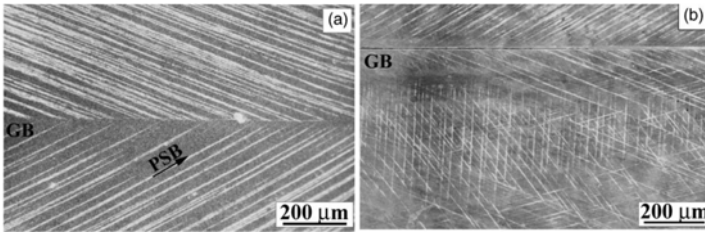


Figure I-24. examples of PSB at grain boundary [49]

The other damage caused by fatigue is the formation of cracks on the surface.

There are two different processes that cause this phenomenon, the first is due to the PSB growth (intra-granular crack), instead in the second process the crack start from a grain boundary (inter-granular).

In the intra-granular mode, the protrusion and extrusion of PSB induces a local concentration of stress, and consequently a crack nucleation [46][50].

In the inter-granular mode the crack start from grain boundary, this mechanism considers the probability of break (higher) and reconnection (lower) between atoms belonging to adjacent grains during a fatigue cycle [39][50][51].

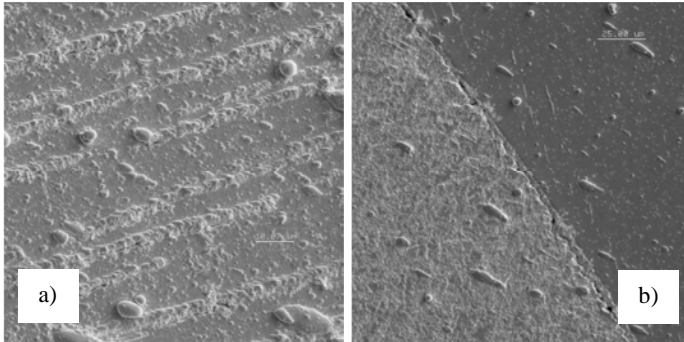


Figure I-25. a PSB with micro-cracks at the base; b) crack at grain boundary [50]

1.3.4 Breakdown phenomenon in RF cavity

The main limitation of the accelerating gradient is theoretical vacuum breakdown, as shown in Figure I-1; in all the tested cavities the maximum value in terms of accelerating gradient is lower to the theoretical one. This gap is due to the defects present in real components.

The breakdown is a catastrophic exchange of charge between two electrodes with a different potential, it manifests as local surface melting, craters, bubbles and holes.

The phenomena cause a shut off of the particles acceleration (the potential difference drop close to the ground value). This effect lasts some nanoseconds, moreover the light produced by the arc lasts several microseconds [52] and it may blind the diagnostic devices.

In last decade several studies were made to understand the correlation between the breakdown phenomena and the characteristics of the component (surface finishing, type of materials, production technique...) [3][53][54][54][55][56].

The discharge is ascribed to a non-homogenous surface, such as tips, powders, holes and oxide areas, roughness and so on.

These surface defects cause a variation of Poynting vector (Figure I-26) and then a localized anomalous absorption of power called dark current [57].

The Figure I-26 the arrows show the direction of Poynting vector whereas the color is proportional to the logarithmic value.

The local increase of the surface charge and the growth of Poynting vector modulus induce an electron emission [58] and consequent power loss (Figure I-26), this loss is called also “dark current”.

P_{FN} is the total power flow dissipates in the field emission process for OFEC:

$$P_{FN} = AE_0^3 \sin^3 \omega t \cdot \exp\left(\frac{-62}{\beta E_0 \sin \omega t}\right) \quad \text{I-6}$$

Where:

- P_{rf} is the initial RF power flow,
- P'_{rf} is the RF power flow transmitted
- P_{loss} in the power flow lose to heat the tip
- P_{FN} is power flow lose for field emission effect

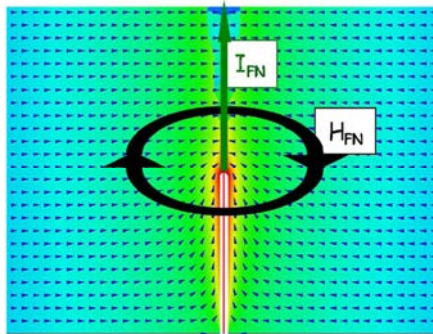


Figure I-26. Field emission power flow distribution close to a tip [57]

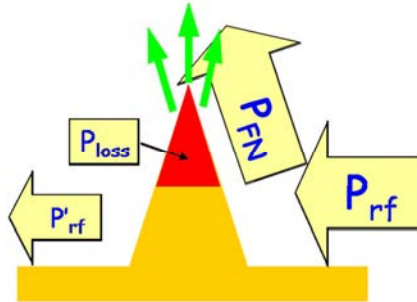


Figure I-27. Schematic of the power flow balance through the tip, in field emission electron "dark current" [57]

There are two different theories that explain the breakdown phenomenon. The first one supposes the defects are already present on the surface, like PSB crests, crack corners etc. Whereas the second theory considers a very smooth surface and it supposes the formation of roughness due to high electric field [59].

The classical breakdown phenomenon is more complex than the simply field emission electron (dark current) and involves different steps Figure I-28.

Starting from a surface defect, for example a tip, the electrons flow causes a local Joule heating. The high amount of energy coupled with electric field, induces consequently an emission of surface metal atoms [8][60][61].

The emitted metal atoms will be ionized by the field emitted electrons and forming a plasma cloud. The plasma sheath, between the plasma cloud and the cathode surface, increase the surface electric field and it promotes the ignition of close emission sites, destroying the original one. The erosion of original site, and after of neighbors, is due to the bombardment of metal ions that are accelerated to the anode. This process is known as sputtering [62].

This chain reaction is called "burning phase of the plasma" and can produce several and large craters [63].

The process continues until the external power provides enough energy to sustain the discharge.

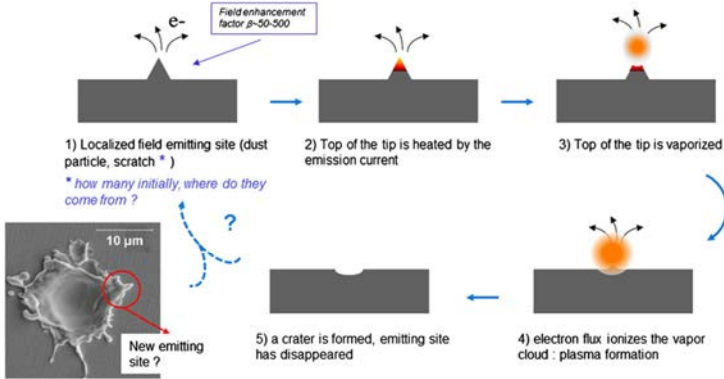


Figure I-28. classical breakdown scenario [59]

The second approach [59] was theorized in order to explain the large areas damaged RF cavities, those are inexplicable using the classical breakdown theory.

In fact in several tested cavities shown large melted areas and Taylor's cone structures, which are not correspond with classical breakdown damage [64][65].

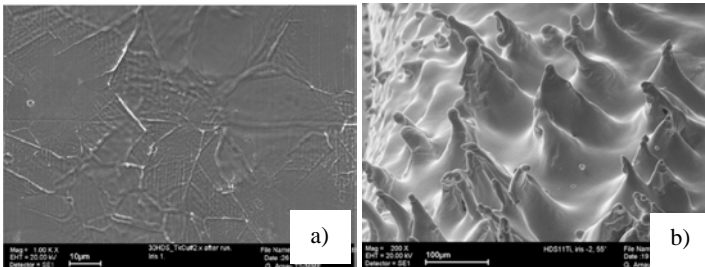


Figure I-29. a) Large melted area; b) Taylor cone structur [59]

In order to explain these particular phenomena, the concept of “capillary wave instability” has to be introduced.

The capillary wave instability is the conjunction of electromigration and collective effects under high electric field Figure I-30 [66].

Electromigration is the balance result between two opposite forces, the “electric wind” and the “direct force”.

The electric wind is the exchange of momentum from one charge carrier to another, as scattering of conduction electrons in the metal and momentum transfer of the moving metallic ion to other charge carriers, whereas the direct force is the action of the electric field applied on the charge of the moving metallic ion.

The surface and grain boundary atoms are weakly bounded, compared to bulk atoms. That means the diffusional activation energy is lower than in bulk material, and the movement of surface atoms is facilitated.

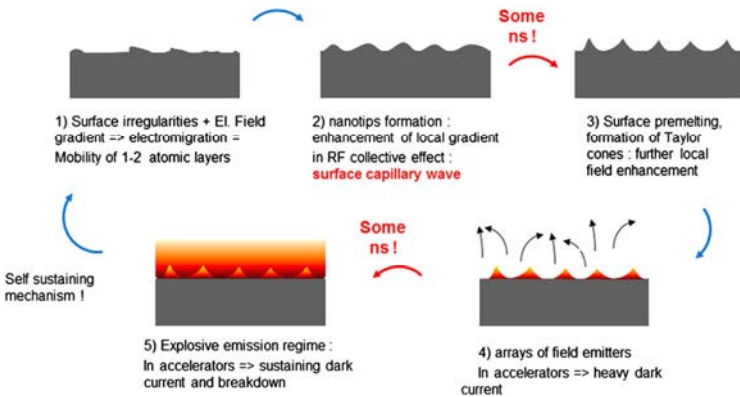


Figure I-30. Electromigration breakdown scenario [59]

In presence of small surface irregularity (nanometers are enough), the electric field gradient cause an electromigration of surface atoms and the formation of hillock and tips. All the tips growth from the capillarity wave are, like in the classical scenario, electrons emission source.

Unlike the classical scenario where the breakdown is caused from an only emission source, in this case there is a collective emission from all tips that cause a diffuse plasma discharge that melt the surface.

The type of damage, as shown in Figure I-29, depends in which stage the process is stopped.

To understand the final acceleration gradient capability of a cavity, it is necessary known its behavior at the different working steps.

Before to reach the work regimen, the cavity is undergone a conditioning treatment. In this phase, the RF power is applied gradually to the cavity without beam, in order to achieve the highest possible accelerating field at acceptable breakdown rate (BDR) without structure damage.

In addition, the conditioning is necessary to decrease the amount of surface defects or contaminations.

After the conditioning the BDR became stables (Figure I-31) and it depends basically from the pulse parameters, such as accelerating gradient, pulse duration and from cavity parameters like shape and materials (Figure I-32 and Figure I-33).

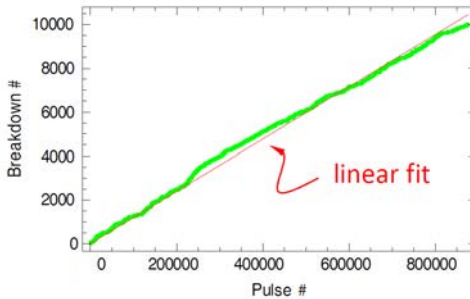


Figure I-31.number of accumulated breakdowns vs number of pulses [54]

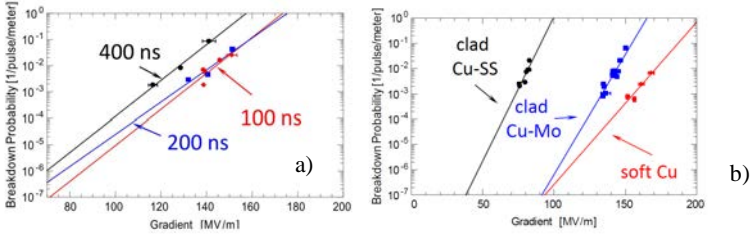


Figure I-32. BDR gradient dependence a) [43]; and material b) [43]

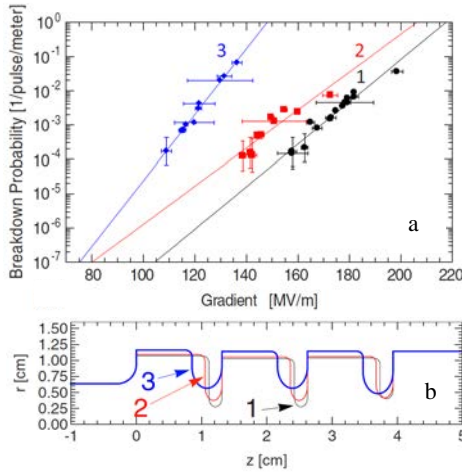


Figure I-33. a) BDR shape dependence; b) cavity shape profile [67]

The effect of BD on the cavity surface depends by the material and the cavity structure design. The BD is predominant close to iris aperture of the cavity, where the electric field is higher Figure I-34.

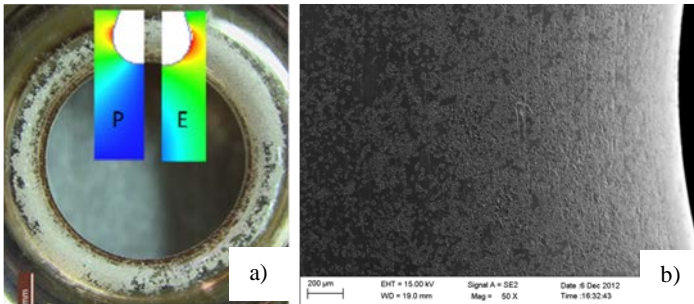


Figure I-34. a) Iris damage in tested cavity with relative Poynting vector and electric field; and b) SEM image [43]

1.3.5 Protective nanostructured multilayer coating

As describe in previous paragraphs in HVFC regime, the principal failure in smooth sample is the cracks surface formation, generally it starts from an irreversible surface roughness damage due to PSB appearance.

Commonly are used different approaches to improve the cracking resistance of bulk materials:

- 1) hardness: to prevent surface roughening,
- 2) ductility (toughness): to prevent cracking where PSBs intersect the surface,
- 3) cyclic work hardenability: to prevent slip formation,
- 4) residual compressive stresses: to reduce the tensile stresses magnitude
- 5) surface engineering: multilayer coating

The use of nanostructured and multilayer coatings is well established in the industry for tribological applications [68][69].

The interest of these multilayers has grown in recent years also in the field of high-frequency components, such as particle accelerators, engine components, for their different mechanical properties which differing from traditional bulk materials.

The standard metal materials, except amorphous, are composed by grain and the plastic deformation is due to the motion and formation of dislocations. With an amount of energy, there is the activation of slip plain inside the crystal and the consequential deformation. Moreover the presence of defects like lattice void, inclusion and grain boundaries induce the growth of dislocation density. One of parameter that manages evolution of this lattice's damages is the grain size Figure I-35 [70].

In nanostructured multilayer, the grain size is very smaller, then classical bulk materials, that means some plastic deformation process are denied or delayed.

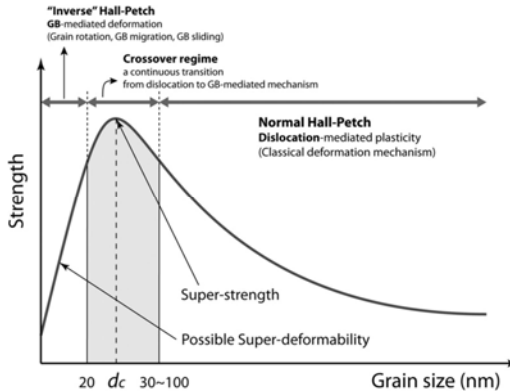


Figure I-35. Relation between strength and grain size in polycrystalline materials [70]

That shown in Figure I-35, a material has different behavior, as a function of the grain size.

At "big" grain size, greater than 100 nm, the process involved is the Hall-Petch mechanism. This is the classical deformation mechanism and the lower value of strength is caused by high mobility of dislocations inside the grain.

The Hall-Petch strengthening is commonly used to increase the material strength. Reducing the grain size there is an increasing of the grain

boundaries amount, these new surface obstacle the defect motion. A dislocation needs more energy to pass through grain boundary than the motion inside to the grain.

Decreasing the grain size, lower 20 nm, there is an inversion of strength trend called “inverse Hall-Petch strengthening”. The softening of material is due to activation of grain boundary-assisted deformation, generally the failure in this kind of materials is ascribe to grain boundaries sliding.

The crossover regime is between 20nm and 100nm. Where the grain can't accommodate multiple lattice dislocations, and it engages alternative plastic deformation mechanisms such as grain-boundary sliding; partial dislocation emission and absorption at grain boundaries.

In micron-scale or bigger material grain, there are more active glide planes and the dislocations can organize a pile-up structures and create PSB.

In nano-scale grain there are a low number of active glide plane, and the pile-up is limited to few dislocations not enough to create PSB.

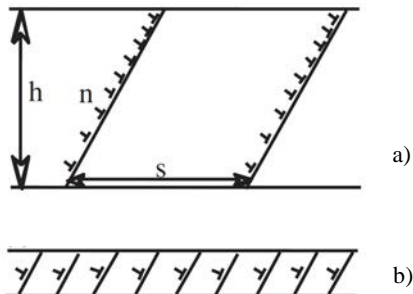


Figure I-36. a) micron-scale, dislocation pile-up; b) nano-scale dislocation distribution [4]

As result of this trapping effect in the nanostructured materials is the increment of lifetime of the component.

Figure I-37 are reported the results of fatigue testing on sample with different surface treatments. The sample coated with nanoscale multilayer present damage at higher number of cycles [5] respect standard coated sample.

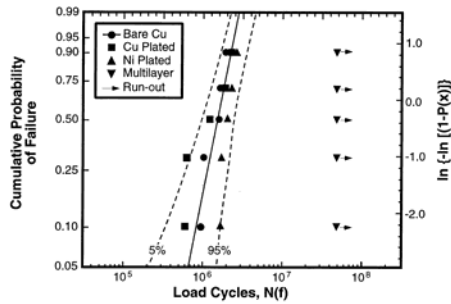


Figure I-37. probability of failure in different samples [5]

Chapter II

PVD Magnetron Sputtering

2.1 PVD Magnetron sputtering technique

Magnetron sputtering is nowadays one of the most important physical vapor deposition (PVD) technique.

Sputtering is a vacuum process, where a process gas (Ar, Kr, ...) is inject in the chamber to maintain the 10^{-2} - 10^{-4} mbar operative range pressure.

The emission of material from the target is an effect of ion bombardment, this is transferred to the substrate surface (the object to be coated) and condense on it Figure II-1.

Nowadays it is used in industrial process and it allows deposition of several materials (metals or compound) with specific mechanical, optical and electrical properties.

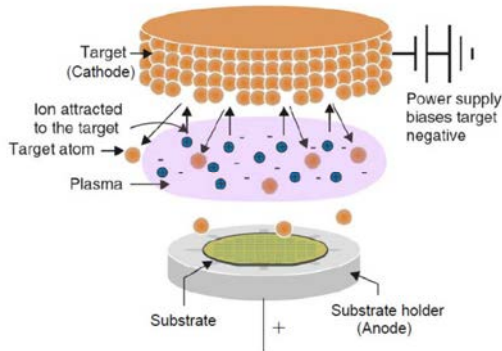


Figure II-1. Schematic representation of sputtering process [71]

The discovery of sputtering process is attributed to William Grove (middle of 19th) [72], he was the first to report the formation of deposit during his experiments on electrical properties of gases at low pressure.

For approximately a century, sputtering technique has been studied and improved in different form and approach, like hollow cathode, magnetic mirrors and finally Penning trap (electric and magnetic fields combined).

The application of Penning trap model in sputtering process was the breakthrough for industrial applications, and the beginning of PVD magnetron sputtering technique.

In a magnetron sputtering source the magnetic field enhances the glow discharge by closed drift of electrons. The trajectory of electrons in non-homogeneous electric and magnetic field is complex to calculate, but using as example only the magnetic field, the electron gyrate with the cyclotron frequency:

$$\omega_e = \frac{eB}{m_e} \quad \text{II-1}$$

Where B is the magnetic inductance, e is the electron charge and m_e is the mass of electron. The gyration radius of an electron with velocity component $u_{e\perp}$ perpendicular to B vector is:

$$r_{g,e} = \frac{u_{e\perp}}{\omega_e} = \frac{m_e u_{e\perp}}{eB} \quad \text{II-2}$$

Typically an electron will gyrate many times around the magnetic line before to collide with another particles.

Adding the electric field the electron path is perpendicular to B and E vectors.

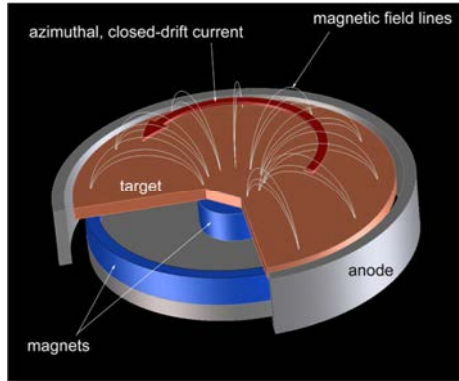


Figure II-2. Circular magnetron sputtering source layout and relative electron race-track [73]

When the plasma discharge is established, most of voltage drop (hundreds volts) in space-charge layer (sheath), that separate the surface and the plasma glow. Only few percent of voltage drop outside the sheath and the value depends from the intensity of magnetic field and discharge condition. The presence of the sheath induces an energy gain of electrons when they across the sheath. The plasma electrons are bounced and return to the plasma because they have typically few eV of energy, not enough high to cross the sheath.

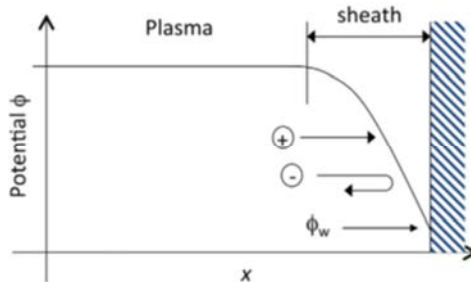


Figure II-3. Potential of plasma

The ions due to their high gyration radius are not affected by magnetic trap. The positive ions are accelerated by electric field and impact on the target surface, whereas the negative ions are repulse in opposite toward. When an energetic ion impact onto the surface, different phenomena may occur Figure II-4:Figure II-4:

- Ion may be reflected and neutralized in the process
- Ion may cause ejection of electron (secondary electron)
- Ion may become buried in the target (implantation)
- Ion impact may cause a series of collisions between atoms of the target, and promote the ejection of target atoms.

The material is ejected from the target in form of atoms, because the process involve a kinetic energy cascade transmission. In fact the emission of clusters or droplet is a typical characteristic of other PVD technique like arc discharge deposition. Moreover the most of emitted atoms are neutrals and only few percent are ions [74].

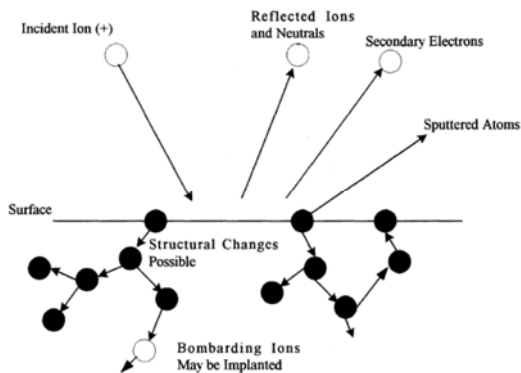


Figure II-4. Ion impact effect [75]

Finally the ejected atoms cross to the plasma and finally condense on the sample substrate and form the coating.

It is possible obtain different coating microstructures in function of experimental parameter and process [76][77].

In a simple sputtering system (without assisted ions bombardment growth), microstructure of coating is depends mainly from process pressure and temperature of the substrate.

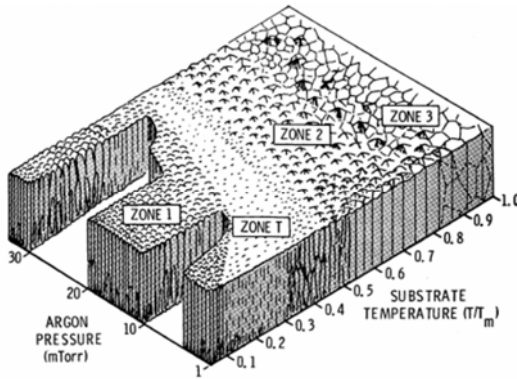


Figure II-5. Thornton's structure zone diagram for sputtering [78]

The Thornton structure zone diagram (SZD) is divided in 4 zone:

- Zone 1: the low adatom mobility lead a continuous nucleation, the result is a very fine-grin texture growth in deposition flux direction, with high ratio of pores and defects.
- Zone T (transition zone): structure is non homogeneous along the film thickness. The surface diffusion is notable but grain boundary diffusion is strongly limited leading to competitive grain growth, the result is a V-shaped grains.
- Zone 2: the higher energy of adatom permits the movement on surface, the result is a columnar crystal structure with lower rate of defect than zone 1 and near perpendicular grain boundaries direction
- Zone 3: bulk diffusion and recrystallization leads to dense films with large equiaxed grains.

The two parameters in Thornton's diagram, pressure and substrate temperature are an indication of the energy of sputtered atoms on the surface. Indeed if the atom that arrives on the surface (adatom) has enough

residual energy to move on the surface the final coating results composed by big crystals.

Increasing the process gas pressure, the thermalization of sputtered materials is increased too, that means the atoms lose part of their kinetic energy in collision with gas before to arrive on the surface, the result is a proneness to nucleate a new crystal.

Instead in an hot substrate the energy is supplied by thermal energy to adatom, in this way the adatom has enough energy to move on the surface and find a lower energetic point to condense, generally at boundary in already existent grain. The variation of this two parameters permits to promote different kind of crystal structure.

2.2 HiPIMS technique

High power impulse magnetron sputtering (HiPIMS) or high power pulse magnetron sputtering (HPPMS) is the last improvement in sputtering deposition technique.

HiPIMS was developed to respond to the increasing request of functional coatings in the microelectronic field, where the standard sputtering coating technique is not suitable due to the complex geometry of electronic device [79].

HiPIMS is the alternative to the other sputtering technology studied in 1990s, ion PVD deposition (IPVD) techniques, that uses a standard sputtering process (dc-MS, rf-MS) coupled with a secondary ionization source (RF-coil or ECR) [80] that improves the metal ions formation.

Instead in HiPIMS the ionization of sputtered metals, generated by high density plasma, happens directly close to the target. In this way the sputtering system became very easier than IPVD, moreover the fraction of metal ions in HiPIMS is higher (in some case double) compared to IPVD process.

HiPIMS is an high power pulsed technology, that means the discharge happen in short pulse at imposed frequency, with one order, or more, higher power density (kW/cm^2) and the plasma is consequentially more dense too [81][82][83].

Using a pulsed technology involve another advantage; one of main problem in glow discharge and in particular in magnetron discharge is the propensity to “arcing”. The arc is anomalous discharge with high current and low voltage concentrated in small surface’s cathode spot, that induces the emission of unwanted droplet, that prejudice the coating quality.

To reduce the arc phenomenon is necessary decrease the local accumulation charge on target surface. The first technology developed was RF-MS, but has a strong limitation about deposition rate. In alternative of RF-MS in the 1990s the pulsed technology was developed [84][85], that permits to obtain also dielectric coating and decrease drastically the arc probability.

The HiPIMS discharge is more sensitive to the arc phenomenon due to the high density current and high voltage. Modern HiPIMS power supply are equipped with arc detection and arc suppression device, that detect the drop of voltage or the jump in current and it interrupts the pulse.

However, between the arc formation and arc suppression the energy released may damage the target surface.

The reduction of arc odds is the best way to avoid the coating defects and target damages, and that depends of experimental parameters setup, like: pulse length, pulse frequency, amount of contaminations, pressure, pulse voltage and current, magnetic and electric filed non-homogeneity, target material, etc.

As mentioned before, in HiPIMS discharge strong fraction of sputtered material is ionized.

The ion bombardment is commonly used in coating technology to improve the quality and density of films, because the adatom has enough energy to travel on surface and find the lower level energy position.

As consequence of this new amount of energy the Thornton’s diagram has to be redefined adding the energy of incident particle as parameters.

The third additional parameter (E^*) is inserted instead to the gas pressure and it describes the displacement and heating effects caused by the kinetic energy of bombarding particles.

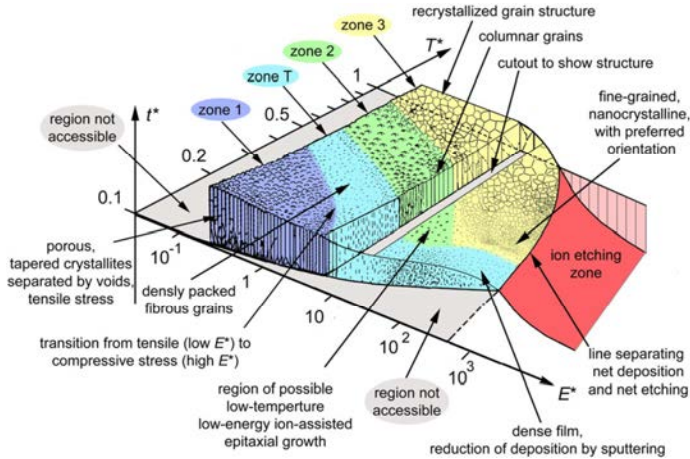


Figure II-6. Structure zone diagram applicable to energetic deposition [86]

As shown in Figure II-6 the main difference with classical SDZ is the reduction of deposition rate in function of energy bombardment.

This effect is accentuated in the ion etching zone (red zone) where the particles induce a re-sputtering effect. It is used to pretreat the surface before the deposition in some applications [87].

HiPIMS is an intrinsic ion-assisted deposition technology without a secondary device, like an ion gun.

Moreover, the energy transfer efficiency is higher than the traditional process, because the main part of the deposition energy on the substrate is made directly by the sputtered material and not by the transfer between process gas-coating.

2.2.1 HiPIMS power supply

The HiPIMS power supply is essentially one or more LC circuits and a pulsing timer (thyristor switch).

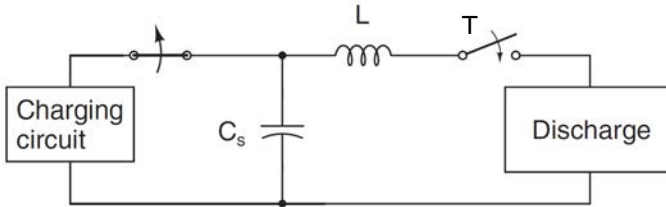


Figure II-7. HiPIMS power supply scheme [88][89]

The charging circuit is basically a DC power supply, that charge the capacitor (C_s), when the switching component (T) close the circuit the capacitor releases the charge on the magnetron and glow discharge starts.

The inductance coil (L) is connected in series with the magnetron and it has the purpose the limitation of rate current rise, to avoid the formation of arc discharge and to protect the electrical components.

The pulse shape is not only determined by the power supply, but it depends also by the operative conditions like chamber, magnetron configuration, target material, gas pressure, type of gas, magnetic field structure and time lapse between the pulses.

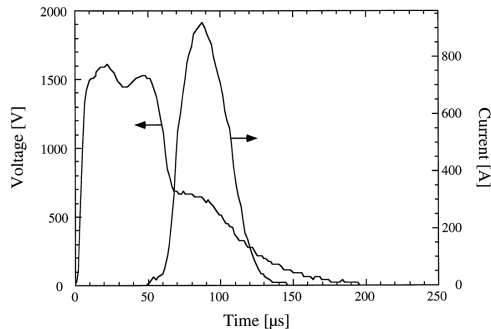


Figure II-8. Example of HiPIMS discharge [79] (Chemfilt R&D AB Sweden)

The Figure II-8 shows a typical voltage and current curves of first HiPIMS generation power supply based on scheme in Figure II-7.

In the last decade, several research groups and companies have developed different HiPIMS arrangements (Figure II-9) for laboratorial and industrial applications and they are developed to increase the rate deposition and for specific process, like reactive sputtering.

These devices are similar in their basic structure which is schematically showed in Figure II-7.

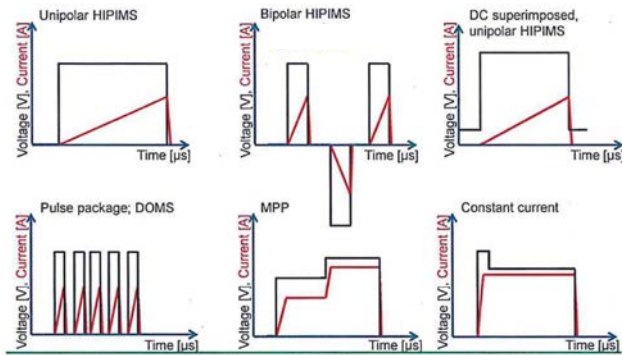


Figure II-9. Different HiPIMS operation modes

2.2.2 HiPIMS discharge

HiPIMS discharge are more complex than standard DC pulsed discharge, due to the fast phenomena evolution in each pulse.

As mentioned before HiPIMS means high power impulse magnetron sputtering, but there are two different interpretations. The first is more technological and it is referred about the higher power or current density compared with a DC discharge (Figure II-11), the second one is referred to the high fraction of metal ions produced in the discharge (Figure II-10).

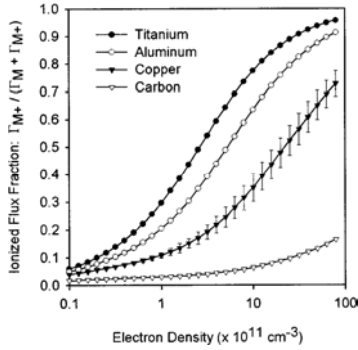


Figure II-10. Fraction of metals ion [90]

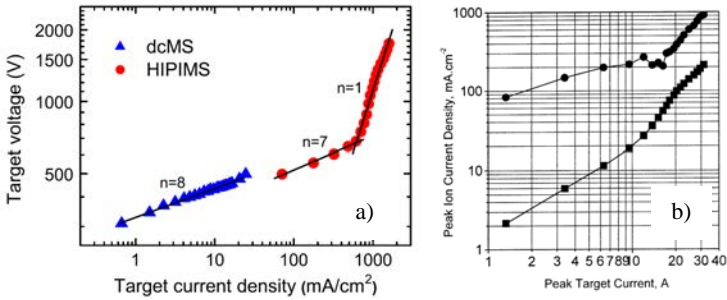


Figure II-11. a) Target voltage vs target peak current density in DC and HiPIMS and b) Ion saturation current vs peak target current [83]

As shown in Figure II-11 the voltage and current peak density increment in the discharge follows a power law [80]:

$$I_d = k_d * V_d^n \quad \text{II-3)}$$

Where:

- V_d is the voltage discharge
- I_d is peak current density

- K_d is a constant of target material, gas type and pressure and geometry of the discharge

High value of coefficient n indicate that the discharge may arrange a significant amount of current with a small increment of the target voltage. This is possible because the plasma is relatively weakly ionized and more charge can be generated as needed.

The current consumption in the discharge (HiPIMS, DC, RF) is caused by ion charge neutralization (I_i) and emission of secondary electrons (I_e).

$$I_d = I_e + I_i = I_i(1 + \gamma_{SE}) \quad \text{II-4}$$

Where γ_{SE} is secondary electron emission coefficient (0.05-0.2 for most metals), that means the most part of discharge current is caused by ion current. Due to the low efficiency of secondary electron emission, each SE produces more than one electron-ion pair.

$$N \approx \frac{V_d}{\varepsilon_c} \quad \text{II-5}$$

Where ε_c is the energy loss to create an electron-ion pair.

In HiPIMS discharge the coefficient n has two different operation mode. At low discharge density current indicates a classical discharge operation and at high density current the exponent (n) strongly decreases close to 1.

The reason of this drop is explicable with the reduction of secondary electron trapping in HiPIMS and the formation of non-homogeneous turbulent plasma fluxes on magnetron surface [80][91][92].

As shown in Figure II-8, the current curve is shifted in time than voltage curve.

This delay time is characteristic in HiPIMS discharge, when the pulses are independent of each other, that means the pulses are enough distant, without external pre-pulse or low DC discharge. This delay time (t_d) is composed by two factor:

- t_s is the statistical time lag for the initial electron formation, this is strongly affected by external causes, like previous pulse residual, cosmic rays, prepulse...
- t_f is the formative time lag, it corresponds to the necessary time for discharge development from initial electrons

$$t_d = t_s + t_f = t_s + (t_i + t_e) \quad \text{II-6}$$

t_f is also composed of two components, t_i is the necessary time for an ion to reach the target surface and t_e is the time that secondary electrons need to induce the ionization of the gas.

$$t_i = \sqrt{\frac{2sm_i}{Eq_i}} \quad \text{II-7}$$

$$t_e \approx \left(\frac{m_e}{2E_e}\right)^{1/2} \left(\frac{kT_a}{\sigma_{ea}(E_e)p}\right) \quad \text{II-8}$$

Where:

- s is the typical distance between target surface and local ionization
- E is electric field
- m_i is the mass of gas atom
- q_i is electric charge of ion
- m_e is the mass of electron
- E_e is the characteristic energy gain of electron from electric field
- k is Boltzmann constant
- T_a gas temperature (300 K)
- $\sigma_{ea}(E_e)$ is the ionization cross section as ionization probability
- p is the pressure

the t_f is drastically reduced when several initial electrons are present and a significant plasma density is applied before the HiPIMS pulse, this is

realized using low power DC, pre-pulse phase, arc plasma, cathodic arc plasma, high frequency [93][94].

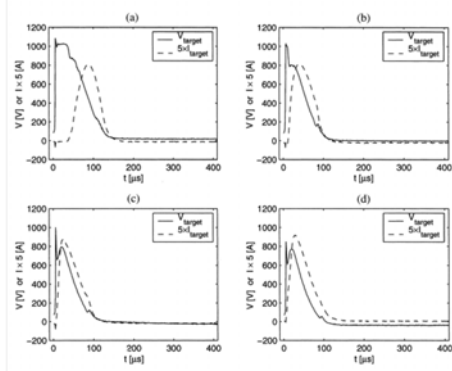


Figure II-12. Voltage and current vs. time from initiation of the pulse using different argon gas pressure (a) 0.5, (b) 2, (c) 10 and (d) 20 mtorr [95]

The dynamic of HiPIMS discharge is more complex than DC discharge, because we have to consider, in addition of standard plasma species (gas ions, neutral gas and neutral sputtered material), the metals ions too.

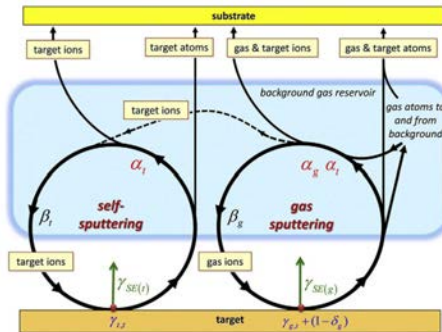


Figure II-13. Schematic representation of HiPIMS discharge. α is the probability of ionisation, β is the probability of return to the target, γ is the secondary electron emission probability. The t and g subscript mean “target” and “gas” [91]

In Figure II-13 the loop on the right is referred to gas process (see cap. 2.1), instead on the left is referred to metal. The contribution of two sputtering loops depends by pulse parameter (power, length and frequency) and discharge parameters (pressure, magnet configuration).

The formation of sputtered metal ions in HiPIMS discharge is due to two main reasons. The first is the lower ionization energy of the metals compared to noble gas ionization energy Table II-1, the second is rarefaction of gas close to the magnetron and the self-sputtering runaway.

	ϕ (eV)	E_{0-1} (eV)	E_{1-2} (eV)
Ar	-	15.76	27.63
Cu	4.9	7.73	20.29
Ti	4.1-4.3	6.82	13.58
Nb	3.96	6.88	14.32
C	4.53	11.26	24.38
W	4.55	7.98	17.62
Al	4.08-4.28	5.99	18.83
Cr	4.5	6.77	16.50

Table II-1. work function, first and second ionization energy of some metals and Argon [96]

The term rarefaction indicates the local gas density reductions and that is equivalent to reducing the original gas pressure.

Rarefaction effect has been studied for DC discharge by Rossnagel [97] and the same phenomenon will expected in HiPIMS discharge Figure II-14.

Using an extrapolation of Rossnagel data at HiPIMS general power density, the density of gas in front of target became very small [73][98].

In rarefaction, the particle flux (neutral and ion) from the target has an effect on the gas in front of the target, because through collision the gas is heated and displaced. The consequence is a decrease of gas density. This effect is well known from several years (Steenbeck 1920s) and it is called also “sputtering wind”[99].

The reduction of gas density induces a loss of ion current on target, consequently the sputtering wind is reduced too. That induces a refill of the gas in the low-density zone and the process restart with another increment of current. Due to these periodical parameters variation the discharge current

shows slow and large oscillation (wave) during the pulse, these are associated to a modulation of gas pressure and sputtering wind [95][100].

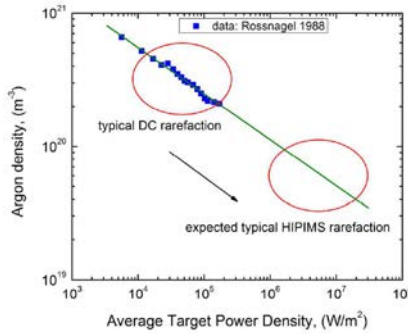


Figure II-14. Extrapolation of expected rarefaction in HiPIMS discharge [73]

In HiPIMS discharge, part of ionized sputtered material returns to the target, like gas ions, and induce sputtering too. This process is called self-sputtering (Figure II-13).

In particular conditions the self-sputtering can operate in a self-sustained mode, that means the discharge is sustained (during the pulse) by only metal ions created in the early stage of discharge. In this mode, it is possible to have sputtering process without process gas [101][102].

The self-sputtering mode is allowed in few material, like copper, chromium, titanium, with high sputtering yield and characteristic condition of gas rarefaction [96].

The scheme of HiPIMS discharge (Figure II-13) in self-sustained mode has to be modify excluding the loop referred to the gas sputtering loop (Figure II-15).

The necessary condition to have sustained self-sputtering is:

$$\Pi = \alpha\beta\gamma = 1 \quad \text{II-9}$$

Where:

- $\alpha < 1$ is the ionization probability of sputtered atom
- $\beta < 1$ is the probability of ion return to target
- $\gamma > 1$ is the sputtering yield (in the case metal-metal)

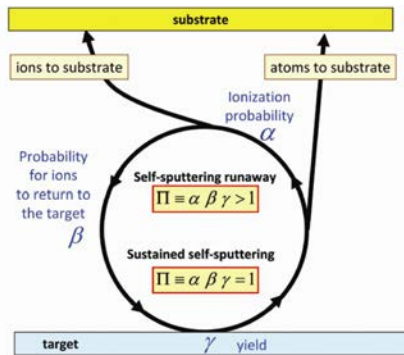


Figure II-15. Representation of self-sustained HiPIMS discharge [73]

The self-sputtering runaway is a particular case, where the parameter Π is greater than 1. The current discharge continues to increase until the power is supplied. The discharge is allowed to rapidly develop into a high current steady state where the ionization and loss processes are balanced. Generally the runaway is stopped (before the end of pulse) by the arc suppression device or power limitation in power supply, otherwise by the melting of target.

2.2.3 HiPIMS deposition rate

As mentioned in previous paragraphs HiPIMS was developed as simplified improvement of I-PVD focused on industrial application.

Increase the deposition rate in industrial field is one of most important goal, because that means less working time and then less cost.

Due to the different physical evolution, it has been reported in several works, in HiPIMS the deposition rate depending by target material, pulse

configuration and the deposition is different in non-reactive or a reactive mode.

The rates range change from 15% to 120% compared to DCMS deposition rate using the same average power [80][103][104][105][106][107].

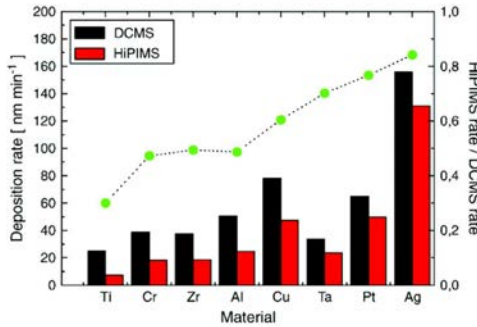


Figure II-16. comparison between DC and HiPIMS deposition rate in some metal target, using same power average. The green dots are referred to HiPIMS/DCMS ratio [107]

About metal deposition (Figure II-16), applying the same average power, the deposition rate of metal target using HiPIMS technique, is generally lower than DCMS.

There are two main reasons to explain the deposition rate loss. The first is referred to the sputtering yield, the second is a consequence of different plasma composition in HiPIMS.

The increment of voltage induce an increment of sputtering yield (Y) and is proportional to the impact particle energy:

$$E = q \cdot eV_t \tag{II-10}$$

$$Y \propto E^m = (q \cdot eV_t)^m \tag{II-11}$$

Where:

- E is ion energy
- q is charge state of ion
- e is elementary charge
- V_t is target potential
- m is a constant (<1) and that depends by mass of particle, mass of target, incident angle

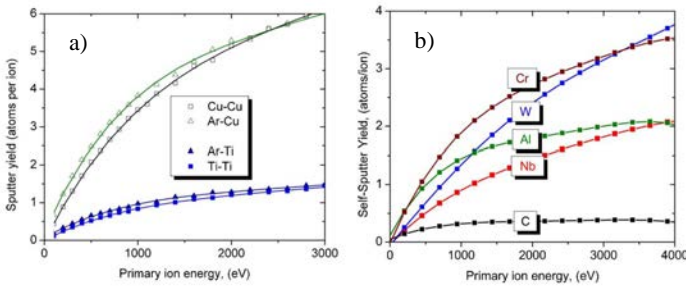


Figure II-17. a) Sputtering Yield function of ion energy. example of Ar and self-sputtering of Cu and Ti; b) self-sputter yield of some target materials [96]

In first approximation the deposition rate is proportional to the target erosion rate (Φ):

$$\Phi = j_i \cdot Y \quad \text{II-12)}$$

Where j_i is ion current on target and Y is sputtering yield.

In DCMS j_i is essentially composed by argon ion (gas ion) and the fraction of metal ion current is negligible. In HiPIMS we have to consider both ions contribution:

$$\Phi^{HiPIMS} = j_i^{Ar+} \cdot Y^{Ar+} + j_i^{M+} \cdot Y^{M+} \quad \text{II-13)}$$

Assuming a same average power applied to the target in DCMS and HiPIMS discharge. The higher potential applied in the HiPIMS discharge induce a lower ion current on target, moreover the increment of sputtering yield is

nonlinear with increment of voltage (eq. II-11) as result the target erosion rate is lower in HiPIMS then DCMS.

The second reason of deposition rate loss is due to the intrinsic development in ion discharge.

When the zone in front of the target is depleted from the gas (Figure II-15), and the discharge is sustained (fully or partially) by the metal ions. The fraction of metal ion, that returns to the target, determines the lower deposition rate, because only a fraction of sputtered material arrives to the sample. Moreover the loss increase with the pulse length, because the metal ion discharge became more predominant.

Another effect incurs in the deposition loss is the larger azimuthal electron current above the race track. That exerts a tangential outward force on the ions and the material flux, part of the ions moves along off-normal (tangential) respect target normal axis, the result is a decreasing of the net flux of material on substrate placed in front of (parallel) to the target surface [106].

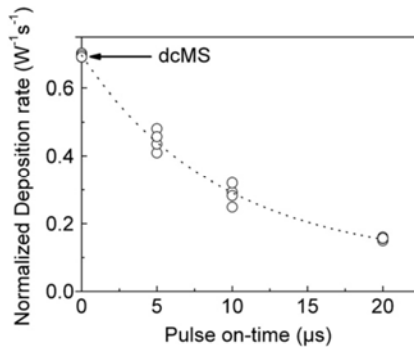


Figure II-18. HiPIMS/DCMS deposition rate vs pulse length [108]

It is possible extend the eq. II-13 with the ion current return (self-sputtering)

$$\Phi^{HiPIMS} = j_i^{Ar+} \cdot Y^{Ar+} + j_i^{M+} \cdot Y^{M+} - j_i^{M+} \quad \text{II-14)}$$

In reactive HiPIMS discharge, the deposition rate is also influenced from reactive gas and in some case the deposition rate may be higher than in DCMS.

To obtain stoichiometry compound film, usually the process run with a surplus reactive gas, in this way all the sputtered metal reacts with the gas and forms the compound, as consequence a poison of target will occur.

The formation of compound on target surface induce usually a reduction of sputtering rate. To reduce the poison effect on the target, generally the gas flow is set close to transition zone, that means in DCMS the target works in an intermediate coverage regime between metallic and compound mode. In DCMS the transition zone is often unstable with hysteresis loop.

The Figure II-19 shows the different trends of deposition rate in DCMS and HiPIMS reactive process. Generally in the reactive HiPIMS discharge the hysteresis loop is smaller or absent at the same DCMS gas flow regime.

The stabilized transition zone is explicable by the competition between the formation and the removal of the compound from target surface.

The reason of more stable transition zone in HiPIMS discharge, is due to the high erosion ratio during the pulse. Indeed at same average power in HiPIMS the current density is very higher than in DCMS, that means the target erosion, compound in this case, is higher too.

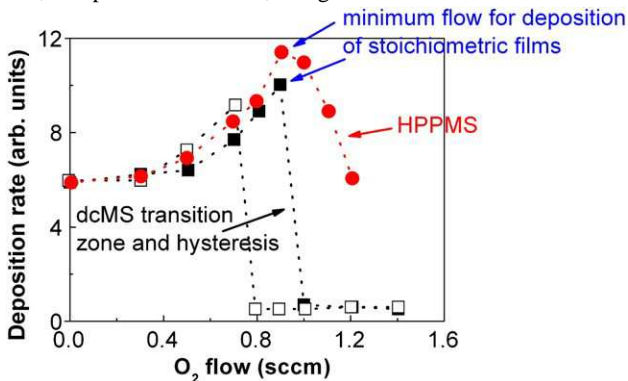


Figure II-19. Comparison of DCMS and HiPIMS deposition rate vs reactive gas flow [109]

2.2.4 HiPIMS coating feature

In coating technology the energy transferred to the film by particles bombardment play an important role on the coating growth.

It is known that the plasma-film interface is affected by the energy, flux, nature and incident angle of bombardment ions. It is possible change the properties of coating (microstructure, optical, mechanical and electrical properties) changing the process parameters as example peak target current, pressure, deposition angle, magnetic field strength, bias, etc. [110] [111].

In this paragraph will be explained the effect of ion bombardment in HiPIMS deposition.

2.2.4.1 Effect on film densification and microstructure

As describe in 2.1 and 2.2 the coating microstructure is strongly influenced by ion flux density and energy, that allows the different film growth (SZD in Figure II-6).

Changing the process parameters such as current peak, and then the ion flux on substrate in HiPIMS discharge, it is possible change the microstructure of the film. As reported in different paper [112][113][114] an high bombardment ion flux allows to obtain fully dense coating, without external sample heating.

An example of film densification as function of ion flux is reported in Figure II-20. The SEM images show how the microstructure change with the increment of ion flux. In DCMS Figure II-20 (on top) the film is columnar, typical of zone 1 and zone T, instead in HiPIMS coating exhibit a dense columnar structure that switch in nanocrystalline type. It is also demonstrated using X-Ray Diffraction (XRD), that shows the reduction of crystal size at high ion flux bombardment.

The fully dense nanocrystalline coating also shows a more smooth surface, because usually, the surface roughness is induced and it is proportional to the crystal size, therefor high adatom mobility promotes the smoothening effect [115][116].

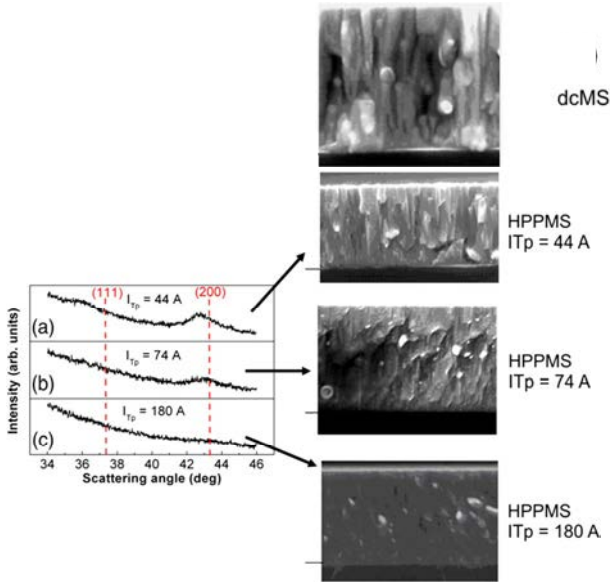


Figure II-20. SEM image of dcMS on top and SEM image with XRD patterns of HiPIMS films grown at different peak target current values [114]

2.2.4.2 HiPIMS coating on complex geometry substrate

In standard sputtering techniques the trajectories of natural particles are defined by ejection distribution from the target and by the thermalization due to scattering with gas. The results is a anisotropic and preferential deposition flux. In non-flat substrate, with presence of grooves or shadowed areas the coating results non homogeneous and porous.

As mentioned the HiPIMS technology was developed for microelectronic device, where the high quality and high homogeneous coating on complex shape substrate is required [79][113][117][118]. In order to simplify and enhance the deposition flux management of already used coating technology (hollow cathode, inductive RF ionization, filtered cathodic arc and so on).

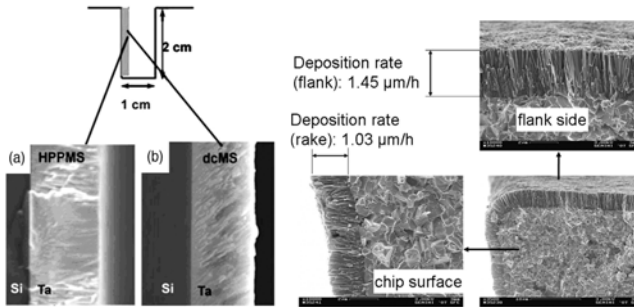


Figure II-21. Examples of coating on complex shape substrate. Deep groove (left) [116] and flank of cutting insert (right) [119]

HiPIMS is an alternative easier technology, that allows to improve coating quality and homogeneity on complex shape substrate.

2.2.4.3 HiPIMS substrate pretreatment

Another important feature of HiPIMS is the possibility to pretreat the substrate using metal ions present in the discharge.

It is established that the adhesion has an important role in functionality and life-time of the coating, because the film-bulk interface is one of most breakable point of coating.

The presence of surface contaminant, like oxide and organic layer, may prevent the direct contact and bonding between coating and substrate, as result the coating is weakly joined with Van-der-Waals forces. Moreover local contaminated areas may cause shadowing and large-scale defects growth.

Often in industrial field, in order to remove the surface contamination, a surface pretreatment is applied to substrate, using argon ion as ion etching and reactive ion etching (RIE) using oxygen. This method is like sputtering process and it has an easy implementation, chiefly when the gas is already part of the coating process.

There are some problems about this procedure, using only argon ion the removal of carbon is very slowly due to low sputtering yield.

Using RIE technology with oxygen, the surface carbon contaminations are removed quickly, with formation of volatile species (CO and CO₂) but sputtering yield of the metal generally is higher than carbon. A local roughness appear due to the differential erosion rate, moreover reactive gas may cause an oxidation of the surface.

Another problem induced by the energetic non-metallic ion bombardment is the incorporation of inert gas, that remain inside of substrate at interstitial site of lattice, causing stress.

The use of high energy metal ions, as pretreatment, it is a valid option to reactive ions, because it avoid the problem of oxidation. The pretreatment is made applying a negative bias to the substrate (several hundred volt), in this way the ions produced in the discharge are attracted and cause the cleaning of surface.

Furthermore it is demonstrate, that the implantation of coating metal in the substrate promote a large-scale epitaxial crystal growth, that enhance the adhesion [87][120].

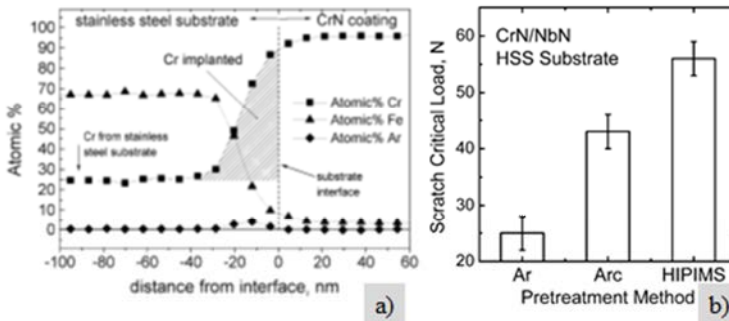


Figure II-22. a) Metal implantation profile [120]; b) adhesion comparison [87]

HiPIMS ion etching promotes the adhesion better than arc discharge, moreover the arc technique needs a macro particle filter to avoid the deposition of droplet on substrate. The nature of HiPIMS discharge doesn't need filter device, that means easier compact and cheaper deposition system.

Chapter III

Cavity iris inspection

3.1 Overview

Courteously Valery Dolgashev provides an X-band cavity iris (Figure III-1) tested at SLAC. The iris has been examined in two different run. The first at INRIM institute in Turin using a FEI Quanta 3D FEG Dual-Beam model and the second run at INFN-LNL (Legnaro, Padua) using a Tescan Vega3 model.

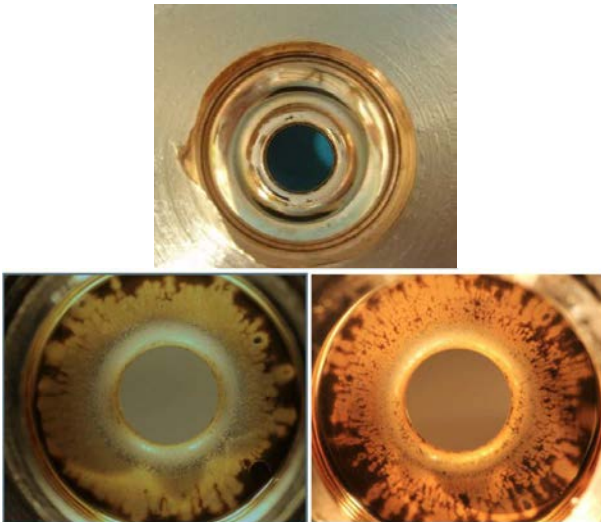


Figure III-1. Pictures of analyzed X-band cavity iris [32]

The goal of this study is understand the kind of surface damages are induced by pulsing RF load.

3.2 Results

The tested iris shows two different surface damages, the first type is induced by thermal fatigue (PSB, grain boundaries damage..). The second is caused by the breakdown electrical discharge (1.3).

3.2.1 Iris thermal fatigue damage

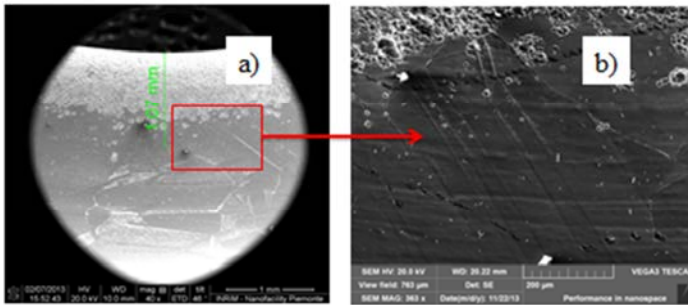


Figure III-2. Surface damage grain boundaries exposure (INFN-LNL)

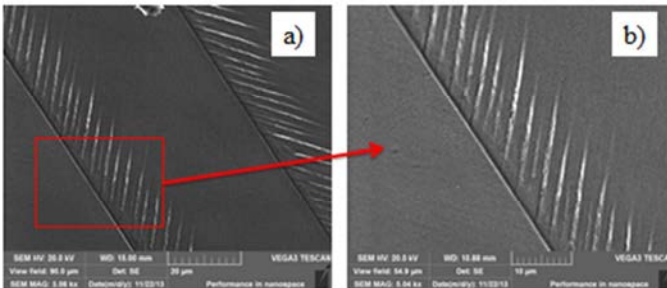


Figure III-3. Grain boundaries exposure (INFN-LNL) referred to Figure III-2

In the previous figures are reported the large damages of iris, due to thermal expansion and contraction of the material, that induce thermal fatigue, as describe in literature [28] [44] [54]. Furthermore the grain boundaries are a preferential point for the ignition of first type of PSB, due to higher localized stress in according with fatigue theory[33].

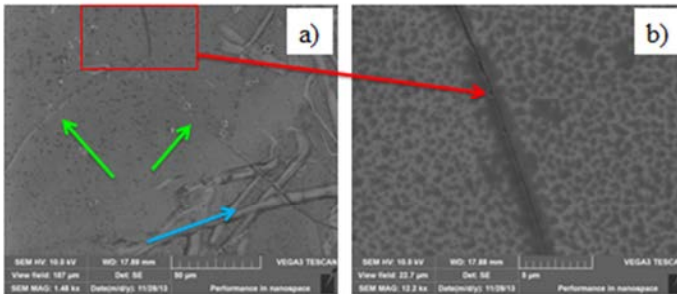


Figure III-4. Different surface damage (INFN-LNL), various defects a); crack b)

The Figure III-4 shows different surface damages, the red line indicate a crack located at grain boundary, the green lines indicate the grain boundaries exposure and finally the blue line indicate roughness due to manufacturing process or a post manipulation of iris.

In Figure III-5 and Figure III-6 is shown another typical large area surface damage. The surface melting or pre-melting phase reported in the pictures are in according with the electromigration scenario [59].

Finally Figure III-7 and Figure III-8 show the roughness increase caused by the PSB formation and growth.

The relevance of the study of surface damage, it is due to the fact that these sites are thought to be the ignition site of breakdown phenomenon.

Understand, where and which kind, of damage growth on surface is a fundamental step for develop the surface engineering improvement.

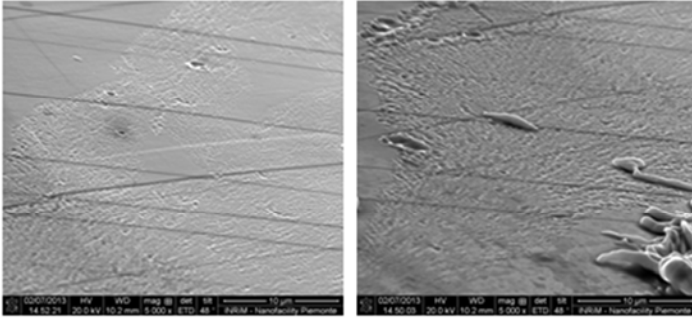


Figure III-5. Large melted area (INRIM)

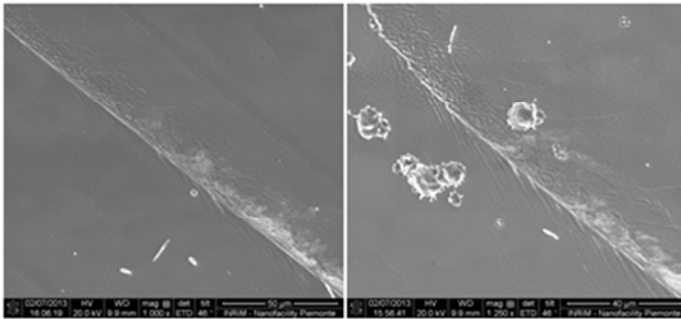


Figure III-6. Large melted area close to grain boundary

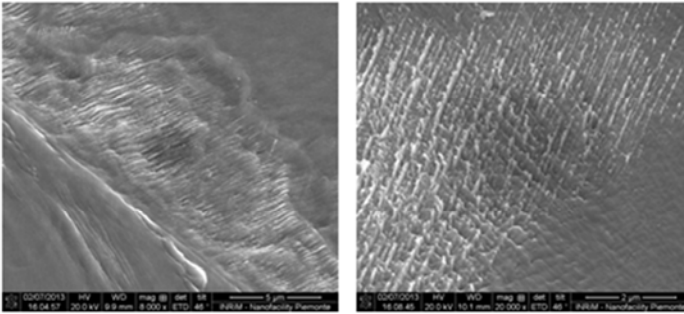


Figure III-7. Roughness induced by PSB growth (INRIM)

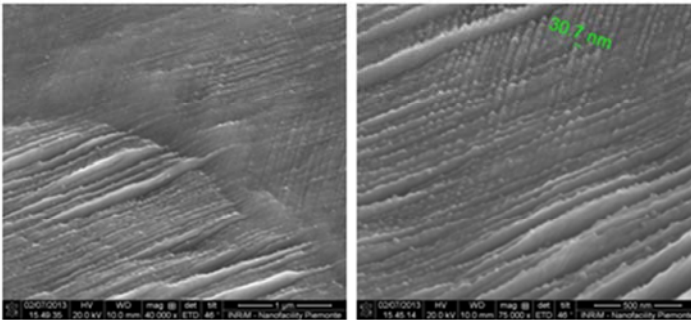


Figure III-8. Roughness induced by PSB growth (INRIM)

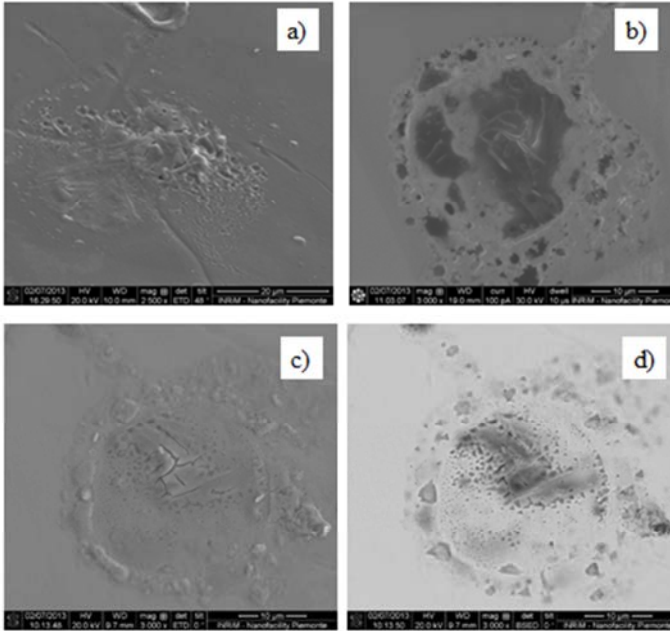


Figure III-9. Bulk material defect, SE image a) and c); ion image b); BSE image d) (INRIM)

The Figure III-9 shows a bulk material defect using different detectors and sources. This kind of defects are ascribed to a manufacturing process of the mandrel and to the electroforming process, that introduces a preferential direction of crystal growth (see 1.2)

A nanostructured multilayer coating decreases strongly the appearance probability of this kind of breakdown ignition site.

3.2.2 Iris breakdown damage

As describe in 1.3.4 the breakdown consist in an electrical discharge that compromises the correct operation of the cavity.

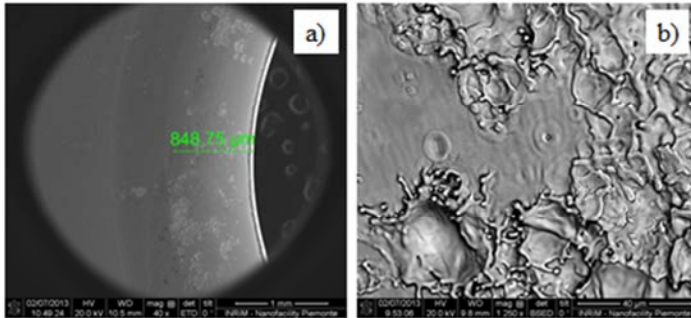


Figure III-10. Wide field a) and melted area b) (INRIM)

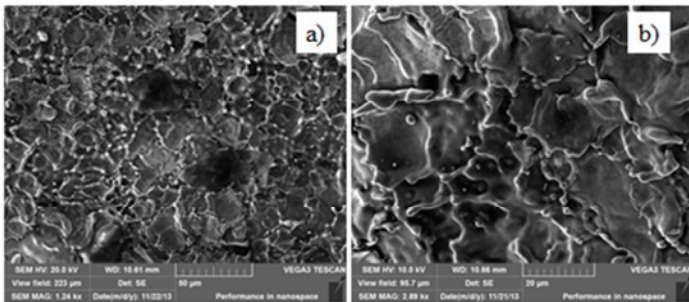


Figure III-11. Melted area by electrical discharge(INFN-LNL)

The damages induced by breakdown are localized close to the iris aperture, where the electric field is higher (see 1.3.4).

The shape and the extension of surface damage is in agreement with the classical breakdown scenario, but it is not possible to exclude that the large damage is due to an avalanche discharge. In this case the crater may be a field emitting sites or, an effect of hot spot induced by the final point of electrical discharge.

To support this assertion, on the iris surface it is possible discern two type of defects. The first is the melted region, more extended, with bobble and craters, the second is distinguish by localized and isolated melted or pre-melted point.

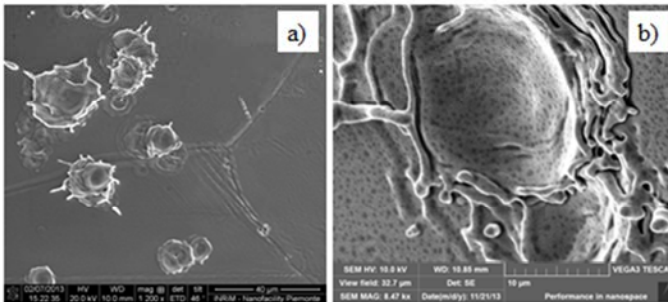


Figure III-12. Exemple of melted spots type 1 INRIM a) INFN-LNL b)

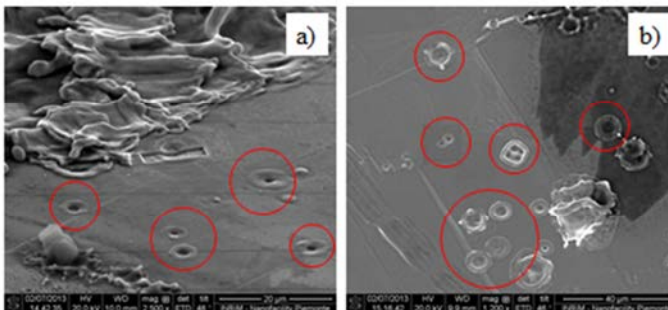


Figure III-13. exemple of localized hot spot type 2 (INRIM)

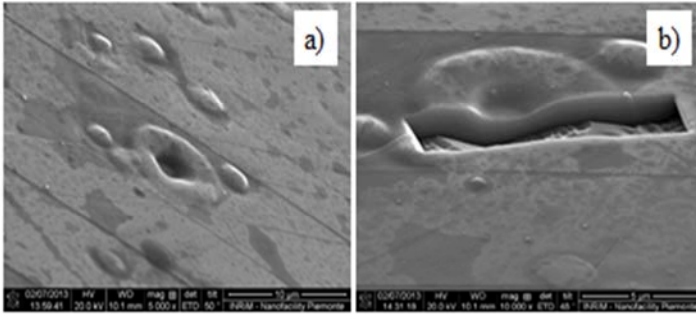


Figure III-14. Type 2 defect inspection before a) and after FIB erosion (INRIM)

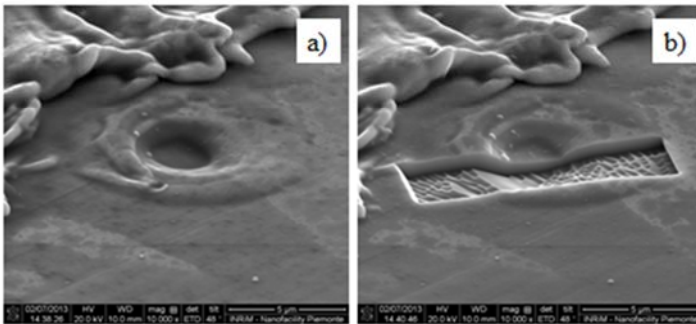


Figure III-15. Type 2 defect inspection before a) and after FIB erosion (INRIM)

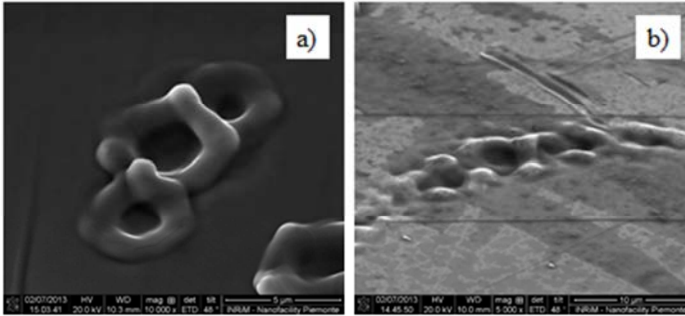


Figure III-16. overlapping of type 2 defects (INRIM)

About the type 1 defects, it is not possible the discrimination between starting or ending point of the discharge, in fact a strong heating in short time, like an electrical discharge, it can produce the melt, the evaporation and the explosion, obtaining damage craters like [121][122].

The spots type 2 may be generated by an external energy source, such as an electrical discharge. In this case the amount of energy it is not high enough to produce the bubbles explosion, but sufficiently high to produce a melted or pre-melted area, quenched in short time, like reported in previous SEM pictures.

Moreover the absence of sub-surficial defects, like holes or inclusions, proved using FIB cross section (Gallium ion beam), shown a contradiction with the classical breakdown scenario and with electromigration breakdown scenario.

Chapter IV

Chamber setup

4.1 PVD Deposition Chamber

The deposition system used in this experimental work is a full steel AISI 304 parallelepiped chamber (720mm,640mm,1090mm) designed and realized at INFN-LNL and already present in physical of materials laboratory.



Figure IV-1. Deposition chamber

The technical characteristics are reported in appendix 9.

The vacuum is provided by:

- One turbo-molecular pump Varian V1200 (1200 l/s 555Hz)
- One dual stage Eduard primary pump (80m³/h).

The pressure is monitored using vacuum meters:

- One Pfeiffer Pirani gauge model: TPR 010
- Two Pfeiffer Penning gauge model: IKR 020
- One Pfeiffer full range gauge model: 251A
- One MKS Capacitance gauge model: Baratron full scale range 0.05 Torr

Magnetron Sputtering source:

- One couple of rectangular Teer Coating (UK) magnetron in close field configuration, directly back cooled, dimension 24.4cm x 13.3cm used for HiPIMS deposition
- One rectangular source AJA international (USA) model ST2056 dimension 2" x 5.63", used for gettingter process.

Power supply:

- Hüttinger 4001, HiPIMS technology (Molybdenum and Copper sputtering)
- Sinex 1.2, HiPIMS technology (Molybdenum sputtering)
- Senvac Maris GS-05, DC (Titanium gettingter)
- ENI RPG-50, DC-pulsed DC (Titanium gettingter and plasma cleaning)
- Kepco BOP100 in series with two Deltaelektronica ES:03-5 (sample holder polarization)

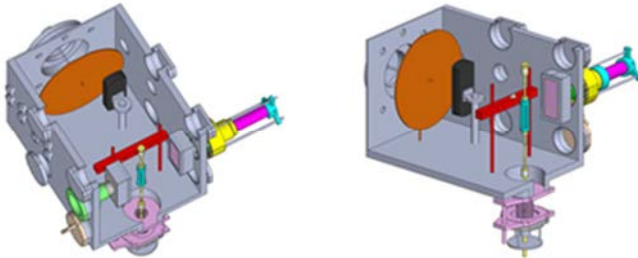


Figure IV-2. Deposition chamber design

The chamber may be divided into two parts, the main HiPIMS deposition subsystem and the titanium gettingter subsystem.

The first part (Figure IV-3) is dedicated for ionized metallic deposition and is composed of:

- Two magnetron sputtering sources
- Rotating, biased, and cooled sample holder shaft

- Sample holder
- Optical fiber holder
- Sample holder shaft alignment system
- Magnetron motion heavy device

About the two magnetron sputtering source, the close field unbalanced configuration allows to have a higher plasma density around the sample holder during the deposition. In this way the biased sample has an high ratio of plasma ions bombardment (see 2.2).

The second subsystem is less complicated, it is composed by a small magnetron sputtering source, equipped with a Titanium target, and a large rotating disc. The role of this sub system is remove all the contaminant present in the chamber, like oxygen and water, during the deposition. The sputtered titanium metal is an active gettering and works as a chemical pump. The rotating disc provides to maintain a new active getter surface on view of sample.

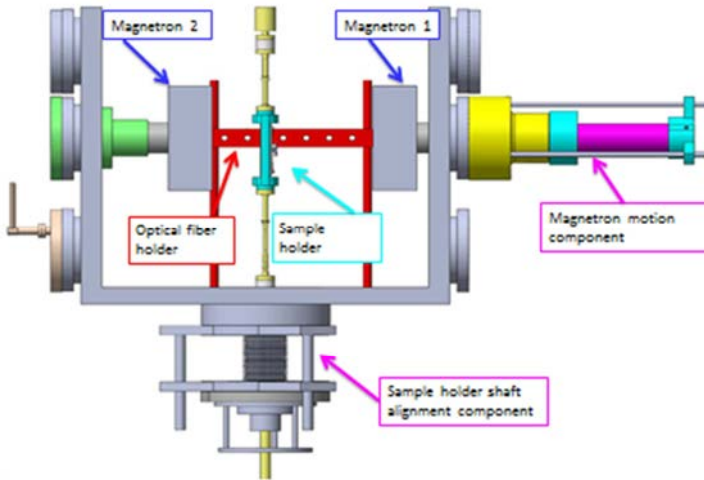


Figure IV-3. Main subsystem design for HiPIMS deposition

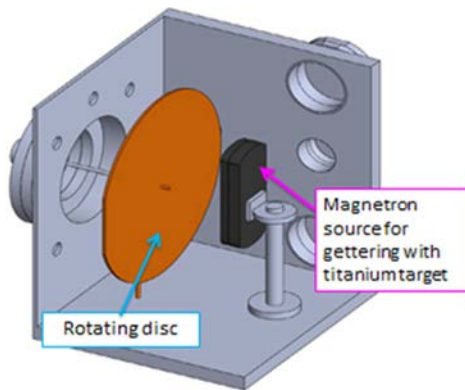


Figure IV-4. gettering subsystem

4.2 Mechanical component design

All the mechanical components used in this experiment (colored component in previous image Figure IV-2: Figure IV-4) have been ad-hoc designed.

All the components have been made at INFN-LNL workshop except the sample holder that was realized by external company.

4.2.1 Sample holder

Since the complex shape of the final sample, the mandrel includes deep grooves with vertical walls and aspect ratios in the range 4÷5. It has been designed a sample holder that mimic the shape of mandrel.

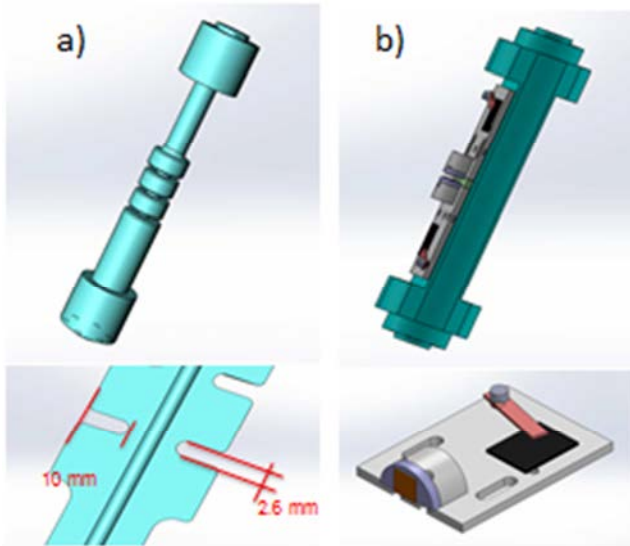


Figure IV-5. final sample a) and sample holder b)

The sample holder realized allows to remove samples from the chamber without dismantle all sample holder from rotating shaft.

The detail in Figure IV-5 b) shows the element that mimics the mandrel grooves curvature. It is possible to remove and replace every single part of sample holder, moreover regulating distant between the two symmetrical elements allows the regulation of the grooves aperture.

4.2.2 Sample holder shaft

The characteristic PVD deposition technique requires the sample cooling, biasing and the constant rotation.

In order to satisfy these features it has been designed a shaft composed by two parts.

The upper half shaft includes the entrance part of water cooling system, bias feedthrough and it provides to hold on and rotate the sample holder.

The lower half shaft basically close the water cooling system and it discards the water in a vessel outside the chamber.

The two half shaft are connected to sample holder in the midway of the chamber between the two magnetron, using Swagelok VCR connectors. Once connected the two half shaft and the sample holder constitute only one stiff component.

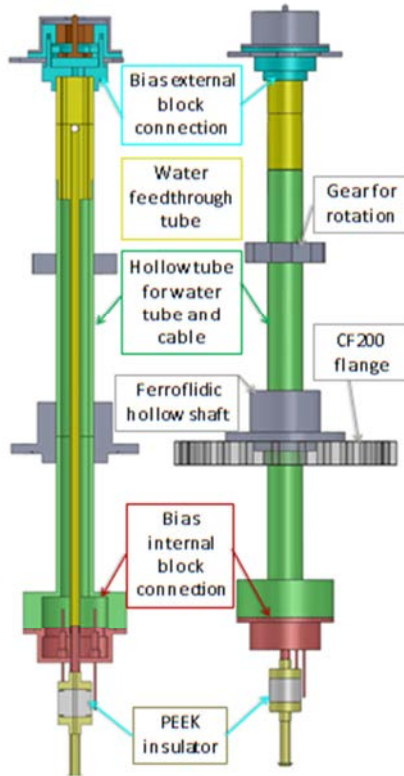


Figure IV-6. Design of upper half shaft

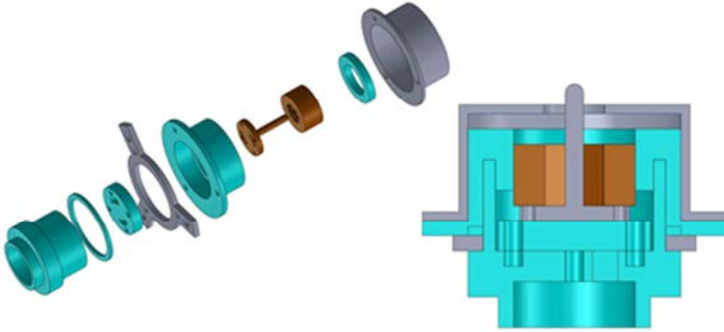


Figure IV-7. Bias external block connection design

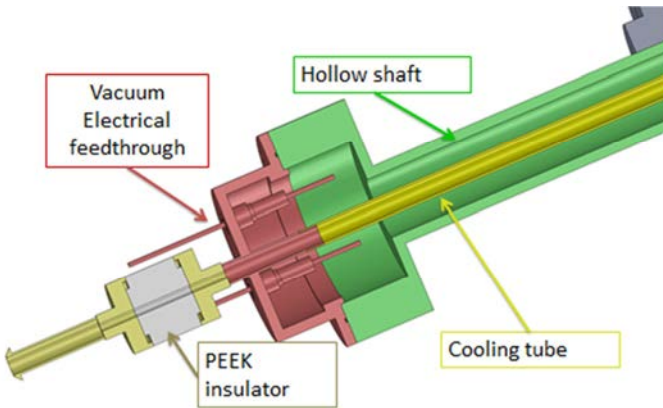


Figure IV-8. Bias internal block connection design

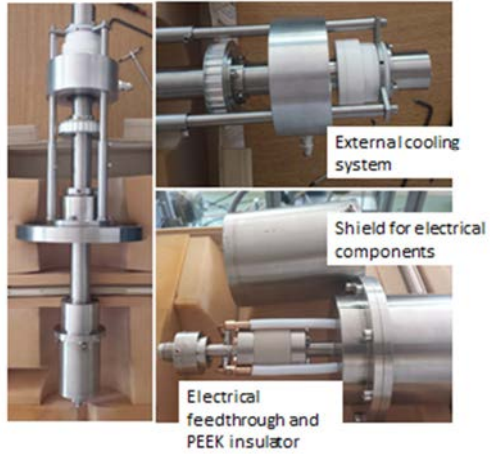


Figure IV-9. Final upper half shaft



Figure IV-10. Final lower half shaft

4.2.3 Shaft alignment component

At the beginning the chamber was designed for another experiment, in that case the easy and fast sample replacement was a trait. For this reason the chamber is equipped of two covers which constitute the top of chamber. The joint of the cover introduce a misalignment among the two flanges, one positioned on the cover and one on the bottom of the chamber. Due to the high rigidity of sample holder shaft an external alignment component is indispensable to compensate the misalignment.

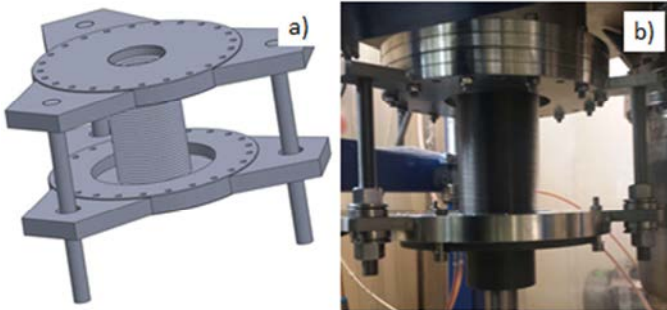


Figure IV-11. Alignment component design a) and relative mechanical component assembled under the chamber b)

This mechanical component consist in two CF200 flanges connected by a welded bellow. The two flanges are bounded with three adjustable independent poles, these parts allow to compensate the misalignments in X,Y,Z direction and in flange plane (four freedom degrees).

4.2.4 Magnetron motion component

In the first configuration the magnetrons was positioned 21cm far from the sample holder, as result a very low deposition rate.

To improve the deposition rate has been designed a custom extended CF150 flange, that allows to reduce the gap between the target and the sample.

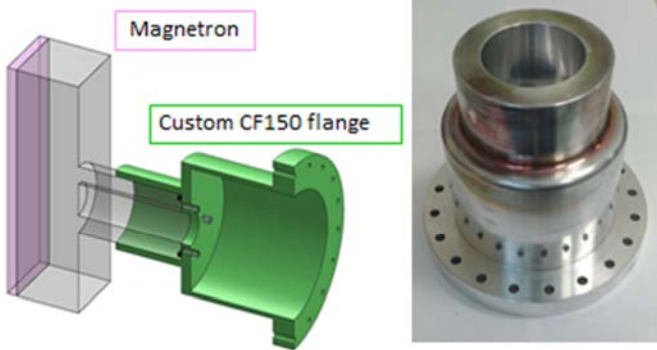


Figure IV-12. Static magnetron holder extended flange

At the later time has been designed a different magnetron holder, that allows the distance regulation between sputtering source and sample holder.

Unlike the commercial solutions that need gears and expensive bellows, this resulted heavy component allows a 15cm magnetron translation using simply a M8 threaded rod, moreover a pneumatic improvement is feasible.

The stiffness is essential due to the cantilevered magnetron and its weight (close to 20kg).

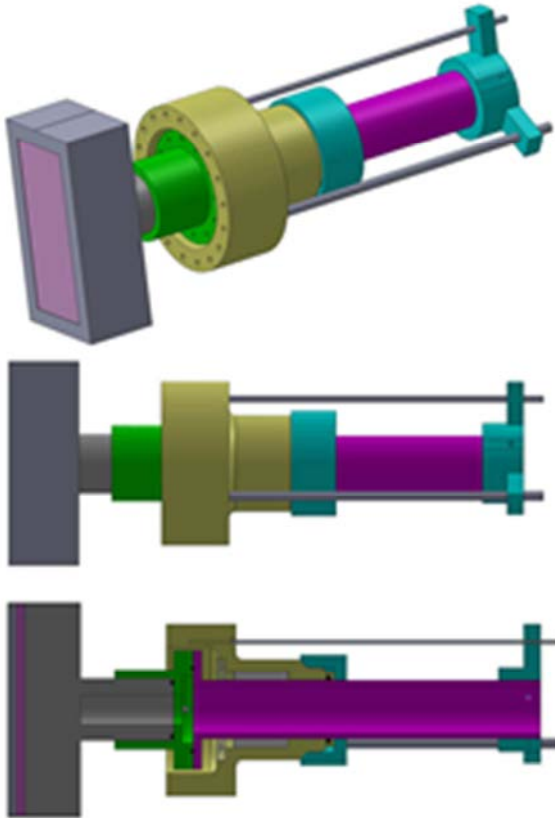


Figure IV-13. magnetron motion component in retracted configuration. Distance magnetron-sample holder 21cm

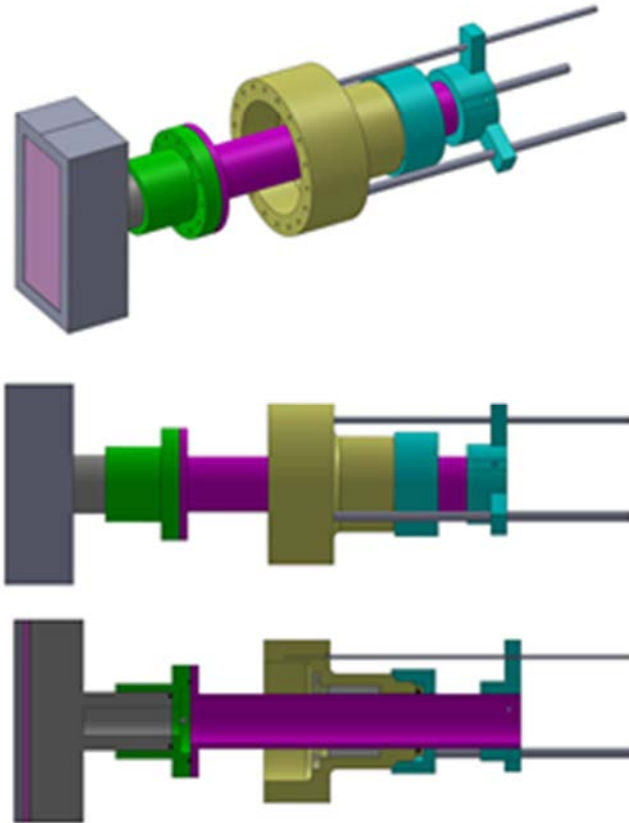


Figure IV-14.magnetron motion component in extracted configuration. Distance magnetron-sample holder 6cm

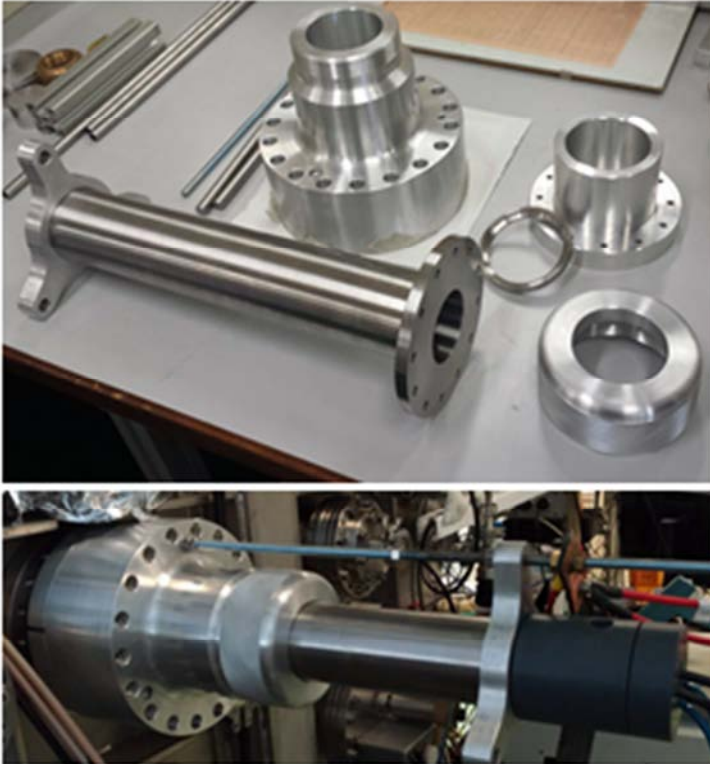


Figure IV-15. Completex magnetron motion component, just finisced and assembled on chamber

4.3 Bias circuit box

HiPIMS technique has an intrinsic incompatibility with the standard bias power supply, due to the high density plasma and then high current pulse.

When the HiPIMS discharge starts, the plasma density close to the target grows rapidly, that induces a dense ion flux toward to sample holder.

Due to the fast increment of current sample holder absorption, the use of standard DC power supply for bias is not possible. The reason is the arc detector, a power supply safety device, that interprets the ion flux like an arc and it intervenes closing the voltage output.

As results the sample ions bombardment is effective only for initial few microseconds of discharge, furthermore the intensive uses of this device may damage the instrumentation.

Usually coupled to HiPIMS power supply, a specific bias power supply is used. That is equipped with a specific heavy arc detector, which does not damage the power supply by the continuous use. When the current rise exceeds the safety threshold, it close the voltage output applied to sample holder. That means, in the initial part of pulse a strong ion bombardment is guaranteed, but it is useless for most part of pulse.

Our goal it is to maintain the bias more constant as possible during all pulse, and then to mantein the ion bombardment effect during all the deposition phase.

To do that a constant negative voltage bias without arc detection it is mandatory. To improve the constant bias a dedicated RC circuit has been designed (Figure IV 16, Figure IV 17).

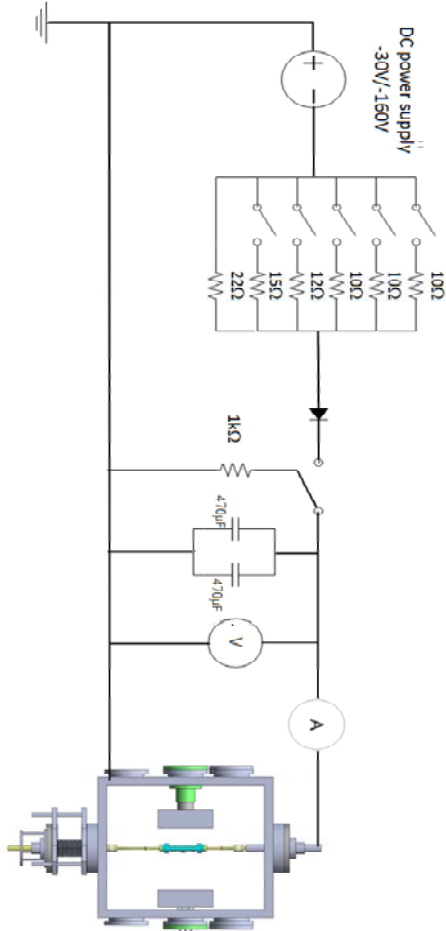


Figure IV-16. Bias circiute scheme

The RC network is composed by a parallel resistance bank and parallel capacitors in series. Changing the resistance bank configuration or adding

capacitors is possible modify the time constant τ of the circuit. A diode protects the power supply from the reversal current. Different configurations have been tested, as result the best one is 2Ω and $940\mu\text{F}$, that provide to a short τ (less than 20ms) and a complete voltage bias recovery.



Figure IV-17. realized bias circuit with DC power supply

The 22W resistor is always connected for safety reasons.

Chapter V

HiPIMS discharge diagnostic

5.1 Instrumentation setup

The study of discharge electrical characteristics is an essential step for understand the physical mechanisms that occur in it. The goal is find the more suitable parameters for the deposition process.

For this reason it has been installed current and voltage probes in order to measure and monitor the electrical time-evolution of discharge.

The monitoring system is composed by:

- Lecroy wave runner 6030 oscilloscope
- Tektronix TCP404XL current probe applied to magnetron
- Tektronix TCPA400 amplifier (coupled to TCP404XL)
- Tektronix TM502A current probe applied to sample holder
- Tektronix A6303 amplifier (coupled to TM502A)
- Tektronix PPE 4kV 100x voltage probe applied to Hüttinger 4001 output
- Tektronix PPE 4kV 100x voltage probe applied to sample holder
- Tektronix P6015 1000x voltage probe applied to Sinex 1.2 output

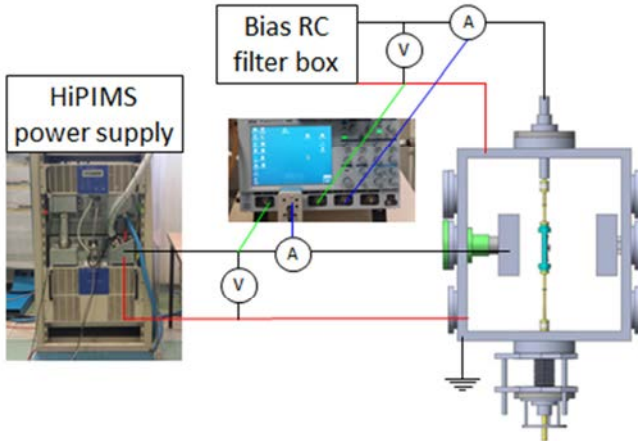


Figure V-1. Electrical Monitoring scheme

5.2 Results

5.2.1 RC bias circuit

The setting of bias box filter has been done by changing the number of resistors and the number of capacitors.

The parallel group of resistors is composed by:

- Three resistors 10Ω
- One resistor 12Ω
- One resistor 15Ω
- One resistor 22Ω

The 22Ω resistor is always connected.

It has been chosen to use at least two capacitors because, using only one capacitor, in the early stage of HiPIMS discharge the current limitation protection of the DC power supply is active.

The HiPIMS discharge parameter used for this testing are:

- Power supply: Hüttinger
- Target Molybdenum
- Voltage: 1000V
- Mean power: 1.5KW
- Pulse width: 75ms
- Distance: 21cm

test	R1 [Ω]	R2 [Ω]	R3 [Ω]	R4 [Ω]	R5 [Ω]	R6 [Ω]	R _{eq} [Ω]	C _{eq} [μ F]	τ [ms]
0	22	15	12	10	10	10	2.02	940	1.90
1	22	open	12	10	10	10	2.33	940	2.19
2	22	open	open	10	10	10	2.89	940	2.72
3	22	open	open	open	10	10	4.07	940	3.83
4	22	open	open	open	open	10	6.88	940	6.46
5	22	open	open	open	open	open	22.00	940	20.68

Table V-1. Resitors configuration with two capacitors

test	R1 [Ω]	R2 [Ω]	R3 [Ω]	R4 [Ω]	R5 [Ω]	R6 [Ω]	R _{eq} [Ω]	C _{eq} [μ F]	τ [ms]
0	22	15	12	10	10	10	2.02	1410	2.85
1	22	open	12	10	10	10	2.33	1410	3.29
2	22	open	open	10	10	10	2.89	1410	4.08
3	22	open	open	open	10	10	4.07	1410	5.74
4	22	open	open	open	open	10	6.88	1410	9.69
5	22	open	open	open	open	open	22.00	1410	31.02

Table V-2. Resitors configuration with three capacitors

Due to the non-ideal nature of the device is not possible calculate the real time constant of circuit using the standard capacitor charge equation:

$$V(t) = V0 * (1 - e^{-\frac{t}{\tau}}) \quad V-I$$

There are two main reasons that may explain this behavior. The first one is the DC power supply that provides power during the capacitor discharging. The second reason is relative to the cables resistivity and inductivity.

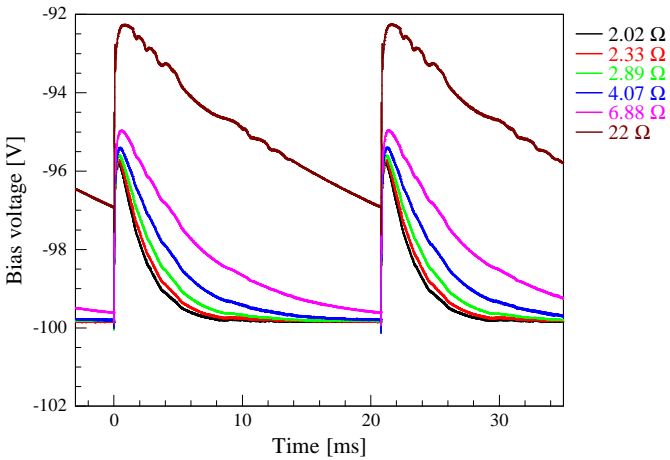


Figure V-2. Bials voltage recovery between two pulses using two capacitors

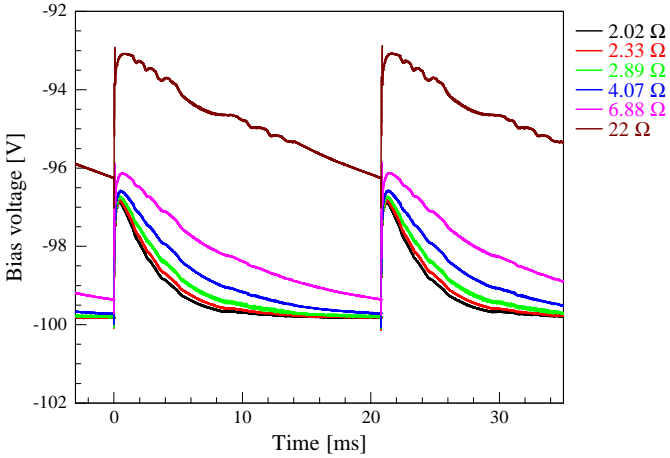


Figure V-3. Bias voltage recovery between two pulses using three capacitors

In order to evaluate the voltage loss of bias due to the RC circuit has been measured the difference between the voltage nominal value (-100V) and the real voltage value at different time lapses (5ms, 10ms, 15ms and 20ms) after the discharge.

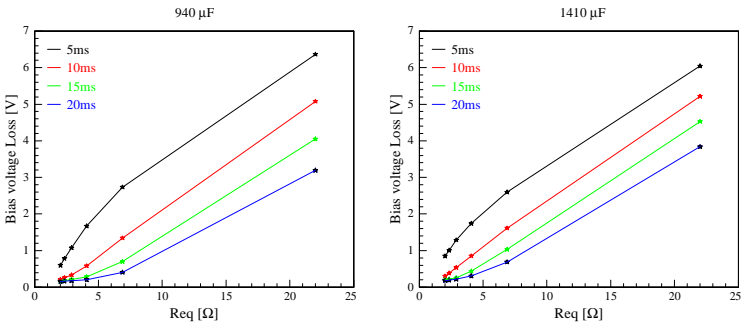


Figure V-4. Bias voltage recovery

The Figure V-4 shows the drop of voltage for different bias circuit configurations. The goal is find the best configuration of resistance and capacitance that reduces as possible the time recovery of voltage bias.

It has been chosen the configuration with 2.02Ω and $940\mu\text{F}$ because that allows to provide the required charge and it has the faster response.

5.2.2 Copper target HiPIMS discharge characterization

The investigation about electrical characteristics of HiPIMS discharge applied to Copper target has been made using Hüttinger power supply with following parameters:

- Pulse Voltage: 750V, 800V, 850V
- Pulse width: $50\mu\text{s}$, $75\mu\text{s}$, $100\mu\text{s}$
- Target-substrate distance: from 210mm to 90mm with 20mm step

The Argon pressure is $4.5 \cdot 10^{-3}$ mbar the same used in deposition process.

The DC Bias voltage is -100V using the configuration 2.02Ω and $940\mu\text{F}$ the same used in deposition process.

In Figure V-5, Figure V-6 and Figure V-7, are reported, HiPIMS voltage and current and sample holder pick-up voltage and current at 210mm, 150mm and 110mm sample holder-magnetron distance respectively.

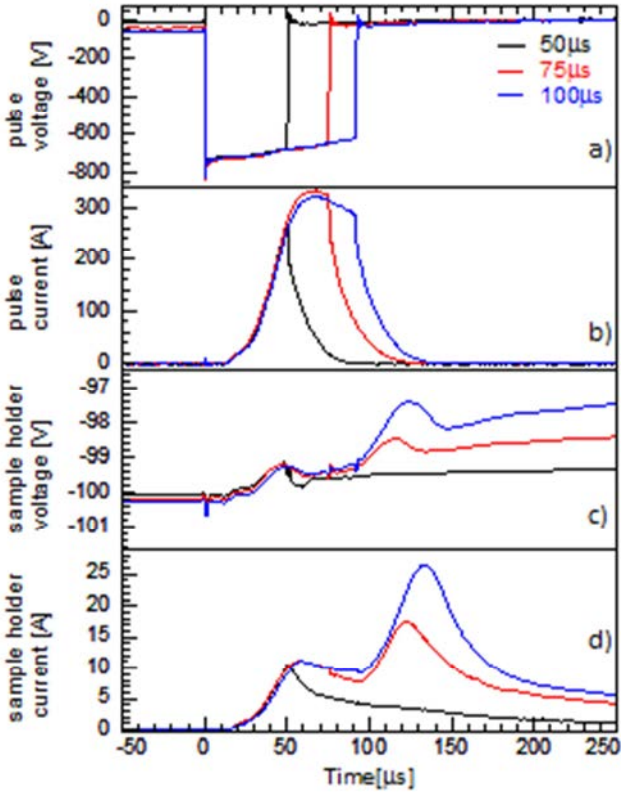


Figure V-5. Cu discharge HiPIMS voltage a) and current b) and corresponding sample holder pick-up voltage c) and current d) with 210mm sample-magnetron distance

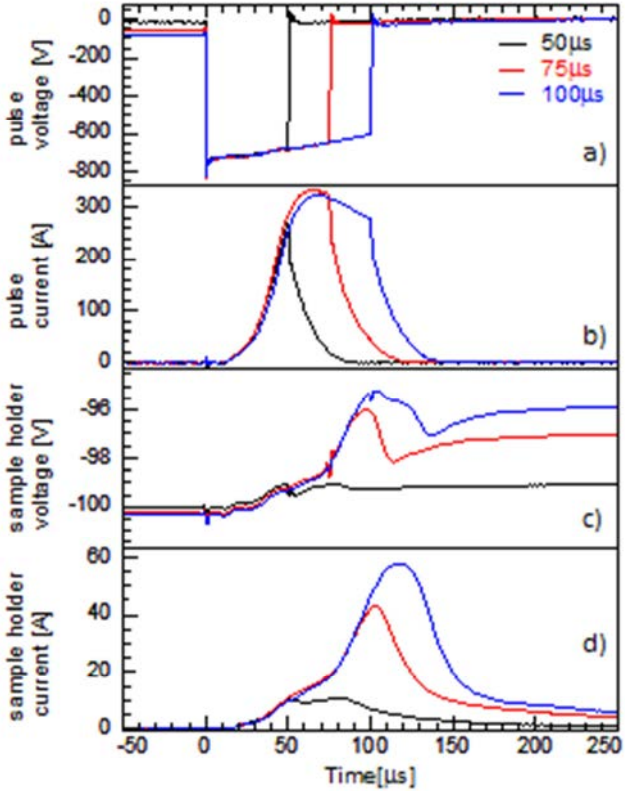


Figure V-6. Cu discharge HiPIMS voltage a) and current b) and corresponding sample holder pick-up voltage b) and current d) with 150mm sample-magnetron distance

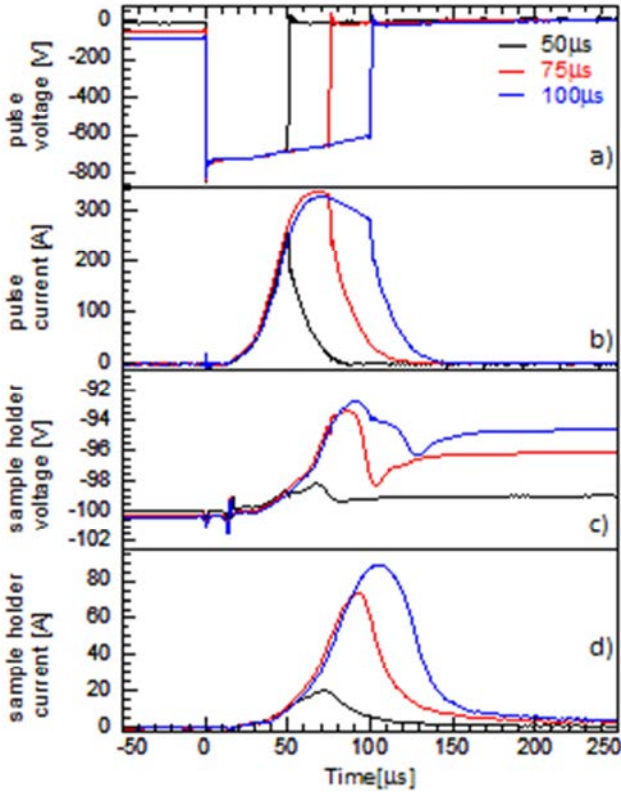


Figure V-7. Cu discharge HiPIMS voltage a) and current b) and corresponding sample holder pick-up voltage b) and current d) with 110mm sample-magnetron distance

	Voltage [V]	Pulse width [us]	Distance [mm]
1	750	50	90-210
2	750	75	90-210
3	750	100	90-210
4	800	50	90-210
5	800	75	90-210
6	800	100	90-210
7	850	50	90-210
8	850	75	90-210
9	850	100	90-210

Table V-3. Different power supply parameters and distance configurations

	90mm [J]	110mm [J]	130mm [J]	150mm [J]	170mm [J]	190mm [J]	210mm [J]	Average [J]
1	2.16	2.27	2.55	2.57	2.74	2.61	2.64	2.51
2	8.20	7.95	7.85	8.18	8.20	8.25	8.13	8.11
3	12.21	12.12	12.39	12.15	12.35	12.09	10.81	12.02
4	4.60	4.25	4.62	4.80	4.77	4.52	4.72	4.61
5	10.94	10.48	10.58	10.65	10.70	10.50	10.68	10.65
6	15.95	15.69	15.67	15.74	15.57	15.65	15.63	15.70
7	7.11	6.69	7.01	6.82	6.89	6.96	6.93	6.92
8	13.93	13.79	13.75	13.65	13.72	13.33	13.67	13.69
9	19.23	19.22	19.06	19.20	18.96	19.01	18.97	19.09

Table V-4. Pulse energy [J] for each measure configuration

For each measurement has been calculated the error based to the instability of current pulse (less than 2us). Using this parameters the error is fixed to 4% for configuration with 50us pulse width, 3% for 75us and 2% for 100us.

The same percentage will be used for the current data.

The value of HiPIMS magnetron pulse energy [J] and magnetron charge [mC] is calculated by the power supply output current and power integral.

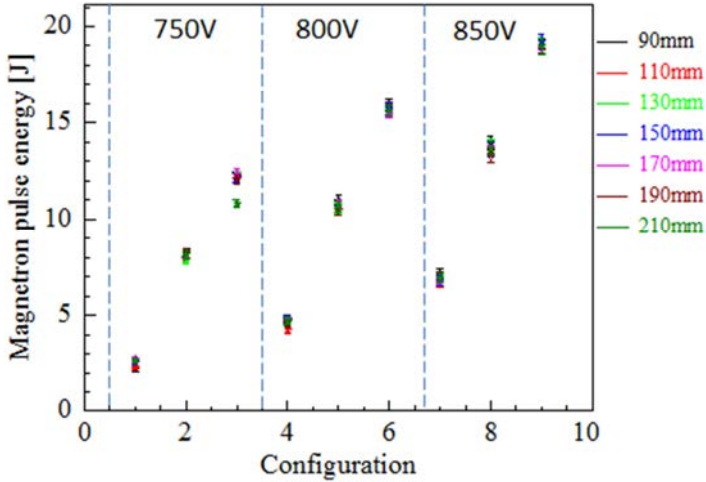


Figure V-8. Pulse Energy [J] for different configuration referred to Table V-4

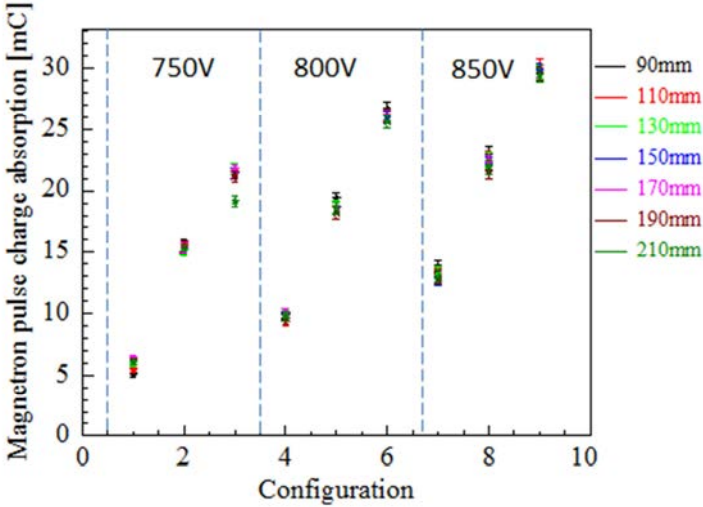


Figure V-9 Magnetron charge absorption [mC] for different configuration referred to Table V-3

Figure V-8 and Figure V-9 show that the magnetron-sample distance variation doesn't change the pulse energy and magnetron charge respectively, when the same power supply parameters are used.

As usual in sputtering technique the discharge parameters are expressed in current and power density. The normalization based on target area permits the comparison between magnetron with different size.

The area of used magnetrons is 324.5cm^2 ($24.4 \times 13.3\text{cm}$). The calculation of current and power density is commonly used the nominal area and the peak current and power value.

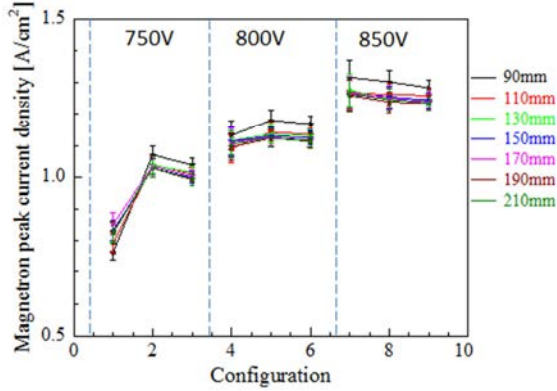


Figure V-10. Peak current density for different configurations

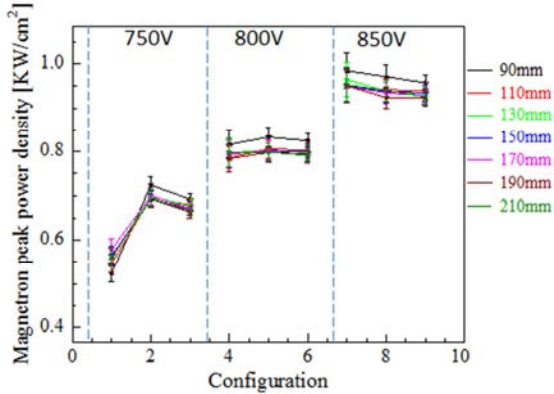


Figure V-11. Peak power density for different configurations

The sample holder current has been raise more interest. As shown in Figure V-5, Figure V-6 and Figure V-7 d) the current on sample holder exhibits an higher second peak (more pronounced in Figure V-5). The maximum of second peak is strong dependent by the pulse width, whereas the position depends by the magnetron-sample distance.

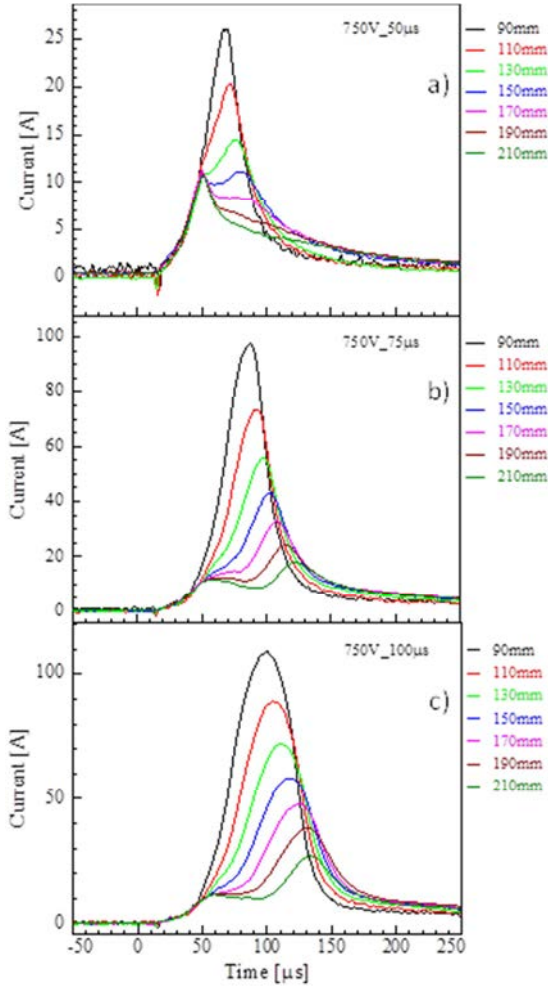


Figure V-12. sample holder current evolution as function of magnetron-sample distance. a) 750V and 50μs pulse width; b) 750V and 75μs pulse width; c) 750V and 100μs pulse width;

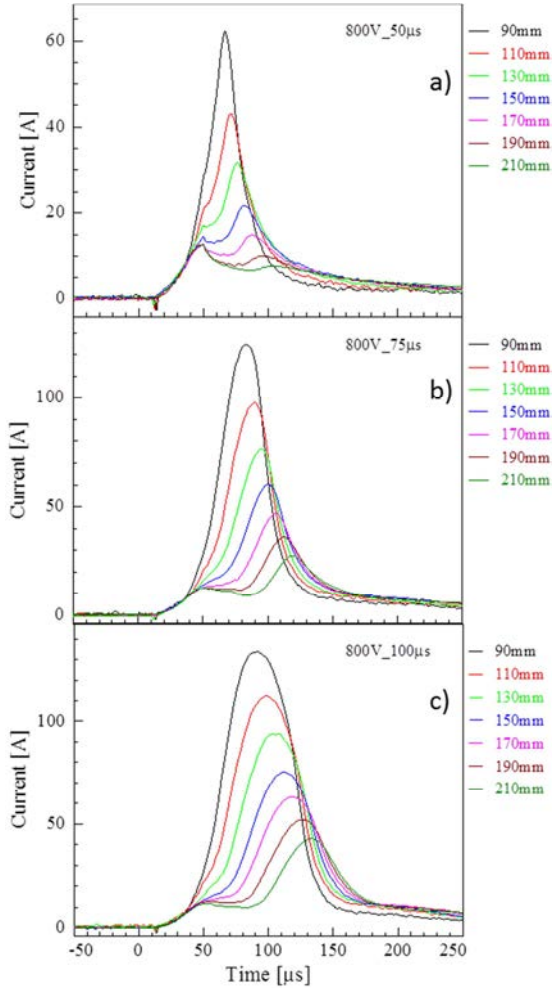


Figure V-13. sample holder current evolution as function of magnetron-sample distance. a) 800V and 50us pulse width; b) 800V and 75us pulse width; c) 800V and 100us pulse width;

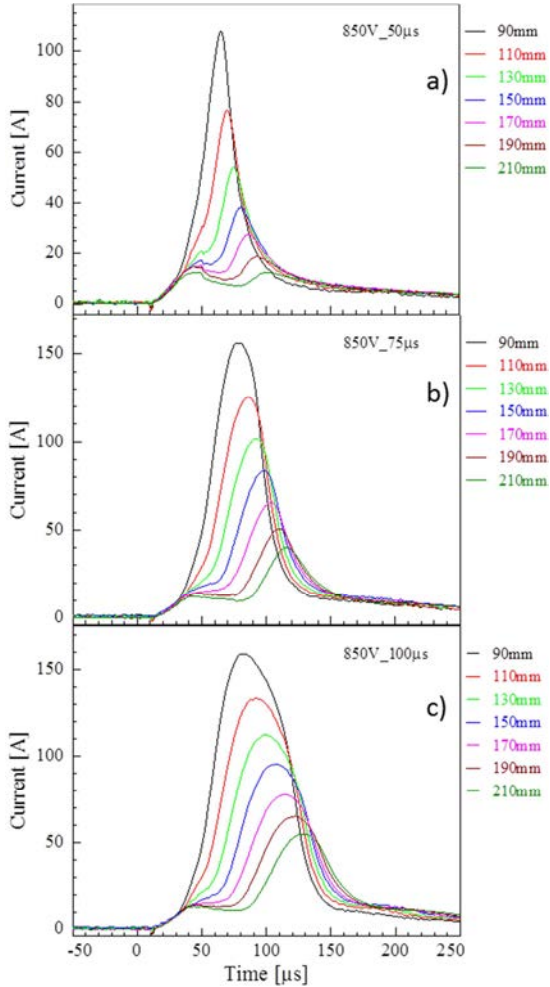


Figure V-14. sample holder current evolution as function of magnetron-sample distance. a) 850V and 50us pulse width; b) 850V and 75us pulse width; c) 850V and 100us pulse width;

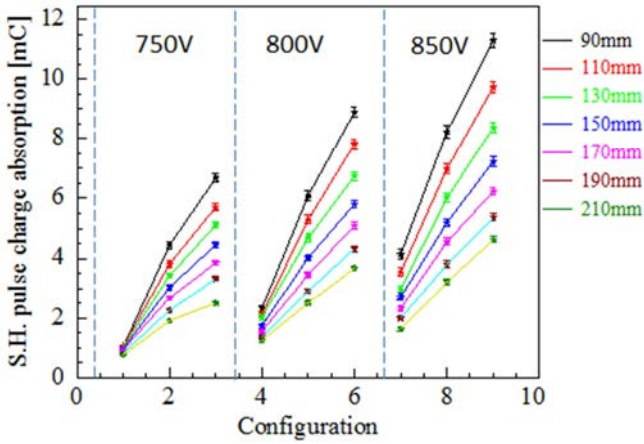


Figure V-15. Sample holder pulse charge absorption in different related to configuration

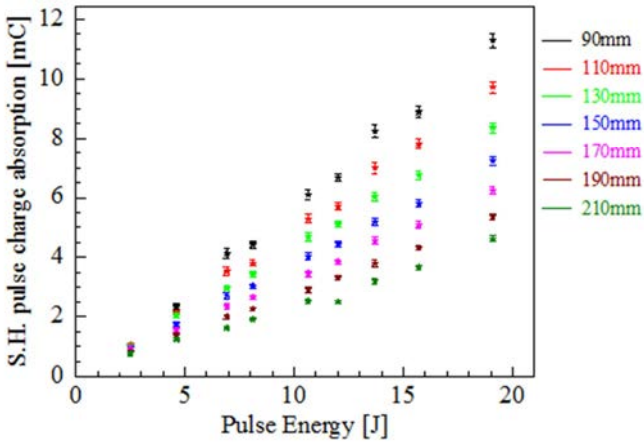


Figure V-16. Sample holder pulse charge absorption related to HiPIMS pulse energy

In Figure V-15 and Figure V-16 are reported the charge absorbed by the sample holder during the HiPIMS discharge, these are referred to configuration and power supply pulse energy respectively. The value of charge is calculated by the sample holder current integral.

Compared to magnetron charge Figure V-9 it is clear that the distance plays an essential role on sample holder pickup current.

This phenomenon may be explained by the magnetron close field configuration, because changing the magnetron-sample distance the distance between the two magnetron is also reduced and the magnetic field increases.

As result of higher magnetic field confinement is an higher plasma density close to sample holder, that results in higher bombardment ratio.

Evaluate an accurate value of ion bombardment ratio is not possible in this case due to different reasons:

- 1) The current value is time dependent and applying the common used expression J_i/J_a (where J_a indicates the neutral atoms flux and J_i the ions flux), it is not correct because it is not reported that the ion bombardment and deposition rate have the same trend.
The only information may be extrapolate it is the ratio of the amount of bombardment charge and total thickness of coating.
- 2) The ion flux is not uniform on all sample surface, because the metal ion flux has a preferential direction.
- 3) In literature reliable data are not available about the secondary electrons emission yield for Copper and Molybdenum induced by metal ion in used voltage range.
- 4) The sample holder pickup current is the amount of the Argon ions and Metal ions contribution.

Some solution are feasible to resolve part of the problems.

About point 2) as example it is possible measure the pickup current simultaneously in two different points of sample holder, one in front of magnetron and one shadowed by sample holder.

Regard to the point 4) it is possible correlate the OES time resolved (see cap. 5.2) with the sample holder pickup. This point has to be deepened because the photon emission probability of different species in HiPIMS discharge is not define yet.

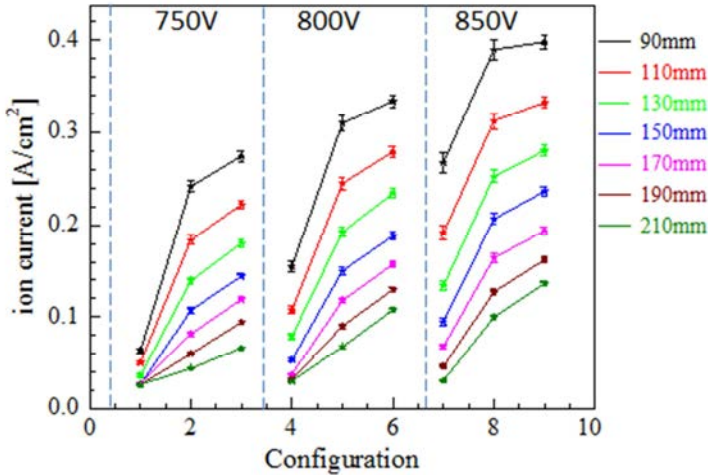


Figure V-17. bombardment ion current density

The data in Figure V-17 have been calculated using the maximum value of sample holder pickup current and the surface of sample holder, roughly 400cm^2 .

It is important taking into account the following approximation:

- All surface of sample holder is bombarded with homogeneous current
- All current is due to positive charged ions, secondary electron emission is negligible [123], [124].
- Negligible part of double charged ions

5.2.3 Molybdenum target HiPIMS discharge characterization

The investigation about electrical characteristics of HiPIMS discharge applied to Molybdenum target has been made using Sinex 1.2 power supply.

The simplicity of this device, exception to a triac there are not electronic component, reproduce the scheme in Figure II-7.

In this power supply the input voltage is the only one changeable parameter, it is expressed in $x/260$ Vac, using a heavy dimmer. Where Vac is the value of standard power grid (230Vac).

The measurements have been made with following parameters:

- Vac: from 80Vac to 200Vac
- Target-substrate distance: from 210mm to 90mm with 20mm step

The Argon pressure used is $4.5 \cdot 10^{-3}$ mbar, it is the same used in deposition process.

The DC Bias voltage is set to -100V using the configuration 2.02Ω and $940\mu\text{F}$, it is the same used in deposition process.

In Figure V-18, Figure V-19, and Figure V-20 are reported HiPIMS voltage and current and sample holder pick-up voltage and current at 210mm, 150mm and 110mm sample holder-magnetron distance respectively.

The different power supply hardware architecture basically, defines the voltage pulse shape. It is clearly comparing the Figure V-5 a) with Figure V-18 a).

As a matter of fact the HiPIMS pulse of Hüttinger has a step shape, it is due to its electronic pulse management. Otherwise in Sinex, where there isn't electronic components, the voltage pulse shape is due to the direct connection of capacitor circuit to the magnetron. The inductance permits to reduce the current flow and avoid the arc discharge mode.

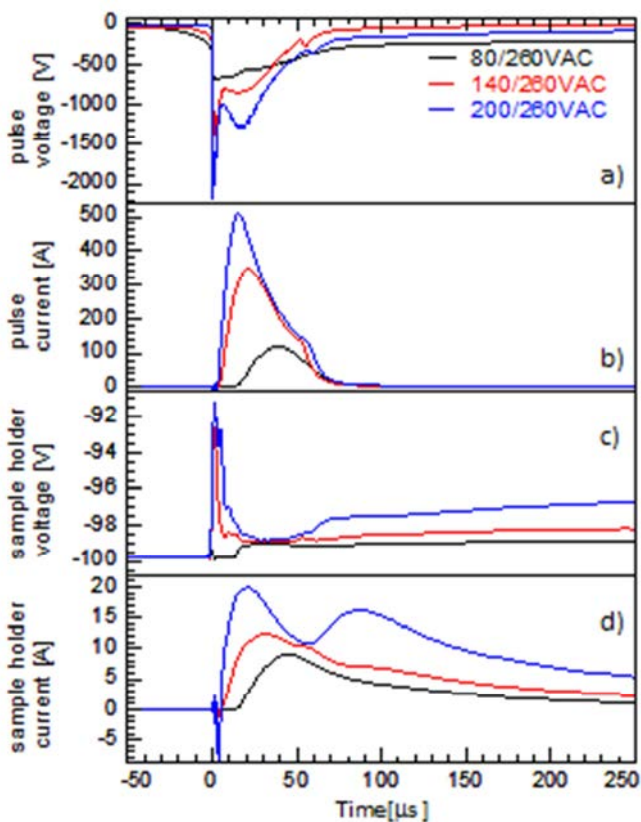


Figure V-18. Mo discharge HiPIMS voltage a) and current b) and corresponding sample holder pick-up voltage c) and current d) with 210mm sample-magnetron distance

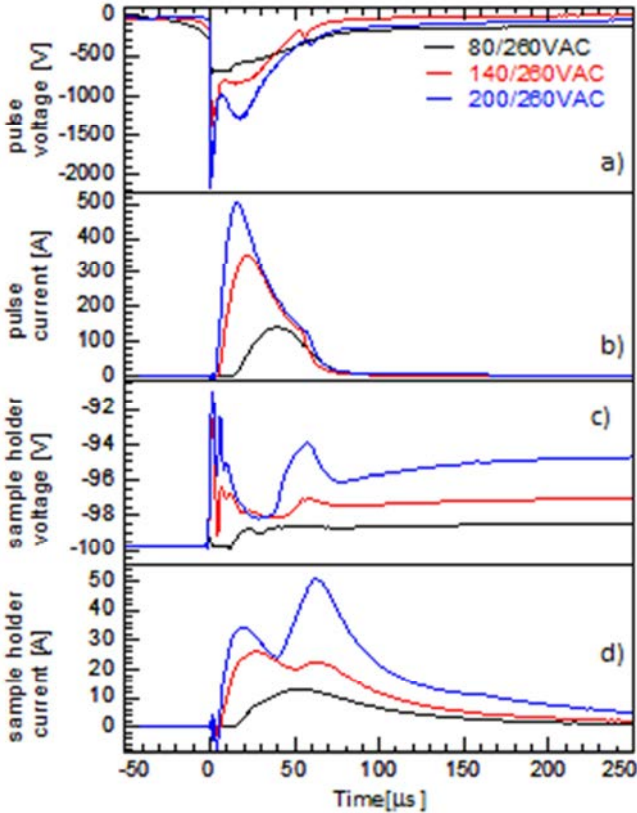


Figure V-19. Mo discharge HiPIMS voltage a) and current b) and corresponding sample holder pick-up voltage c) and current d) with 150mm sample-magnetron distance

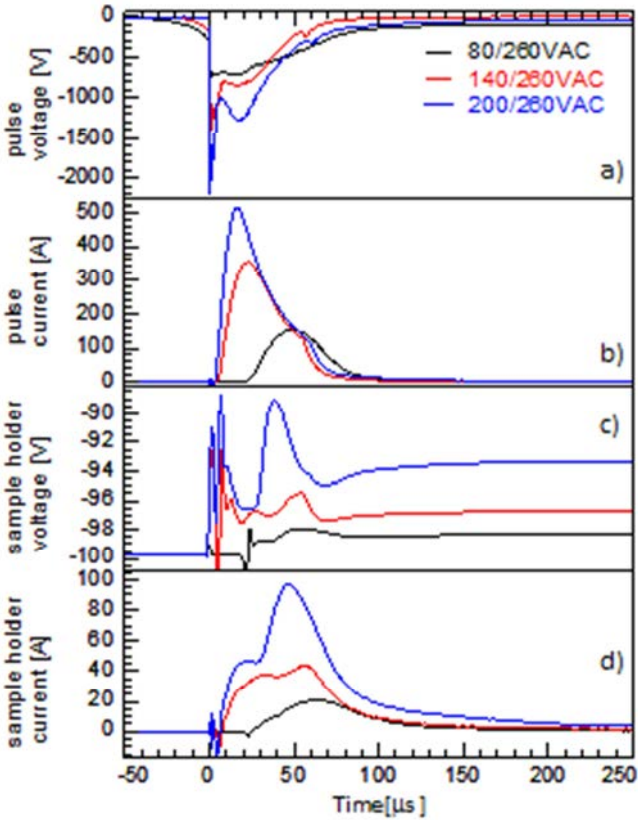


Figure V-20. Mo discharge HiPIMS voltage a) and current b) and corresponding sample holder pick-up voltage c) and current d) with 110mm sample-magnetron distance

	Voltage [Vac]	Distance [mm]
1	80	90-210
2	90	90-210
3	100	90-210
4	110	90-210
5	120	90-210
6	130	90-210
7	140	90-210
8	150	90-210
9	160	90-210
10	170	90-210
11	180	90-210
12	190	90-210
13	200	90-210

Table V-5. Different power supply used for different configurations

Due to the basic architecture of this power supply, the discharge in different configurations reported in Table V-5 differs in magnetron-sample holder distance and in voltage input. The maximum of Vac value (200Vac) is due to the recurring development of breakdown on sample holder and magnetron surface.

Differently, to more stable Hüttinger HiPIMS discharge, Sinex discharge is more noised and susceptible to fluctuations, on account of this, the error is fixed to 6%.

	90mm [J]	110mm [J]	130mm [J]	150mm [J]	170mm [J]	190mm [J]	210mm [J]	Average [J]	Vac [V]
1	2.63	2.56	2.48	2.39	2.29	2.33	2.18	2.41	80
2	3.32	3.26	3.10	3.07	2.99	2.99	2.98	3.10	90
3	4.02	3.97	3.95	3.91	3.87	3.81	3.76	3.90	100
4	4.87	4.73	4.80	4.77	4.73	4.81	4.72	4.78	110
5	5.66	5.61	5.63	5.62	5.59	5.65	5.71	5.64	120
6	6.60	6.56	6.58	6.65	6.64	6.59	6.53	6.59	130
7	7.66	7.55	7.62	7.58	7.49	7.67	7.54	7.59	140
8	8.67	8.71	8.70	8.73	8.60	8.66	8.74	8.69	150
9	9.84	9.82	9.74	9.71	9.81	9.80	9.89	9.80	160
10	11.18	11.01	10.99	11.02	11.06	11.01	11.11	11.05	170
11	12.40	12.37	12.39	12.34	12.34	12.50	12.36	12.39	180
12	13.97	13.63	13.77	13.71	13.68	13.75	13.72	13.75	190
13	15.32	15.26	15.26	15.09	15.29	15.25	15.22	15.24	200

Table V-6. Pulse energy [J] for each measure configuration

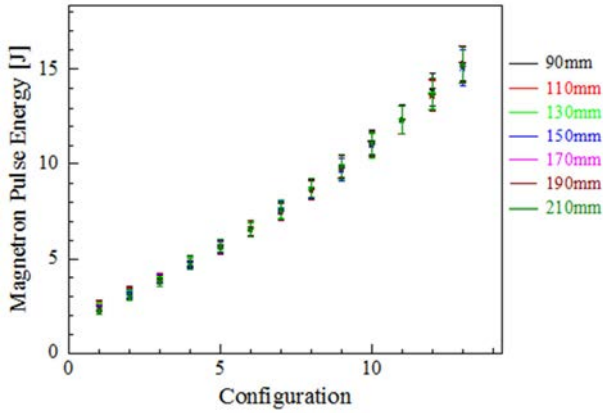


Figure V-21. Pulse Energy [J] for different configuration referred to Table V-6

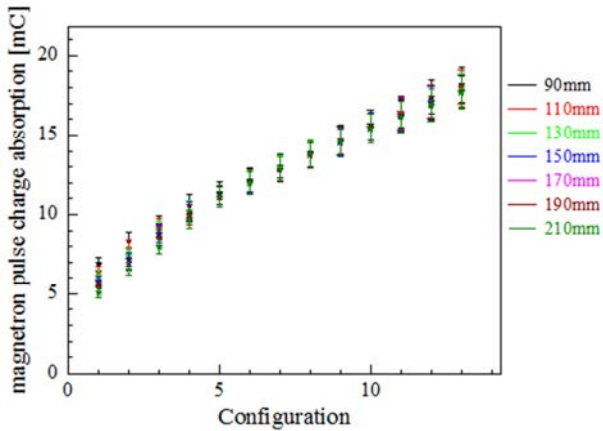


Figure V-22. Magnetron charge absorption [mC] for different configuration referred to Table V-5

Differently to Cu HiPIMS discharge using Hüttinger, the lack of power supply setting parameters in Sinex is traduced in more coherent growth of pulse energy related to input power.

Same as Cu HiPIMS discharge, the power and current density of Mo HiPIMS discharge are reported.

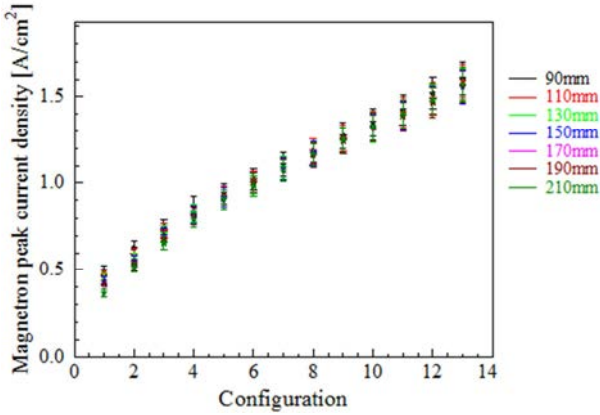


Figure V-23. Peak current density for different condigurations

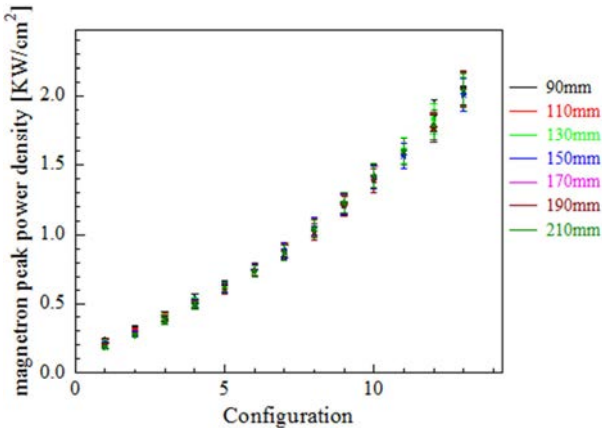


Figure V-24. Peak power density for different condigurations

As shown in Figure V-23 and Figure V-24, there is a different trend of current and power density growth. This behavior may be explained by the different increment in the voltage value. In fact the Sinex pulse is not managed by electronics device like Hüttinger, that provides to a constant voltage value. Furthermore the ignition time of discharge decreases with the voltage increment Figure V-27.

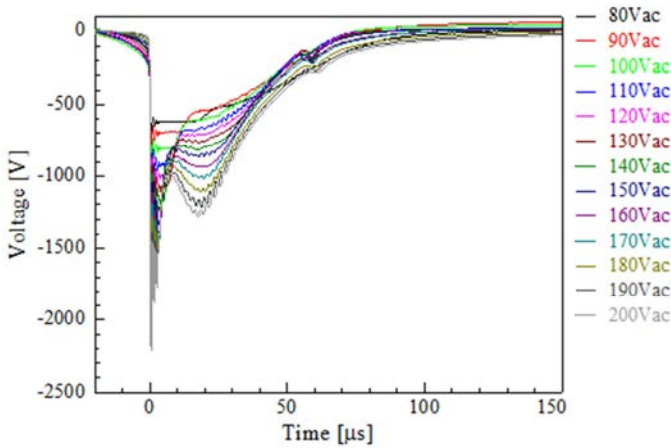


Figure V-25. Voltage pulse shapes related to different input Vac

Comparing the Figure V-23 and Figure V-27 it is possible understand that the magnetron current is inversely proportional to the ignition delay of discharge.

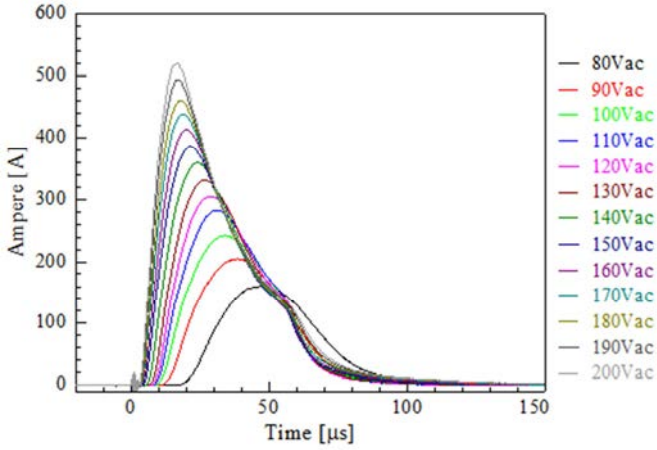


Figure V-26. Current pulse shapes related to different input Vac

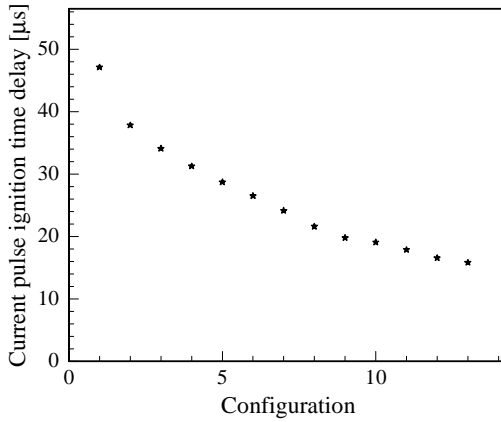


Figure V-27. Current pulse ignition time delay

About sample holder, it has been recognized the current pickup. The sample holder current pickup for the different configuration are reported in following figures.

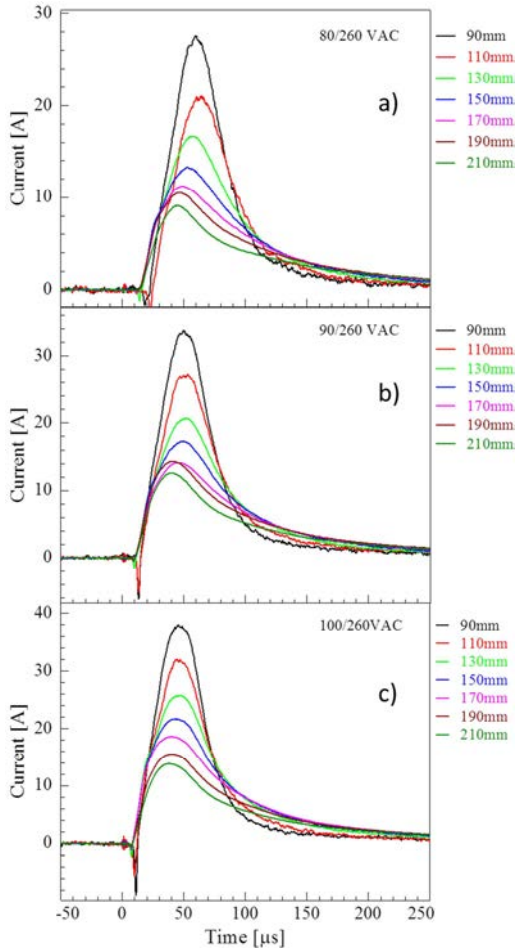


Figure V-28. Sample holder current pickup configurations 1 a), 2 b), 3 c)

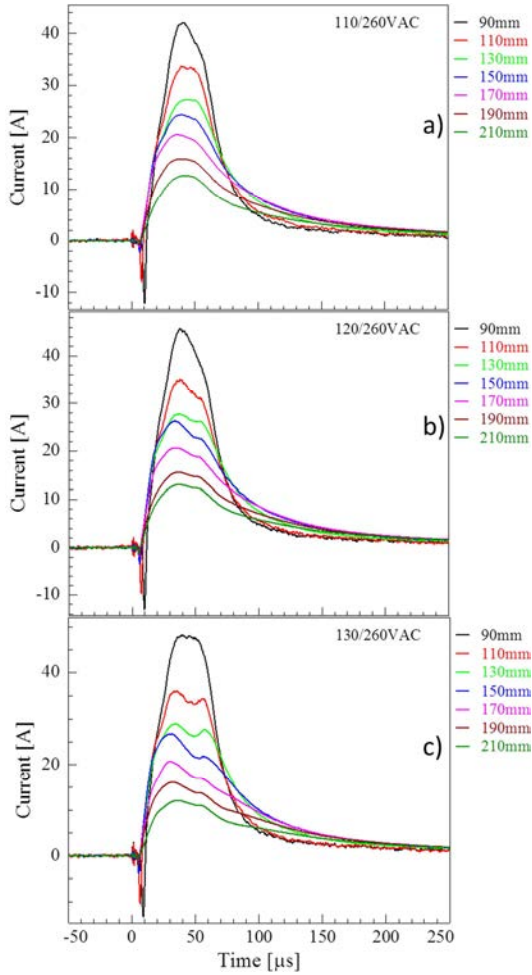


Figure V-29 Sample holder current pickup configurations 4 a), 5 b), 6 c)

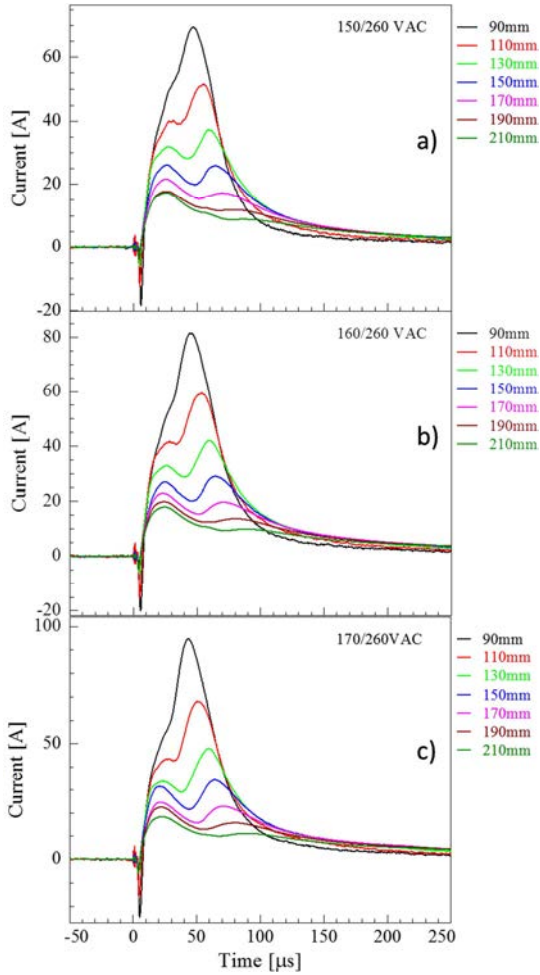


Figure V-30. Sample holder current pickup configurations 8 a), 9 b), 10 c)

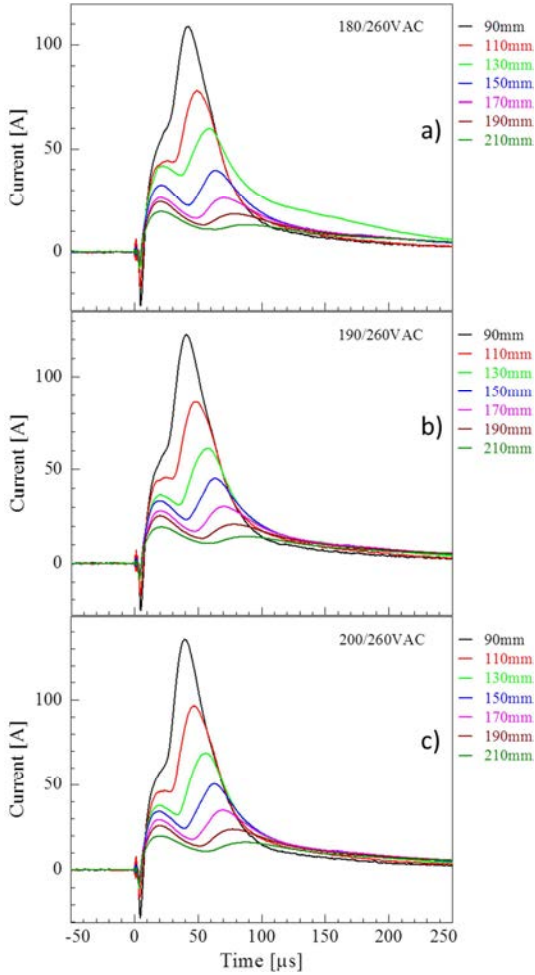


Figure V-31. Sample holder current pickup configurations 11 a), 12 b), 13 c)

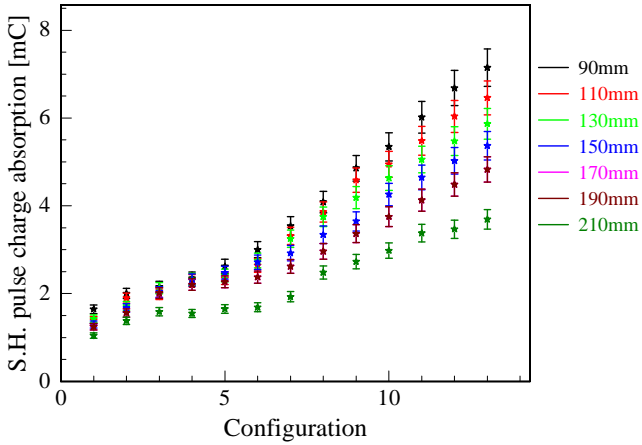


Figure V-32. Sample holder pulse charge absorption in different related to configuration

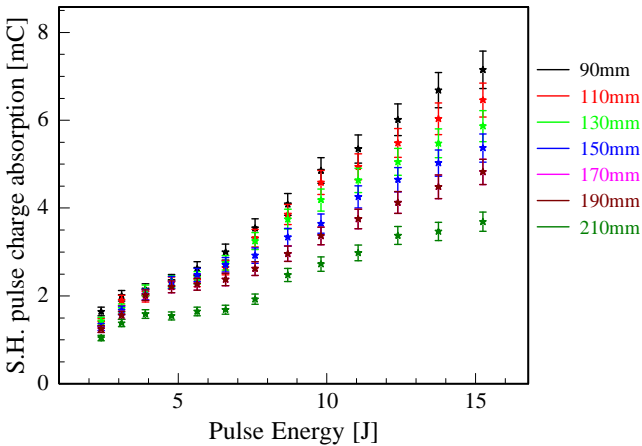


Figure V-33. Sample holder pulse charge absorption in different related to pulse energy

In Figure V-32 and Figure V-33 are reported the sample holder current integral pickup (total charge mC) for the different configuration. The increment of HiPIMS power discharge correspond to an increment of cumulated charge amount.

Furthermore it is clear in all magnetron-sample distant a change of slope close to configuration n°5 equivalent to 120Vac (5.6 J), that is the same configuration where the second peak in sample holder pickup current appears (Figure V-29b).

In order to complete the discharge diagnostic in Figure V-34, it is reported the ion flux that reaches the sample holder. It is also referred to the sample holder peak current maximum.

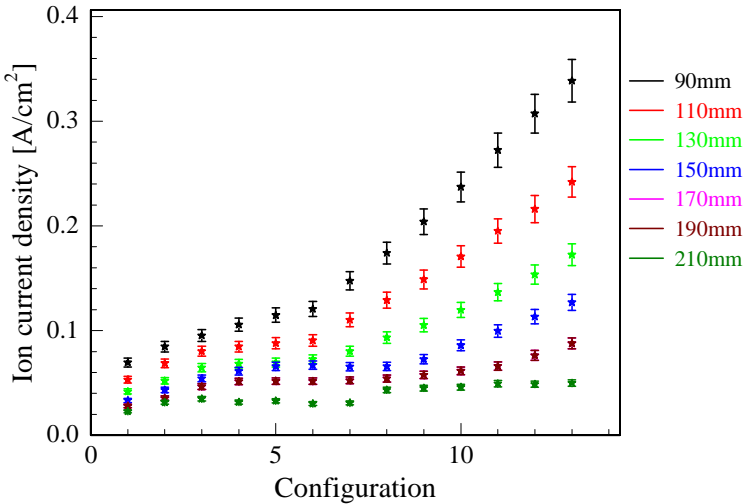


Figure V-34.bombardment ion current density

Chapter VI

Optical Emission Spectroscopy in HiPIMS Discharge

6.1 Introduction

Optical emission spectroscopy (OES) is the study and measurement of light emitted during relaxation of atom, ion and molecule.

A particle, in higher energy quantum mechanical state, returns to a lower one with the emission of a photon. The frequency of emitted photon is equal to the energy difference between the two quantum state, since the energy conservation equation.

$$\Delta E = h\nu \quad \text{VI-1)}$$

There are several possible electron transition for each atom, and the energy between to different quantum state is characteristic and univocal of a specific atom.

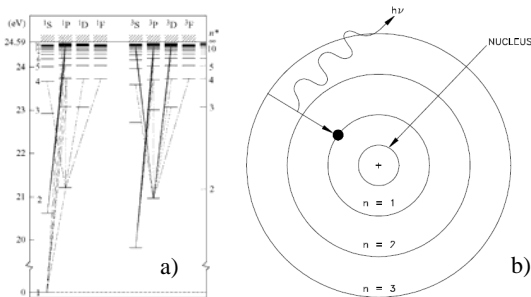


Figure VI-1. exemple of energy-level diagram of neutral helium a) and Bohr model b)[125]

The OES generally return as result a spectra, that shows the light intensity vs light wavelength, but it is possible to have information about the single line in time resolved mode [126][127][128].

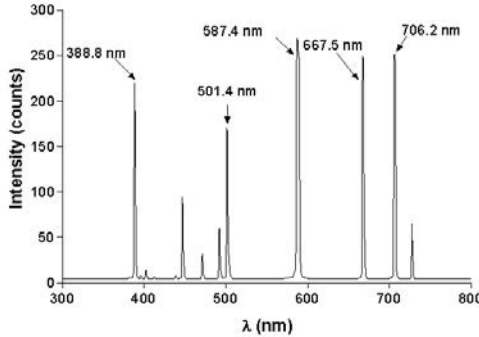


Figure VI-2. example of helium spectrum in visible range

OES in glow discharge essentially is the measurement of the light intensity produced by the plasma. The intensity depends by the density of exited specie (N_i), spontaneous emission probability (A_{ij}), the wavelength (ν_{ij}) and Planck constant (h). The indexes i and j are referred to high and low energy state of transition [129]

$$I_{ij} = N_i A_{ij} h \nu_{ij} \quad \text{VI-2)}$$

The density of exited specie (N_i), more precisely, is not a constant, but it is a function. That depends of excitation state of plasma and it is related to the electron energy distribution function (EEDF). In other hands describes the possibility of an electron to impact with an atom and cause the excitation.

It is important remember that, in a real measurement the intensity is affected by the response and the absorption of the acquisition apparatus (lens, filters, monochromator, PMT, CCD...). In this case it is necessary add another constant to eq. VI-2) after a characterization and calibration of acquisition system.

In standard OES measurement, the intensity is average of the signal that coming from the cylindrical or conical volume in front of acquisition device

(optical fiber or detector), furthermore the spectral is time integrated, that means the signal is acquired in a time interval.

OES spectra, as signal integration, is useful to understand the composition of plasma and it provides the same information whether the light source is pulsed or continuous. Indeed it does not provide any information about the temporal evolution of the discharge.

This elementary setup is used commonly in the reactive process as optical emission monitoring (OEM). Where the injection of reactive gas is regulated by a feedback control, that uses the intensity of specific plasma line to maintain the discharge in transition regime of target hysteresis poisoning (see 2.2.3).

In HiPIMS discharge, where the plasma has a time evolution due to the pulsing nature, it is more interesting study the evolution of plasma species resolved in time.

This kind of measurement setup are more complicated than the simply OES, because it needs in addition a triggering system able to synchronize the optical acquisition with the HiPIMS discharge.

In this chapter will be describe setup and results of OES and OES time resolved in HiPIMS discharge.

6.2 Optical emission spectroscopy

6.2.1 OES Instrumentation setup

Using the deposition chamber described in cap. 4.1, the OES acquisition line has been developed.

The OES system is composed by:

- Optical fiber cable, plastic-clad-silica ([Verity Instruments Inc.](#)) [130]
- Optical head with collimating quartz lens ([Verity Instruments Inc.](#))
- Vacuum Feedthroughs ([Verity Instruments Inc.](#))
- Spectrometers
- Optical fiber holder

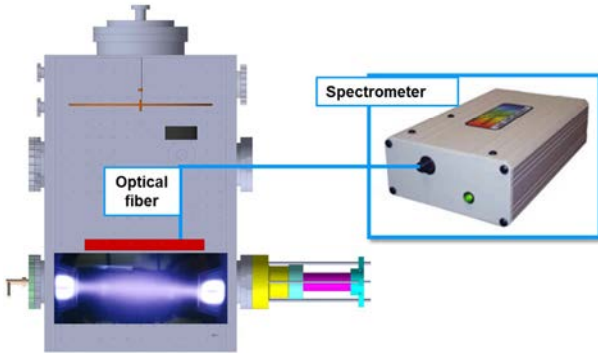


Figure VI-3. OES scheme setup

The optical fiber is positioned close to magnetron (10mm from ground shield), where the plasma density is higher and it has maximum light intensity.

For OES are used two different spectrometer:

- Spectrometer [Ocean Optics](#) model: Maya2000PRO [131] with bi-dimensional CCD array
Resolution: 0.9 nm
Spectral range from 200nm to 1100nm
- Spectrometer [Avantes](#) model: AvaSpec Multichannel Spectrometers [132]
Resolution: 0.2nm
Spectral range from 344nm to 736nm

OES recognition is made using the same parameters used for deposition too (cap. 7.2).

6.2.2 OES results

In OES of copper is used Avantes spectrometer, for this material are recognized DC spectrum and HiPIMS spectrum too, in order to understand the difference between the two different operating mode. It was chosen to use the same average power for both operating mode (1.5kW), as comparison parameter.

Power supply: Hüttinger 4001 Power: 1500W peak Voltage: 750V Pulse time: 75 μ s	Power supply: advanced energy MDX Power: 1500W Voltage: 390V Ampere: 4A
--	--

Table VI-1. Power supplies parameter for copper OES mesuraments

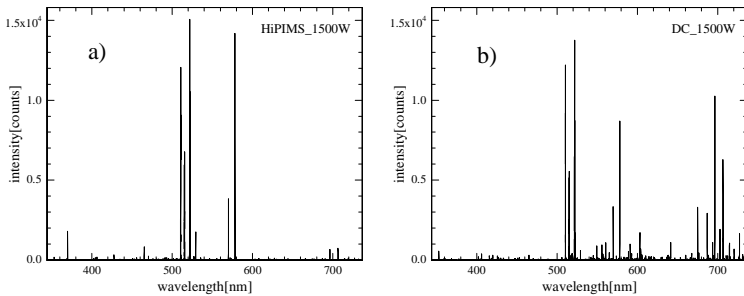


Figure VI-4. OES copper spectra: HiPIMS a) and DC b)

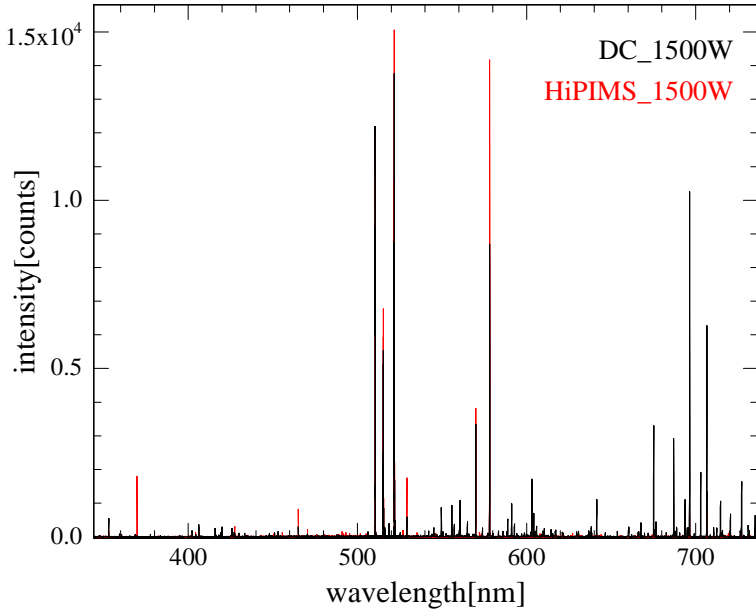


Figure VI-5. Coparation between DC and HiPIMS copper spectra

The analysis of Copper OES spectra has been concentrated on various ranges in order to evaluate the difference between the two discharge operating mode, the different ranges have been decided using NIST atomic spectra database [133]

- 1) CuI from 500nm to 550nm
- 2) CuII and ArII from 480nm to 500nm
- 3) ArI from 580nm to 610nm

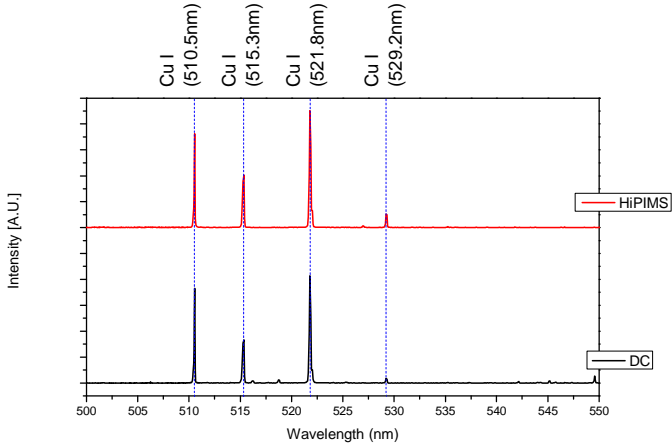


Figure VI-6. Range 1): CuI lines

Observing the previous spectra (Figure VI-4 - Figure VI-8) it is ascribe that:

- 1) The neutral copper line intensity increase in HiPIMS discharge
- 2) The presence of ionized copper in HiPIMS discharge
- 3) The reduction in intensity of neutral argon emission line in HiPIMS discharge, in according with literature[134][135]

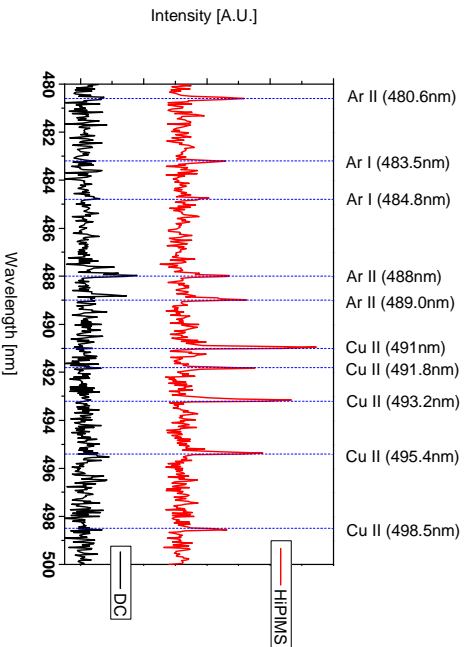


Figure VI-7. Range 2): CuII and ArII lines

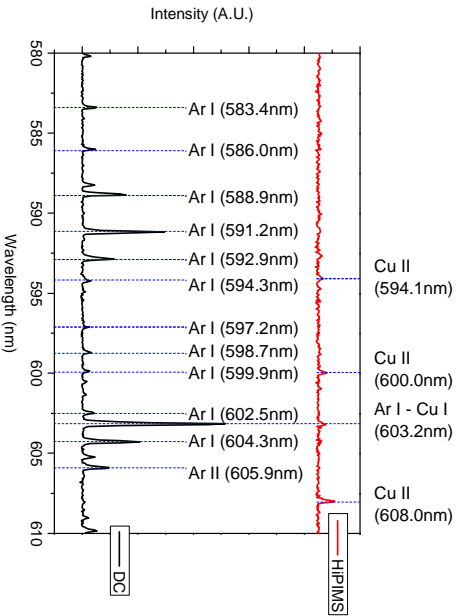


Figure VI-8. Range 3): CuII and ArI line

The same study has been done using the Ocean Optics spectrometer for Molybdenum target. Due to the low power throughput of the Sinex power supply, the measurements in DC mode has been done at 600W instead 1500W like in case of copper.

Power supply: Sinex 1.2 Power: 600W Peak Voltage: 1200V	Power supply: advanced energy MDX Power: 600W Voltage: 298V Ampere: 2A
---	--

Table VI-2. Power supplies parameter for Molybdenum OES mesuraments

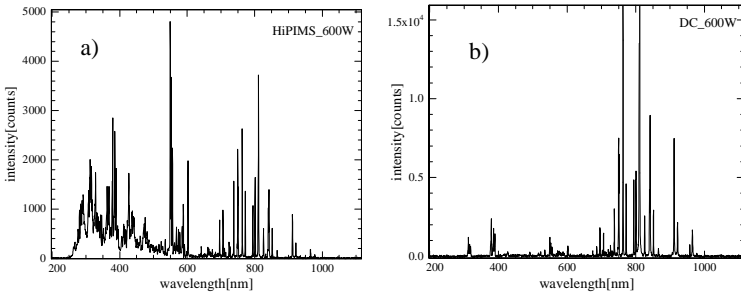


Figure VI-9. OES molybdenum spectra: HiPIMS a) and DC b)

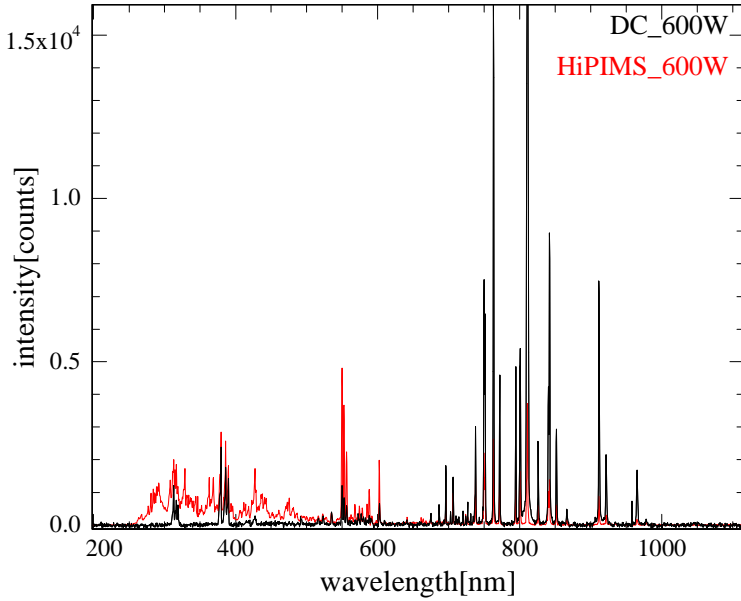


Figure VI-10. Coparation between DC and HiPIMS Molybdenum spectra

The analysis of Molybdenum OES spectra has been concentrated on various ranges in order to evaluate the difference between the two discharge operating mode:

- 1) MoI from 300nm to 340nm
- 2) MoII from 250m to 300m
- 3) ArII from 540nm to 590nm
- 4) ArI from 740nm to 920nm

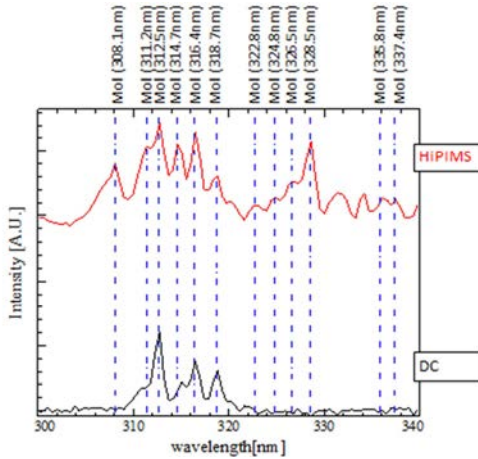


Figure VI-11. Range 1) Mol lines

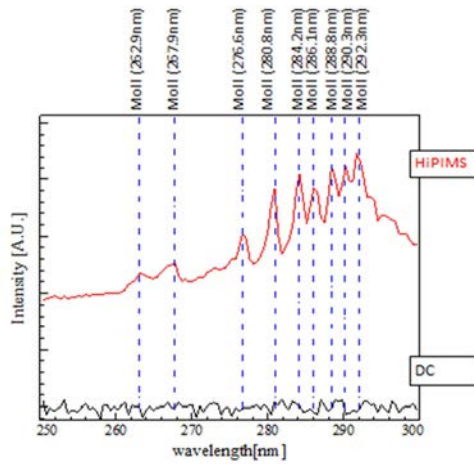


Figure VI-12. Range 2) MoII lines

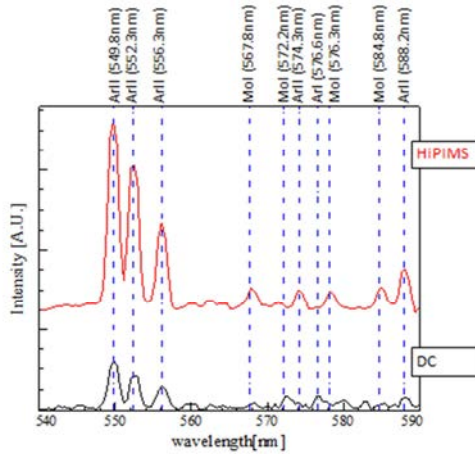


Figure VI-13. Range 3) ArII and MoI lines

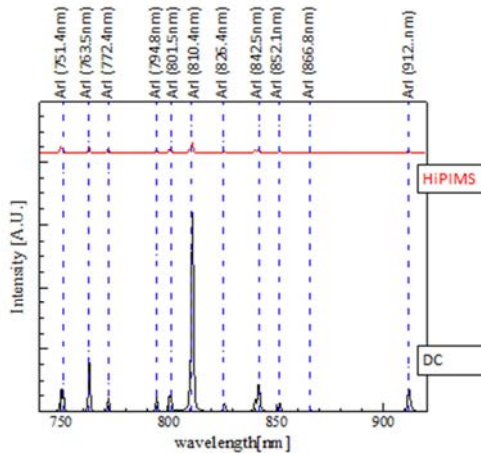


Figure VI-14. Range 4) ArI lines

The Molybdenum spectra analysis (

Figure VI-9 - Figure VI-14) it is ascribed that:

- 1) The neutral Molybdenum lines intensity increase in HiPIMS discharge
- 2) The presence of ionized Molybdenum in HiPIMS discharge and the completely absence in DC discharge
- 3) The increasing of intensity of ionized argon lines
- 4) The reduction in intensity of neutral argon emission line in HiPIMS discharge

It is confirmed the HiPIMS mode discharge, and the presence of sputtered metals ions.

6.3 Instrumentation setup OES time resolved

6.3.1 OES time resolved setup

In order to understand the plasma evolution in the HiPIMS discharge, it is decided to improve an OES time resolved (OES-TR) measurement line.

As mentioned in par 6.1, the OES time resolved requires a more complex setup than classical OES, due to the fast plasma evolution and the triggering system, that allows the synchronization between HiPIMS pulse and data acquisition.

Due to the low intensity of the light in each HiPIMS pulse, it is necessary to collect the signal of several pulses, merge the acquired data and create the OES-TR spectra. This is the main reason because developing a good and reliable triggering system is mandatory.

Unlike the standard OES, in OES-TR it is possible to acquire only one emission line selected by a monochromator.

The voltage and current curves recognition setup is the same described in cap 5.1.

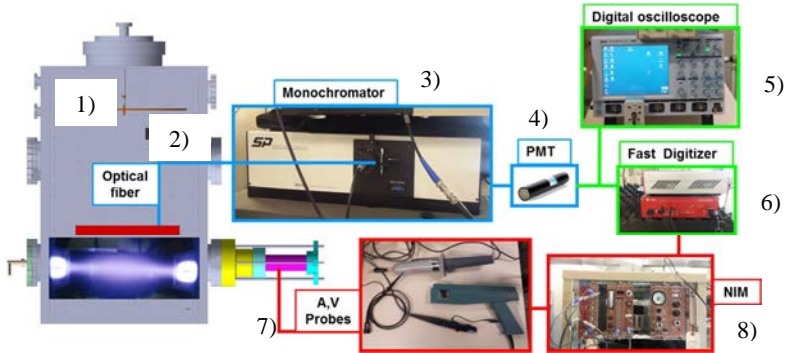


Figure VI-15. OES time resolved setup

In Figure VI-15 is reported the OES-TR scheme, in order to describe better the system, the different components are marked using different colors. The light blue line is used to indicate the optical acquisition line, the red line is used to indicate the triggering system and the green line for the acquisition step.

Starting from the plasma discharge in the chamber (1), the light is pulled out using an optical fiber (2) and directed to monochromator (3).

The optical fiber is positioned in different point and always orthogonal to the sputtering wind flux.

The monochromator receives the plasma emitted light, and using a grating that allows the emission light separation, it returns the selected wavelength.

Using a photomultiplier (4) (PMT) the “filtered light” that comes out from monochromator, is converted in an electrical signal. Finally the electrical signal is checked using a digital oscilloscope (5) and it is recorded in a PC hard drive memory using a fast digitizer (6).

The triggering system is a little more complex, because its aim is define the time zero of each HiPIMS pulse.

The current probe (7) signal is taken close to magnetron and it is manipulate using a Nuclear Instrument Module (8) (NIM), in order to make compatible the original current signal with operative range of fast digitizer. The NIM output results is a TTL signal, that define the time zero of each HiPIMS pulse.

About the triggering system, it is decided to use a threshold on current curve instead voltage signal, because the each HiPIMS pulses are not always identical.

As describe in 2.2.2 in HiPIMS discharge there is a time delay between current growth and applied voltage. The time delay is not always constant in each discharge and it causes an oscillation of current curve.

The maximum oscillation range of current is less than $2\mu\text{s}$ and it is calculated using the time at half maximum current value of each peak in a recognition of some hundreds current pulses.

It is assumed the plasma has the same characteristics at the same current value, and the use of a threshold on current as trigger (time 0 of pulse) guarantee that the acquired optical signal is referred to the same physical status of plasma.

The core of the acquisition line is the fast digitizer, this device permits to record in two separate channels the input signals (PMT and NIM TTL), in the same time and in continuous mode. The data flow is recorded on the PC memory in ascii files and these contain the set data of each event and the essential information, the trigger time tag. The two ascii files, one for the light signal (PMT) and the second for trigger (NIM), are elaborated using an ad-hoc software (cap 10.2), that returns a time resolved spectra.

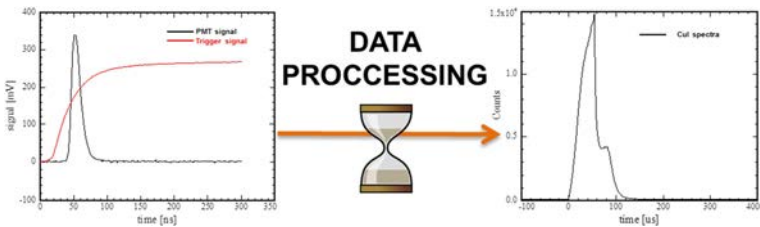


Figure VI-16. Events recorded by digitizer (left) and the final OES-TR spectra after data processing (right)

In Figure VI-16 (left) is reported an example of basic data events recorded by digitizer, the black line is the PMT pulse signal after the photon-current conversion, whereas the red line is the TTL output signal of NIM synchronized with the magnetron current signal.

In Figure VI-16 (right) is reported the OES-TR spectra after data processing by binning algorithm.

6.3.2 OES time resolved results

In this paragraph will be reported the results about OES-TR of copper and molybdenum. The parameters used to improve this analysis are the same used for the deposition process. (cap. 7.2).

The study OES has been done in two different configurations. In the first configuration the distance between magnetron and sample holder is 210mm. In the second configuration the distance is 110mm, that is the same used in deposition process.

Due to the mechanical setup and position of the optical fiber the data related to magnetron OES analysis are referred only to the first configuration.

Using the monochromator the spectrum resolution is higher than the spectrometer, but the range of survey is smaller due to the available gratings. As in standard OES it is used the NIST atomic spectra database [133], in order to select and choose the more useful lines for this experiment.

Selected Wavelength:

- ArI: 696.54nm
- ArII: 404.29nm
- CuI: 510.55nm
- CuII: 505.41nm
- MoI: 313.26nm
- MoII: 292.34nm

The measurement consist in 5 minutes of constant acquisition using the digitizer, that return two ascii files, one about the optical signal and one about the TTL trigger. Moreover for each measurement power supply throughput current, power supply throughput voltage, current absorbed by the biased sample holder and TTL signal have been recorded. That is essential to compensate the delay between the power supply pulse and the TTL trigger.

As a matter all the OES time resolved are referred to the time zero of voltage pulse.

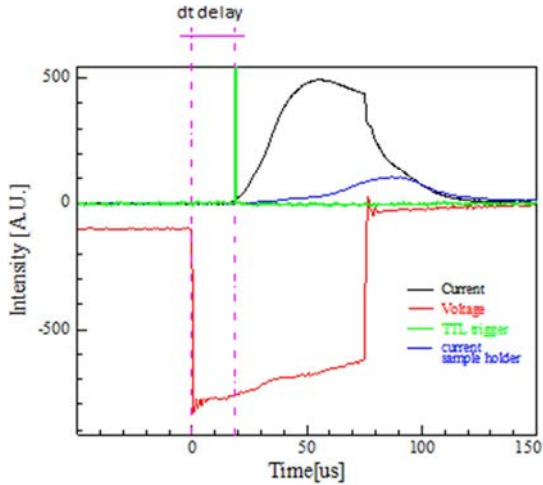


Figure VI-17. Example of electrical curves acquired for OES time resolved post processing, the “dt” time delay is determined by the SCA (single channel analyzer) threshold.

Experimental parameters:

- Monochromator DK240 spectral products:
 - Entrance slits: 50 μm
 - Exit slits: 100 μm
 - Grating n° 3 (see appendix 9)
- PMT power supply (see appendix 9): -1000V
- Power supply for Copper target: Hüttinger 4001
 - Voltage: 800V
 - Pulse width: 75 μs
 - Pulse frequency: 48Hz
- Power supply for Molybdenum target: Sinex 1.2
 - Voltage: 160VAC (1000V)
 - Pulse width: self-managed
 - Pulse frequency: 50Hz
- Bias Voltage: -100V

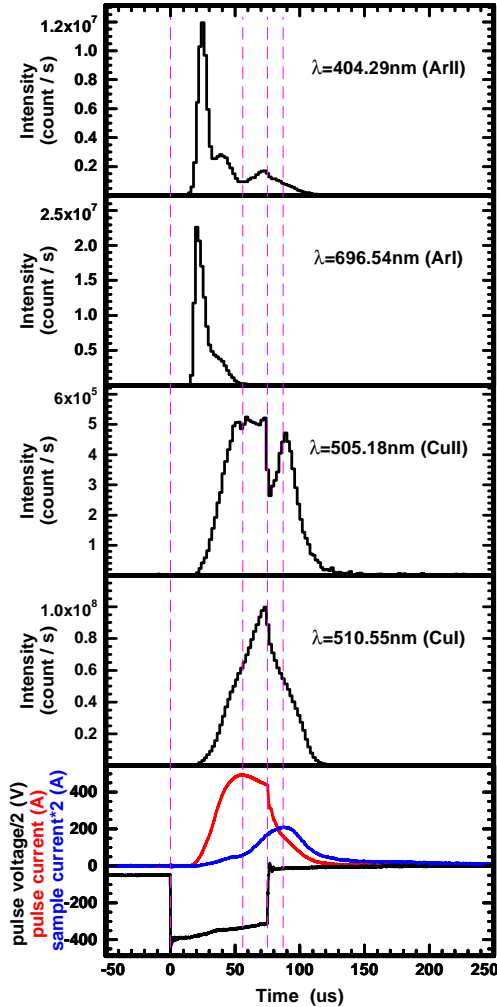


Figure VI-18. OES time resolved of Copper HiPIMS discharge close to sample holder, distance 11cm, binning time $2\mu\text{s}$

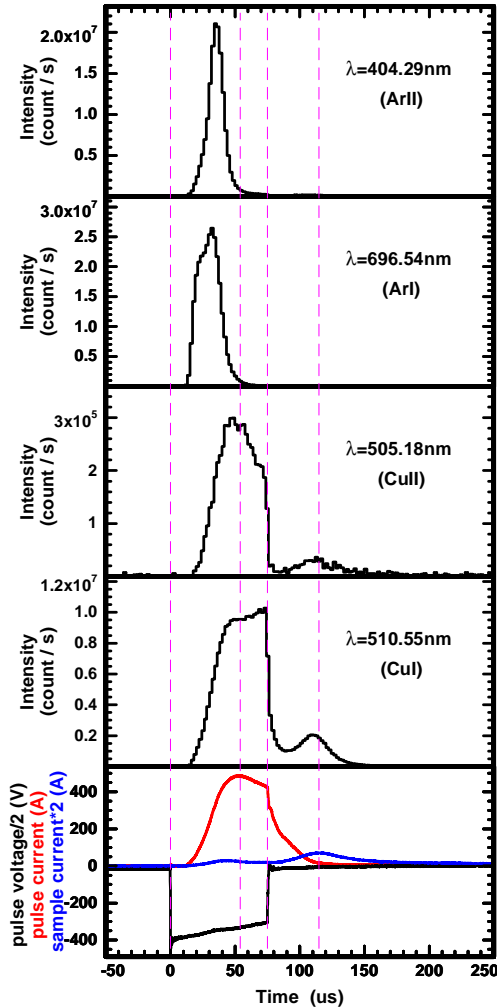


Figure VI-19. OES time resolved of Copper HiPIMS discharge close to sample holder, sample-magnetron distance 21cm, binning time $2\mu\text{s}$

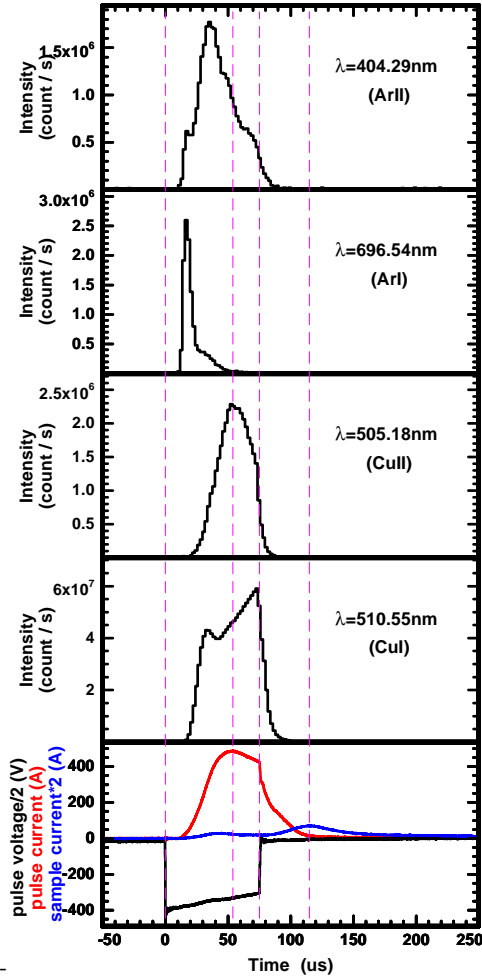


Figure VI-20. OES time resolved of Copper HiPIMS discharge close to magnetron, sample-magnetron distance 21cm, binning time 2 μ s

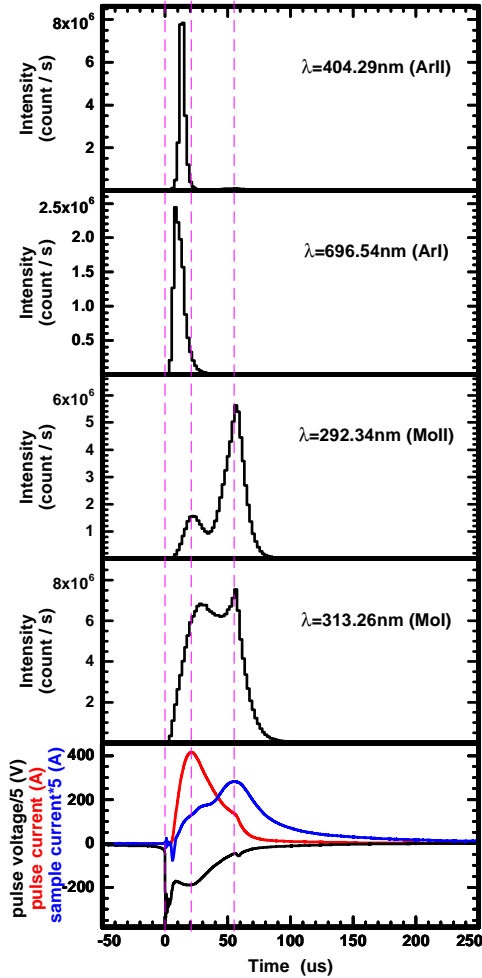


Figure VI-21. OES time resolved of Molybdenum HiPIMS discharge close to sample holder, sample-magnetron distance 11cm, binning time 2 μs

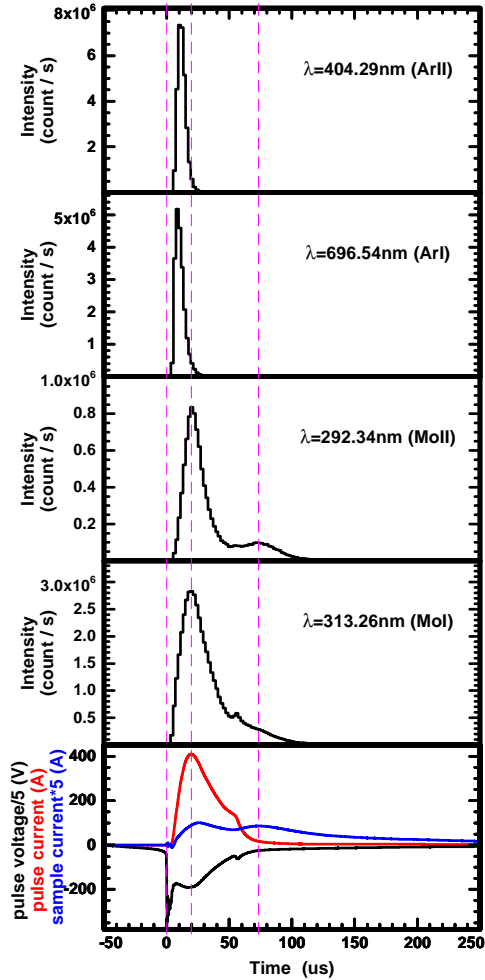


Figure VI-22. OES time resolved of Molybdenum HiPIMS discharge close to sample holder, sample-magnetron distance 21cm, binning time 2 μ s

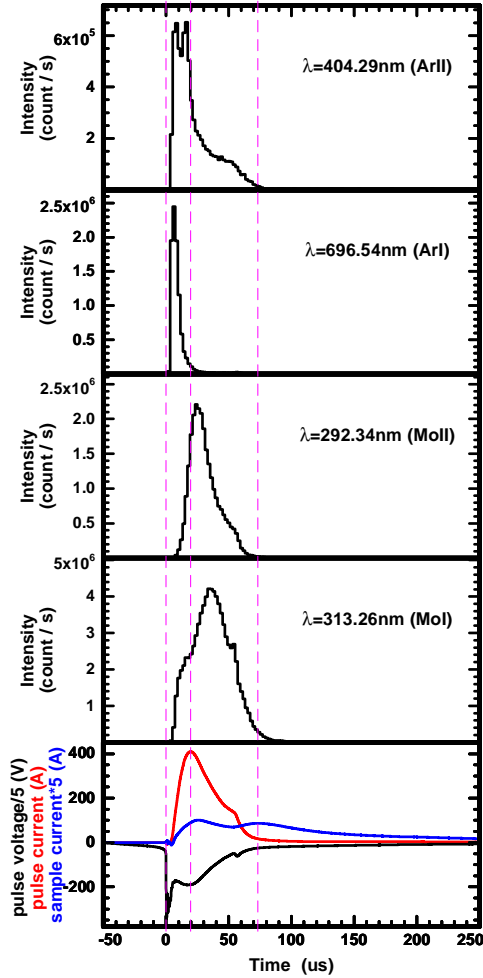


Figure VI-23. OES time resolved of Molybdenum HiPIMS discharge close to magnetron, sample-magnetron distance 21cm, binning time $2\mu\text{s}$

In Figure VI-18, Figure VI-19, Figure VI-20 are plotted, the OES time resolved spectra of all species present in the HiPIMS plasma discharge using Copper target.

In Figure VI-21, Figure VI-22, Figure VI-23, are reported the OES-TR spectra of Molybdenum HiPIMS discharge.

The pink lines indicate the most important events in the HiPIMS discharge, the start and the end of HiPIMS pulse, the maximum of target current and the maximum of current on sample holder.

The Figure VI-18 and Figure VI-21, show the light acquired positioning the optical fiber close to sample holder with a 11cm distance between magnetron and sample holder.

It is significantly because represents exactly the density and the time distribution of each specie present in the plasma, that reaches the sample. The study of this spectra can drive the setting of power supply in order to improve the deposition process.

The Figure VI-18 Figure VI-19 and Figure VI-22, the optical fiber is also positioned close to sample holder but in this case the distance between magnetron and sample holder is 21cm.

Finally in Figure VI-20 and Figure VI-23 show the plasma composition close to the magnetron.

In both target materials there are some similarity:

- 1) Considerable flux of ionized metal reaches the sample during the deposition.
- 2) In both case, it is present the time delay due to the ignition time of discharge
- 3) The delay is present in OES-TR spectra too, and underline the strong correlation between magnetron current and plasma ignition.
- 4) Higher presence of Argon close to the magnetron, instead close to the sample holder. This behavior could be explained introducing the gas rarefaction process and gas refilling as describe in 2.2.2.
- 5) The second peak of sample holder current pickup corresponds to an increment of ion species close to sample holder.

Chapter VII

Thin film characterization

7.1 Techniques

The analysis on produced coating is a fundamental part of experimental research.

In order to investigate the quality of thin films have been used basically three techniques:

- Atomic force microscope (AFM)
- Scanning (SEM) with different features (EDXS and FIB)
- Rutherford backscattering spectrometry

7.1.1 AFM analysis

The AFM measurements allow to measure and valuate the surface roughness of coating.

This device is usually used for thickness measurement (top coating - substrate) and for roughness measurement.

The coating asperities are recognized using a nano-tip mounted on a cantilever, that scanning the surface.

When the tip bumps into a peak or a valley, it follows the surface inducing a bending of cantilever (Figure VII-1).

Using a laser pointed onto cantilever and reflected on a photodiode matrix as detector, it is possible obtain the roughness information by the cantilever deflection.

Based on the whole surface mapping the device allows to calculate the quadratic and algebraic surface roughness.

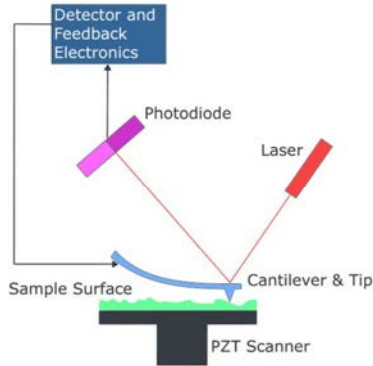


Figure VII-1. AFM layout

For roughness measurement it is recommended to use substrate with low roughness. Moreover if the sample is biased the substrate has to be a conductive material.

The technical details of used device are reported in cap 9.

For this experiment has been chose a Bayville chemical supply company Inc. silicon wafers as substrate. The silicon wafer has 100 orientation, chemical-mechanical polishing, roughness less than 1nm and 10 Ω cm resistivity.

7.1.2 SEM analysis

The Scanning Electron microscope is used for a first qualitative evaluation of surface roughness and thickness.

This device uses a focused electron beam to scan the surface and using a backscattered or secondary emitted electrons detector it creates the surface image.

The magnification that this device allows are in a range of some tens up to some hundreds of thousands (from 13x to 100kx).

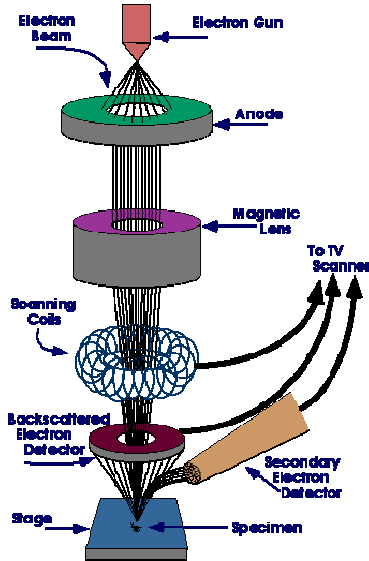


Figure VII-2. SEM layout

The electron source is usually produced by thermionic emission by a tungsten filament, in modern and more expensive SEM a Tungsten monocrystal is used. In this case the electron beam is generated by field emission (FEG field emission gun), the result is higher brilliance and higher resolution.

There are different features available for SEM, like EDXS analyzer and a second confocal ion source.

The EDXS is an energy dispersion X-ray spectrometer. This device allows the compositional analysis of sample.

The second confocal ion source (focused ion beam FIB) is a versatile device, that allows the erosion of sample surface, in order to investigate under the surface and it is used as ion cutter for micro-nano mechanics.

7.1.3 Rutherford backscattering spectrometry

RBS is one of most useful non-destructive technic for thin films study. It is a nuclear technique that uses ions as primary beam, generally Hydrogen or Helium.

Rutherford backscattering is applied to analyze the surface atomic composition, from uppermost layers to few micrometers inside of material.

The beam, with high-energy ions in the order of MeV, collides the sample surface. A part of them is backscattered, after a nuclear elastic interaction or electrons inelastic interaction with sample's atoms.

A silicon solid state detector pickup the backscattered ions, converts the ion energy in a current signal and sends that to the electronic chain acquisition line (NIM). As result is a RBS counts/energy spectrum.

The theory behind this technique is rather complex and it is not matter of this thesis.

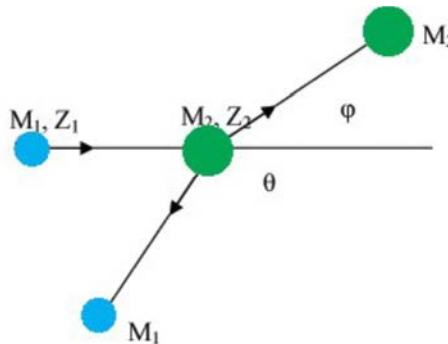


Figure VII-3. Exmple of nuclear interaction, M_1 is the projectile particle (primary ion beam), M_2 is the semple atom

Basically the backscattered ion energy is proportional to the ratio projectile mass and sample mass. In this way it is possible the discrimination of sample elements.

$$E_1 = k \cdot E_0 \quad \text{VII-1)}$$

$$k = \left(\frac{m_1 \cdot \cos \theta_1 \pm \sqrt{m_2^2 - m_1^2 \sin^2 \theta_1}}{m_1 + m_2} \right)^2 \quad \text{VII-2)}$$

Using RBS technique allow to obtain different information:

- Identification of surface chemical species by backscattered ions energy discrimination
- Quantitative analysis of sample composition
- Composition profile of target material
- Thickness or mass measurement expressed in dose (atoms/cm²)

7.2 Sample preparation and deposition parameters

In the early stage of experimental part have been testes several system configurations and power supply parameters.

The used materials Copper and Molybdenum have been chose due to their immiscible characteristic. In fact these materials don't create alloys and maintain the well-defined interfaces. This is essential for a dislocation barrier effect.

The first observed problem is a low adhesion of coating to commercial silicon wafer substrate. The de-adhesion has been shown for both of coating material used (Copper and Molybdenum).

The de-adhesion is caused by the incompatibility between the sputtered metal and the native silicon oxide.

In order to resolve this problem, the samples have been pretreated with hydrofluoric acid bath, deionized water washing and fast drying using carbon dioxide snow jet cleaner. The last part of sample surface cleaning is a plasma etching directly inside the deposition chamber.

Chemical pretreatment: <ul style="list-style-type: none"> ➤ HF 5% vol. solution ➤ 5 min ➤ Constant agitation ➤ Deionized water rising ➤ CO₂ drying 	Plasma pretreatment: <ul style="list-style-type: none"> Pressure: $7.5 \cdot 10^{-3}$ mbar Process gas Ar grade N6 Time: 30min Power supply: ENI <ul style="list-style-type: none"> ➤ Pulsed DC 0.15A current controlled ➤ Frequency: 180KHz ➤ Duty cycle: 496ns ➤ Applied to entire sample holder Power supply: Senvac Maris GS-05 <ul style="list-style-type: none"> ➤ DC 0.5A current controlled ➤ Applied to Titanium gettering source
--	--

Table VII-1. pretreatment parameters

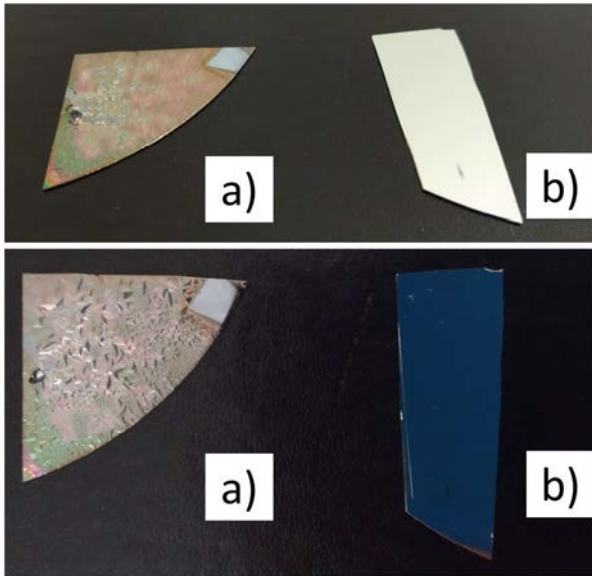


Figure VII-4. Sample pretreatment effect on Mo coating, a) without pretreatment and b) with pretreatment

Figure VII-4 reports the improvement of coating quality and adhesion, due to substrate pretreatment. The two pictures, top and bottom, show the same sample at different angles, in order to emphasize the de-adhesion of no pretreated sample (Figures VII-4 a) compared to sample with plasma pretreatment (Figures VII-4 b).

As described in cap 4.2.1 the sample holder is a mockup of final sample groove (Mandrel). In order to understand the thickness and quality of coating, silicon wafer substrates are positioned inside the mockup groove and external position.

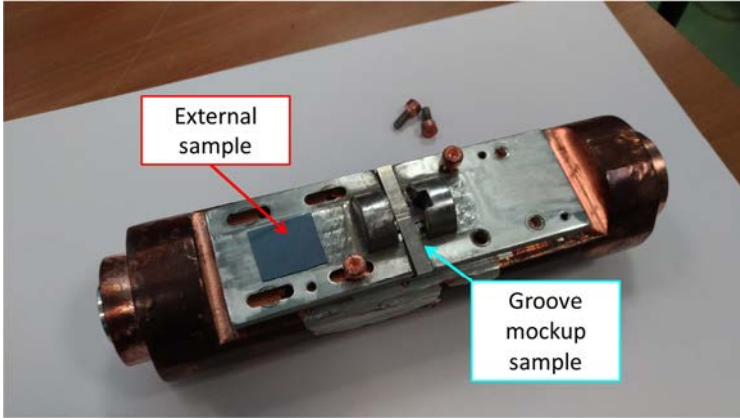


Figure VII-5. Sample holder assembly

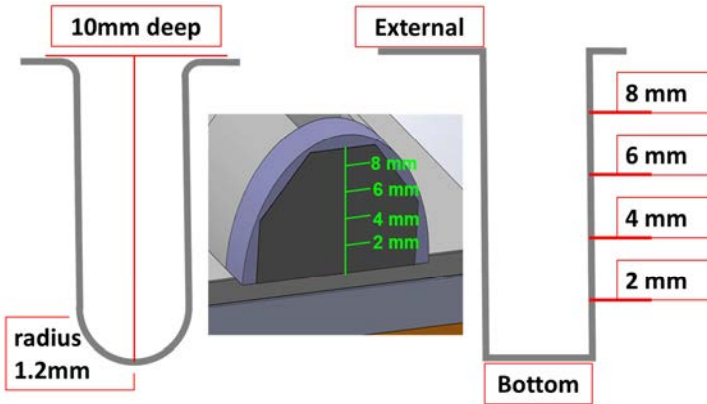


Figure VII-6. Real Groove profile and relative mockup with investigated points

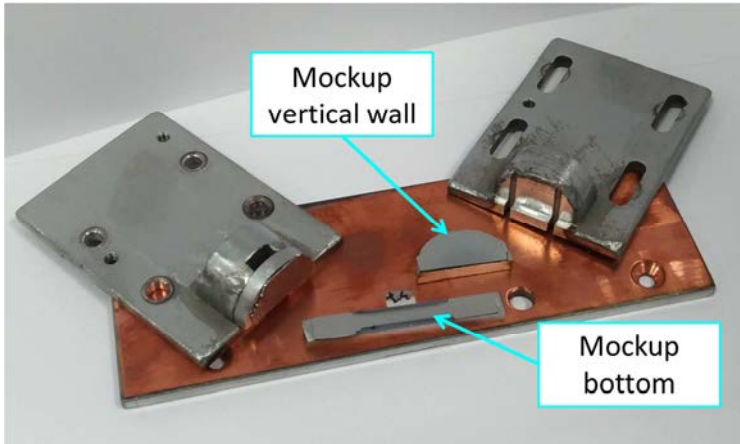


Figure VII-7. Mockup deassembled with sample

The final deposition parameters are based on several process factors:

- Coexistence of two sputtering source, the main for HiPIMS discharge and the secondary for titanium gettering
- Magnetron power dissipation (cooling system)
- Sample holder discharge.
- Encumbrance of the mechanical component integrated inside the chamber (optical fiber holder, magnetron shutter, rotating disc for gettering)
- Pumping capability
- Budget

The working pressure has been set at $4.5 \cdot 10^{-3}$ mbar using Argon N6 grade.

That is a compromise between thermalization of sputtered materials and titanium source ignition.

The thermalization is an effect of sputtered atoms multi-scattering with gas. When the sputtered material is thermalized lose its original trajectory, that is traduced in sputtering rate loss.

This effect is proportional with the gas pressure, then reduce this parameter is important to improve the sputtered material flux.

Opposite the titanium source, due to its magnetic field configuration works better at high pressure. Using pressure lower than $4.0 \cdot 10^{-3}$ mbar compromise the right discharge ignition, as result a very low current anomalous discharge, and an inefficient gettinger process.

About power supply parameters are reported in Table VII-2

Target material: Copper Power supply: Hüttinger 4001 Pulse width: 75 μ s Pulse Voltage: 750V Frequency: 48Hz Bias: -100V Distance: 11cm Sample holder rotation:	Target material: Molybdenum Power supply: Sinex 1.2 Set point: 160Vac Frequency: 50Hz Bias: -100V Distance: 11cm
--	---

Table VII-2. Copper and Molybdenum HiPIMS power supply parameters

The coupling Copper-Hüttinger and Molybdenum-Sinex is due to two reasons:

- 1) The Copper target doesn't sustain the Sinex ignition voltage without target surface discharge.
- 2) The Molybdenum sputtering yield is lower than Copper sputtering yield Figure VII-8

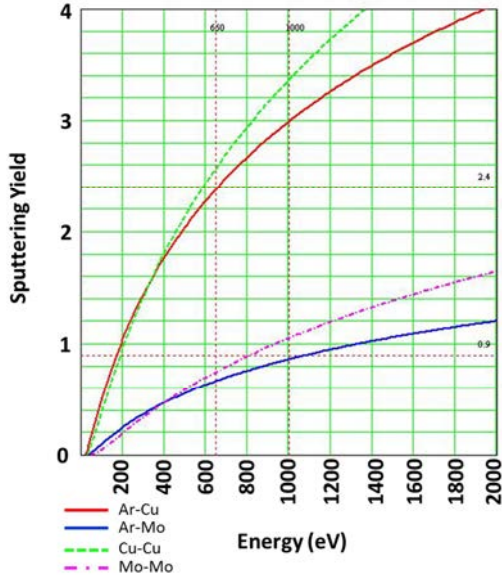


Figure VII-8. Copper and Molybdenum sputtering yield [136]

The power supply frequency is restricted by the RC circuit time recovery of bias box; anyway it is possible increase the Hüttinger pulse frequency up to 100Hz without relevant voltage bias loss.

Based on electrical and optical analysis the pulse parameters have been determinate. About the voltage concerning Hüttinger (750V) the limitation is due to the sample holder arc ratio in the early stage of deposition. The discharges on sample holder are caused by inhomogeneity of sample surface, like corners, tip and residual dielectric material.

The chosen voltage is enough high to obtain a HiPIMS discharge and in same time enough low to prevent sample arc Figure VII-9.

Using the final smooth mandrel as sample, it wills possible increase this parameter without arcs.

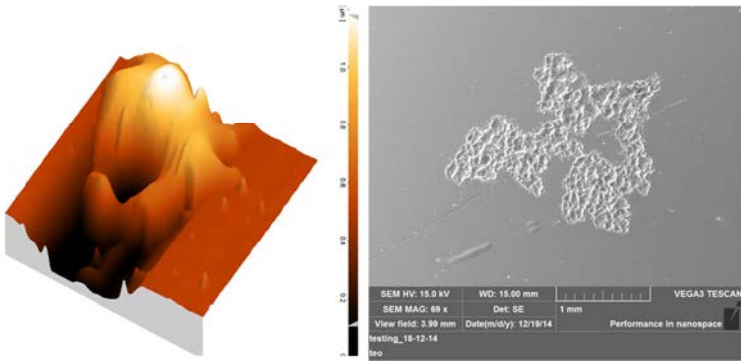


Figure VII-9. Example of Arc damage on Copper coating(Tescan)

The distance has been set in order to increase as possible the sputtering rate, maintaining enough space for the magnetron shutters and relative movement.

7.3 Single layer analysis results

The single layer coatings have been studied gradually for every different system change, in order to investigate the coating quality improvements.

The next results of AFM, SEM, and RBS measurements are referred to samples coated with deposition parameters mentioned in previous paragraph (Table VII-2).

The used substrate are silicon wafer, and the measured areas are referred to sample in external position Figure VII-6.

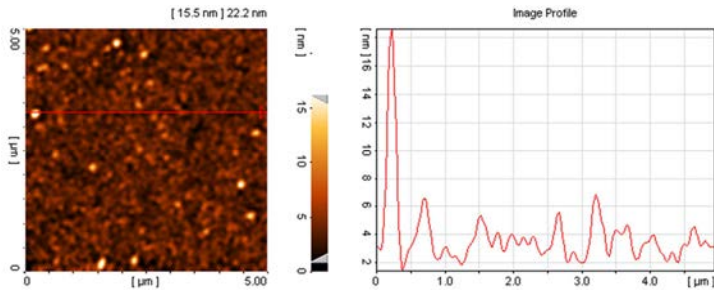


Figure VII-10. Example of Copper single layer coating morphology and profile

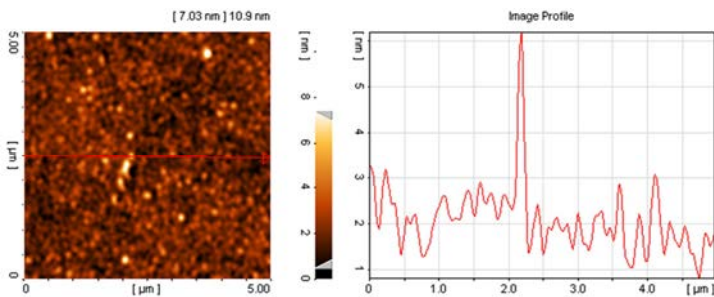


Figure VII-11. Example of Molybdenum single layer coating morphology and profile

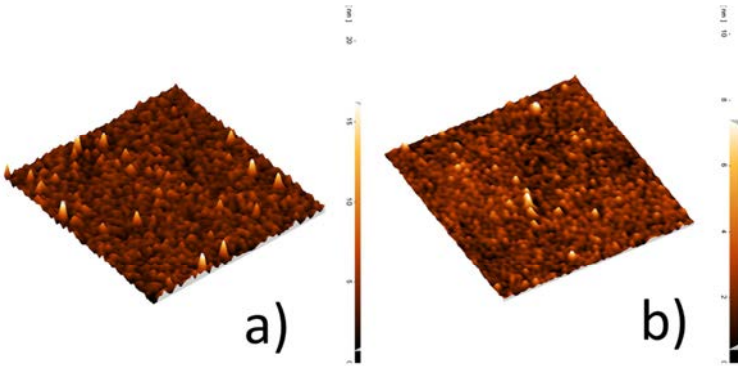


Figure VII-12. a)Copper and b)Molybdenum single layer coating morphology 3D images

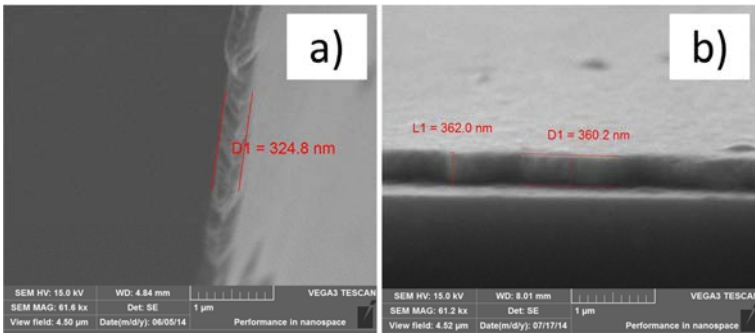


Figure VII-13. a)Copper and b)Molybdenum single layer coating cross section (Tescan)

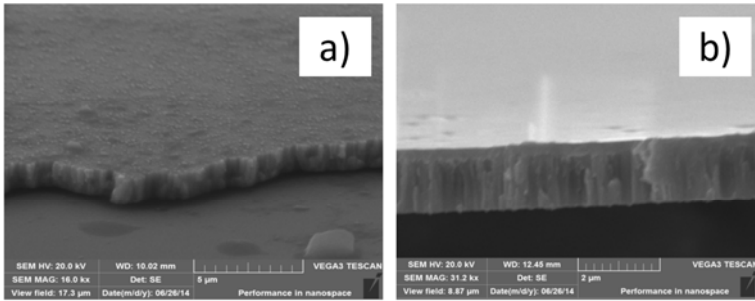


Figure VII-14. Example of Copper Molybdenum bi-layer coating cross section. a) external rough surface; b) smooth coating-substrate surface. 1.4 μm thick (Tescan)

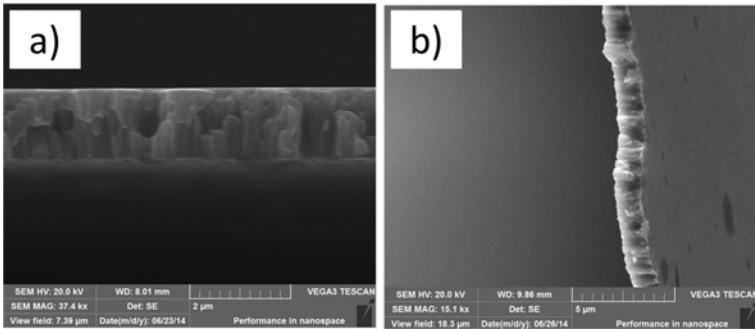


Figure VII-15. Example of Copper Molybdenum bi-layer coating cross section. 1.4 μm thick (Tescan)

Due to high materials ductility, especially for copper, AFM technique is not useful for thickness measurement.

It has been used RBS technique for deposition rate estimation.

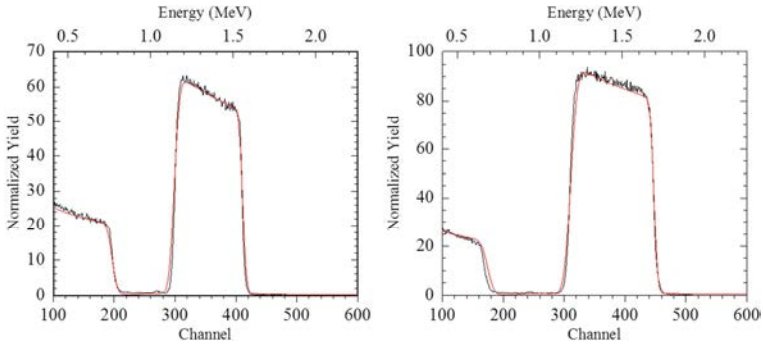


Figure VII-16.a)Copper and b)Molybdenum single layer coating RBS spectra

Material	Ra [nm]	Rq [nm]	Thickness [nm]	Deposition Rate [nm/s]
Cu/Si	2.5 ± 0.3	3.1 ± 0.3	324.8	0.586 ± 0.059
Mo/Si	2.7 ± 0.3	3.4 ± 0.3	360	0.175 ± 0.02

Table VII-3. Summary of single layer characteristics

The single layer deposition is an useful instrument in order to understand the setup improvements.

Using this kind of coating permits the analysis AFM and SEM as routine procedure. The RBS measurements conversely are more complex to organize, because the accelerator time schedule are planned every six months.

That means few days of accelerator shifts each year and the analyzed samples must to be more certain as possible, in order to use more as possible the available accelerator beam time.

7.4 Multilayer analysis results

As mentioned the goal of the project is a nanostructured multilayer coating deposited inside the mandrel grooves.

In order to investigate the quality of coating onto this particular object shape has been used the mandrel mockup described in previous paragraph.

In this paragraph will be reported the coating measurement and results in two chamber configurations:

- 1) 21cm magnetron-sample holder distance, contemporaneous deposition of the two metals (both HiPIMS power supplies active)
- 2) 11cm magnetron-sample holder distance, alternating deposition (HiPIMS power supplies alternate switched on)

The power supply parameters are the same for both configurations as reported in Table II-1.

The multilayer has been characterized by RBS techniques using AN200 Van der Graaff accelerator available at INFN-LNL laboratories.

The analysis are focused onto groove vertical wall, groove bottom and external point, in order to understand how the deposition rate changes as function of shadow effect induced by the groove.

The coating thickness and the resulting deposition rate calibration, is calculated using RBS technique due to their shape and materials complexity.

7.4.1 Multilayer in first configuration

In first configuration (21cm) the sample holder has been maintained in 0.3 rpm constant rotation, with both HiPIMS power supplies active. Furthermore the multilayer has been realized before the Titanium gettering subsystem setup.

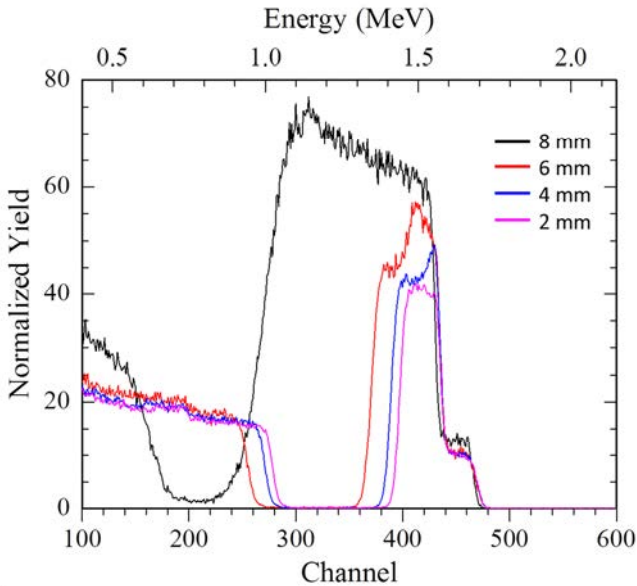


Figure VII-17. RBS spectra of coated vertical wall, measured in different point (referref to Figure VII-6)

In Figure VII-17 are reported the RBS spectra (2MeV He^{4+} ions) related to different points on groove vertical wall. It is possible to observe a strong rate deposition loss in deeper position due to the shadowing effect of groove.

Moreover due to the instrumental resolution, it is not possible discern the multilayer structure.

That means the thickness of each layer inside the groove may be too much thin to carry out the dislocation barrier role.

Established the hypothesis that the coating stoichiometry is the constant in each point of the groove wall, it has been calculated, using spectrum simulation and area integral, the stoichiometry in amount of 9.5 to 1 Copper atoms related to Molybdenum atoms.

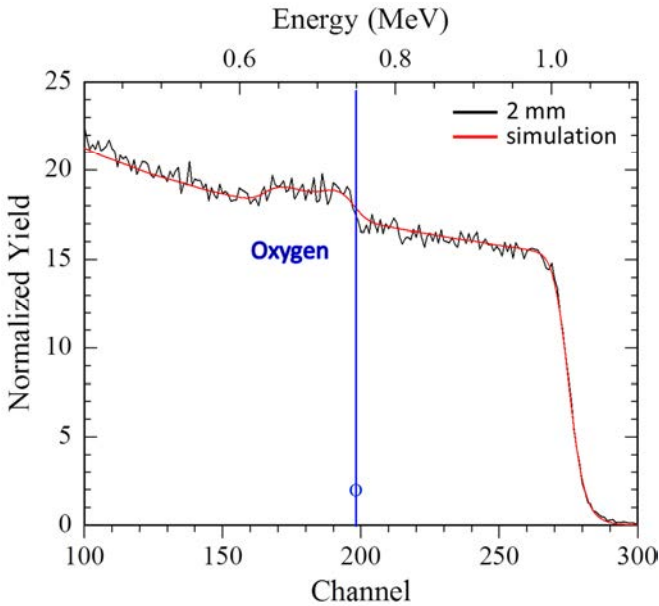


Figure VII-18. Oxygen contamination in coating 2mm position

Another problem of this coating is the presence of oxygen contamination (see Figure VII-18 as detail of 2mm spectrum). Moreover the ratio of oxygen increase going inside the groove, this effect is due to a lower rate deposition.

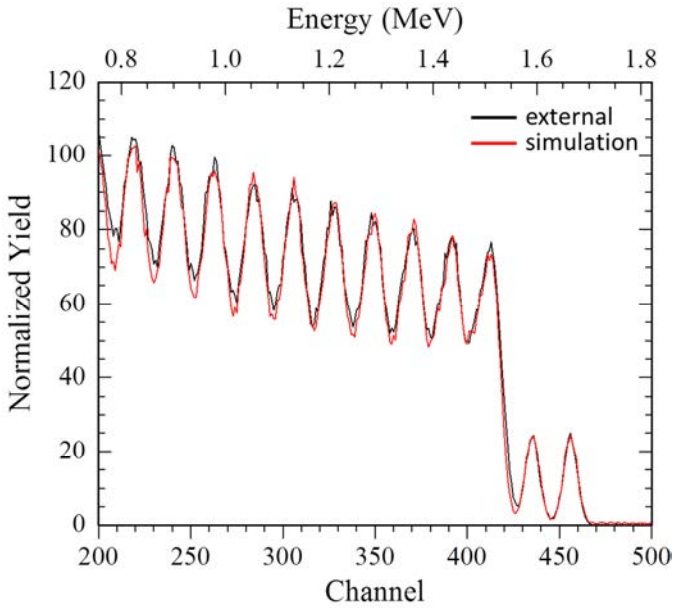


Figure VII-19. nanostructured multilayer in external position

Considering the hypothesis and experimental parameters:

- 1) 0.3 rpm
- 2) 1.5 hours of deposition time (27 bilayer)
- 3) -50V bias voltage
- 4) Power supply parameters Table VII-2
- 5) Constant stoichiometry (negligible differential re-sputtering effect)
9.5 Copper atoms to 1 Molybdenum atoms
- 6) Raw material density

It is possible calculate in first approximation the thickness of each layer.

	Dose layer [(atoms/cm ²)*10 ¹⁵]	Thickness layer [nm]	Total thickness bilayer [nm]
Cu 2mm	27.09 ± 0.81	3.21 ± 0.10	98.55 ± 2.95
Mo 2mm	2.85 ± 0.09	0.44 ± 0.01	98.55 ± 2.95
Cu 4mm	29.91 ± 0.90	3.54 ± 0.11	108.81 ± 3.26
Mo 4mm	3.15 ± 0.09	0.49 ± 0.01	108.81 ± 3.26
Cu 6mm	37.65 ± 2.64	4.46 ± 0.31	136.89 ± 9.58
Mo 6mm	3.96 ± 0.28	0.61 ± 0.04	136.89 ± 9.58
Cu 8mm	108.37 ± 9.75	12.84 ± 1.16	394.47 ± 35.50
Mo 8mm	11.41 ± 1.03	1.77 ± 0.16	394.47 ± 35.50
Cu external	477.20 ± 14.3	74.1 ± 2.22	2211.3 ± 66.34
Mo external	49.90 ± 1.49	7.8 ± 0.23	2211.3 ± 66.34

Table VII-4. Interest points coating layer thickness

The layer thickness and related error reported in Table VII-4 are calculated using the total thickness of coating. After simulation has been divided the amount in mass for each materials by the number of sample holder rotations (27 bilayer).

The error has been calculated as ratio of experimental data and simulation for each spectrum.

The values reported are only an estimation.

The configuration 21cm sample holder – magnetron distance has been discarded for the following reasons:

- 1) multilayer coating is not well defined in all the groove surface. The multilayer barrier effect for dislocation is not guarantee.
- 2) The high oxygen contamination (higher than 20% of mass in 2mm groove position) is not admissible for the application, because oxide inclusions may induce discharge.
- 3) High difference of rate deposition comparing different points inside groove and external position.
- 4) Deposition rate too much low (less than 0.1nm/s in worst position)

7.4.2 Multilayer in second configuration

For the previous reasons has been decided some modifications of sputtering chamber:

- 1) Active Titanium gettering subsystem on order to decrease the Oxygen contamination.
- 2) A strong reduction of magnetron-sample distance in order to increase the deposition rate.

The deposition parameter in this configuration include:

- 11cm magnetron-substrate distance
- HiPIMS power supply parameters Table VII-2
- Alternate deposition, power supply switched on one after the other
- Sample holder rotation 3rpm, in order to reduce thickness error due to the final position for each layer cycle
- Target contamination protection using a shutter, when the other source operate

- Two different sample holder bias voltage, in order to investigate the bombardment effect on the coating characteristics (-50V and -100V).
- The thickness evaluation of each layer has been calculated using the average of material total amount for copper. About Molybdenum has been chose to use the two external layers, in order to reduce the substrate interaction (cap. 7.4.4).

The multilayers have been characterized using the μ -beam line of AN2000 at LNL-INFN laboratories, in order to reduce the lateral error due to the thickness variation along the groove vertical wall.

As mentioned before, for this analysis have been realized two multilayer using the same experimental parameter ad exception of voltage bias.

The multilayer has been designed Figure VII-21 before the coating phase in order to improve the RBS results, and obtain as possible the peaks separation.

The coating is composed by five layers onto pretreated silicon substrate:

- 1) Mo, deposition time 7'36''
- 2) Cu, deposition time 12'0''
- 3) Mo, deposition time 7'36''
- 4) Cu, deposition time 12'0''
- 5) Mo, deposition time 7'36''
- 6) Si

The rate deposition results in external position is:

- Cu: $0.586 \pm 10\%$ nm /s
- Mo: $0.175 \pm 10\%$ nm /s

The proof of effectiveness of gettering subsystem is reported in Figure VII-20.

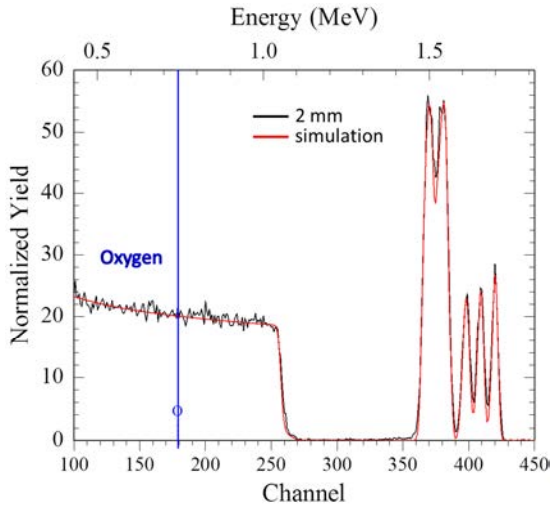


Figure VII-20. RBS spectra after Titanium gettering subsystem installation

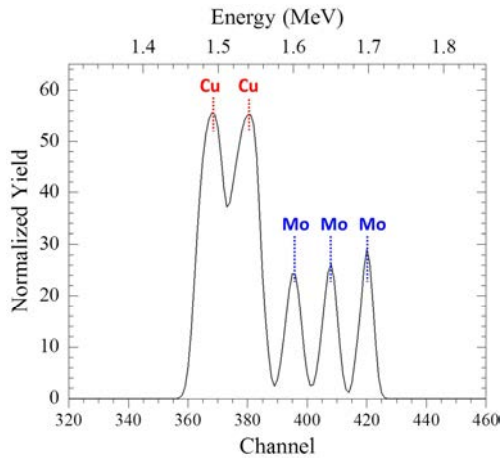


Figure VII-21. Example penta-layer design

7.4.2.1 Multilayer in second condition and low sample holder bias (-50V) results

As usual has been checked and measured the sample morphology and roughness respectively using AFM.

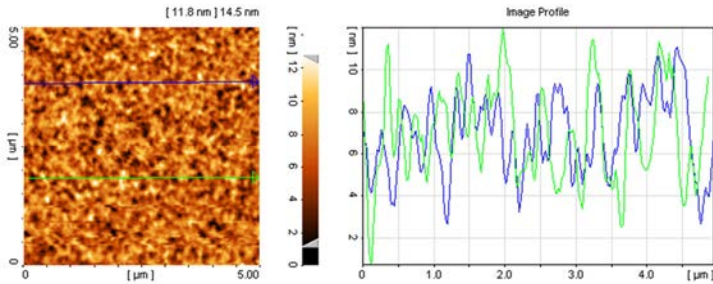


Figure VII-22. AFM profile measurement of coating with low sample holder bias

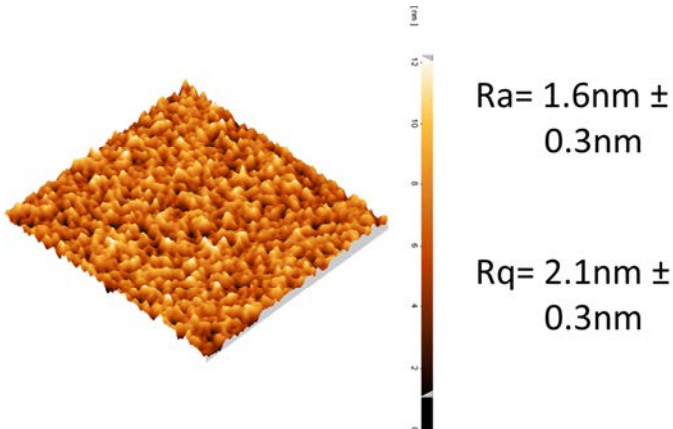


Figure VII-23. AFM morphology of coating with low sample holder bias

The follow images have been realized using an high resolution field emission gun SEM at INRIM laboratory (Turin). This device is equipped of Gallium ion source that permits to work the sample, as example etch and cut. Moreover it is available a STEM detector that permits to obtain images of multilayer cross section.

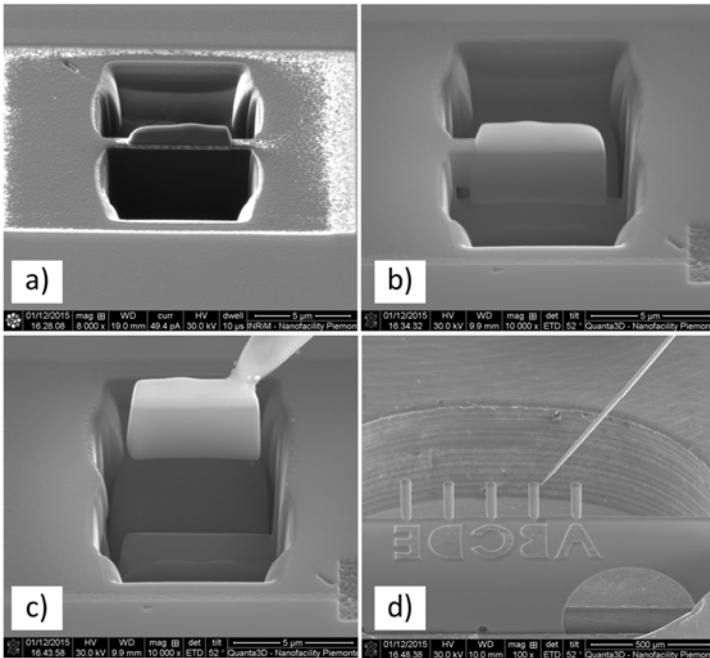


Figure VII-24. STEM sample preparation, a) and b) sample erosion with Ga-ion beam; c) and d) plate handling

The measurement is focused on groove vertical walls, in order to evaluate the quality of coating.

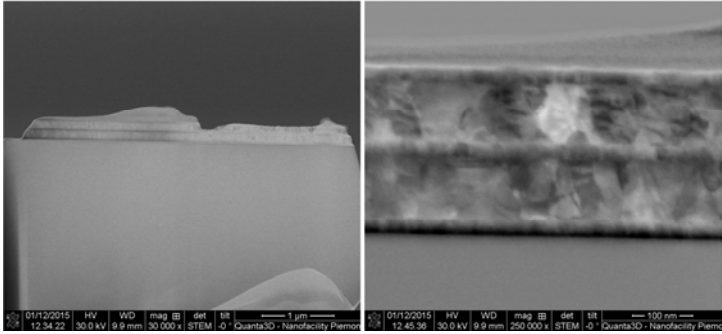


Figure VII-25. Cross section STEM image of low bias multilayer sample

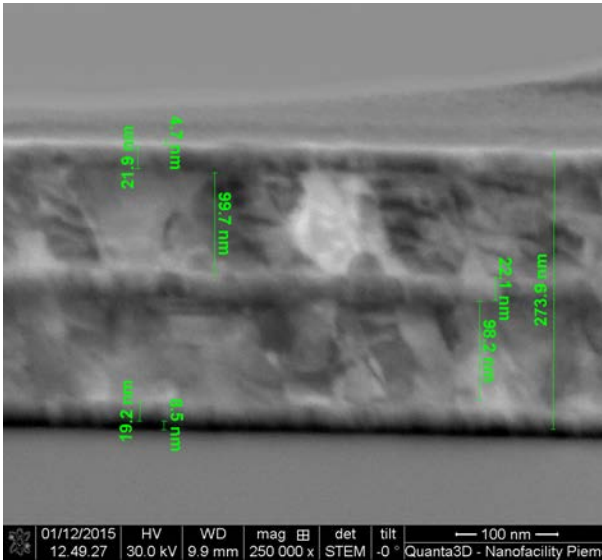


Figure VII-26. Cross section STEM image of low bias multilayer sample

In Figure VII-26 is reported the cross section and relative thickness measurements of multilayer. The plate has been obtained at 7 mm far from groove bottom on vertical wall.

It is possible to discern clearly the penta-layer structure.

Furthermore each layer exhibits a complete crystallization, the grains grow mainly in perpendicular direction of substrate, typical characteristic of HiPIMS coatings [116][137].

As mentioned at the beginning of paragraph, for RBS analysis it has been used the μ -beam tools of AN2000 accelerator (LNL-INFN), in order to reduce the lateral error due to the thickness variation inside the beam spot (close to 1 mm²).

Will be reported the multilayer spectra concerned the 2mm, 4mm, 6mm, 8mm on groove vertical wall, groove bottom and on external position (Figure VII-6).

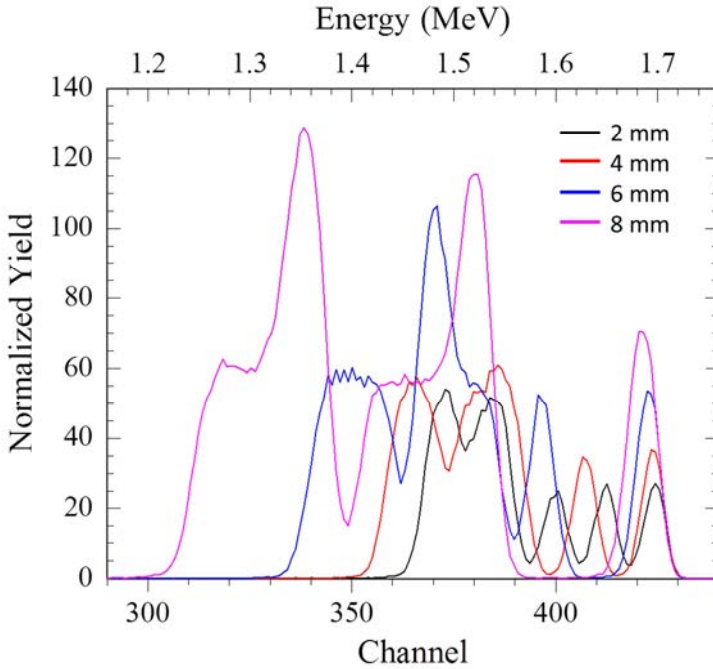


Figure VII-27. RBS spectra of - 50V biased sample groove wall

Otherwise to first configuration coating in this case the multilayer structure is well define.

It is also visible that going inside the groove, the coating thickness has a strong decrease due to the vertical wall shadowing.

The thickness of Copper and Molybdenum layer are reported in Table VII-6.

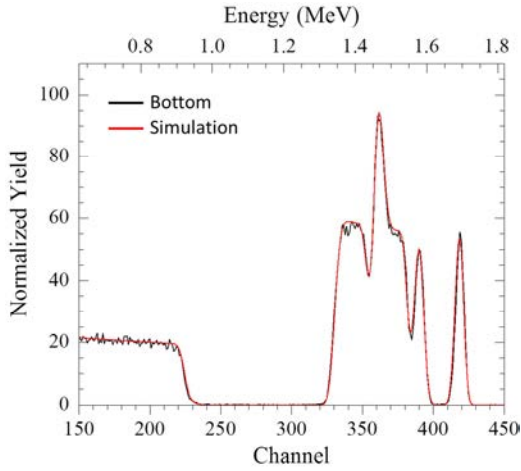


Figure VII-28.RBS spectra of - 50V biased groove bottom

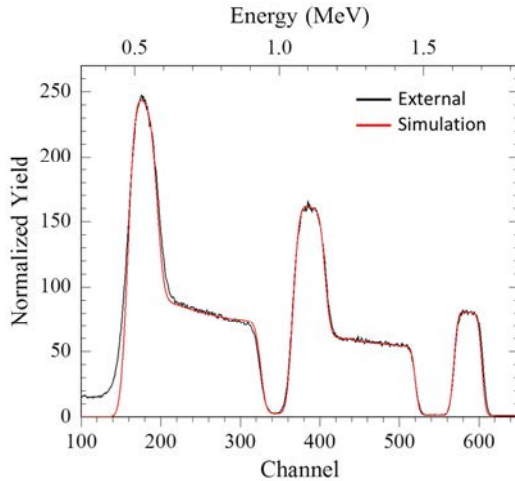


Figure VII-29.RBS spectra of - 50V biased of expenal posion

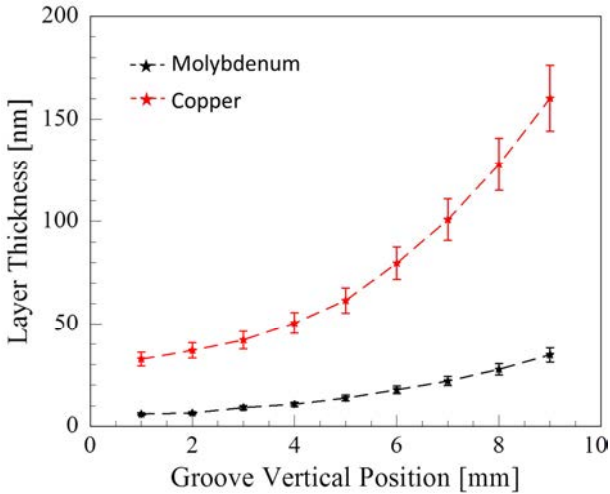


Figure VII-30. Layer thickness profile on groove vertical wall (-50V)

Position [μm]	Cu Thickness [atoms/cm ²]	Mo Thickness [atoms/cm ²]
1000	$5.55\text{E}+17 \pm 5.55\text{E}+16$	$1.15\text{E}+17 \pm 1.15\text{E}+16$
2000	$6.27\text{E}+17 \pm 6.27\text{E}+16$	$1.25\text{E}+17 \pm 1.25\text{E}+16$
3000	$7.13\text{E}+17 \pm 7.13\text{E}+16$	$1.75\text{E}+17 \pm 1.75\text{E}+16$
4000	$8.56\text{E}+17 \pm 8.56\text{E}+16$	$2.07\text{E}+17 \pm 2.07\text{E}+16$
5000	$1.04\text{E}+18 \pm 1.04\text{E}+17$	$2.64\text{E}+17 \pm 2.64\text{E}+16$
6000	$1.35\text{E}+18 \pm 1.35\text{E}+17$	$3.42\text{E}+17 \pm 3.42\text{E}+16$
7000	$1.71\text{E}+18 \pm 1.71\text{E}+17$	$4.23\text{E}+17 \pm 4.23\text{E}+16$
8000	$2.17\text{E}+18 \pm 2.17\text{E}+17$	$5.33\text{E}+17 \pm 5.33\text{E}+16$
9000	$2.72\text{E}+18 \pm 2.72\text{E}+17$	$6.69\text{E}+17 \pm 6.69\text{E}+16$

Table VII-5. Copper and Molybdenum layer thickness [atoms/cm²] groove vertical wall position (-50V)

In Table VII-5 are reported the layers thickness declared in Dose [atoms/cm²], that is the standard unit for RBS measurement.

In order to make easier the comprehension of the real dimension of layer the Dose has been converted in nanometer [nm] using the nominal density of standard materials.

This is possible if the coating is considered fully dense as hypothesis. Generally the sputtered materials are few percent lighter than the raw materials, but the amount of voids using HiPIMS technique is lower than standard sputtering techniques.

Position [μm]	Cu Thickness [nm]	Mo Thickness [nm]
1000	32.7 ± 3.27	5.99 ± 0.60
2000	37.0 ± 3.70	6.52 ± 0.65
3000	42.0 ± 4.20	9.10 ± 0.91
4000	50.4 ± 5.04	10.77 ± 1.08
5000	61.6 ± 6.16	13.73 ± 1.37
6000	79.7 ± 7.97	17.78 ± 1.78
7000	100.8 ± 10.08	21.99 ± 2.20
8000	127.8 ± 12.79	27.71 ± 2.77
9000	160.1 ± 16.02	34.78 ± 3.48

Table VII-6. Copper and Molybdenum layer thickness [nm] groove vertical wall position (-50V)

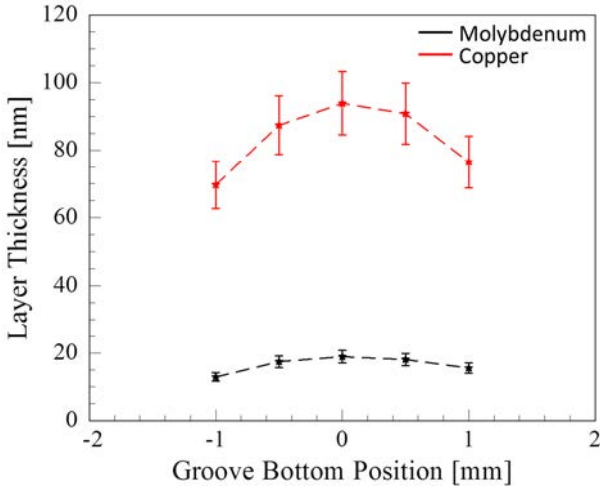


Figure VII-31. Layer thickness profile onto the groove bottom (-50V)

Position [μm]	Cu Thickness [atoms/cm^2]	Mo Thickness [atoms/cm^2]
-1000	$1.18\text{E}+18 \pm 1.18\text{E}+17$	$2.47\text{E}+17 \pm 2.47\text{E}+16$
-500	$1.48\text{E}+18 \pm 1.48\text{E}+17$	$3.35\text{E}+17 \pm 3.35\text{E}+16$
0	$1.60\text{E}+18 \pm 1.60\text{E}+17$	$3.63\text{E}+17 \pm 3.63\text{E}+16$
500	$1.54\text{E}+18 \pm 1.54\text{E}+17$	$3.47\text{E}+17 \pm 3.47\text{E}+16$
1000	$1.30\text{E}+18 \pm 1.30\text{E}+17$	$2.98\text{E}+17 \pm 2.98\text{E}+16$

Table VII-7. Copper and Molybdenum layer thickness [atoms/cm^2] onto groove bottom (-50V)

Position [μm]	Cu Thickness [nm]	Mo Thickness [nm]
-2000	69.72 ± 6.97	12.86 ± 1.29
-1000	87.42 ± 8.74	17.45 ± 1.75
Center	94.04 ± 9.40	18.90 ± 1.89
1000	90.70 ± 9.07	18.06 ± 1.81
2000	76.46 ± 7.65	15.51 ± 1.55

Table VII-8. Copper and Molybdenum layer thickness [nm] onto groove bottom

7.4.3 Multilayer in second configuration and high bias (-100V)

Like in previous paragraph, it will be reported Morphology, cross section images and composition spectra about the multilayer deposited using -100V sample holder bias.

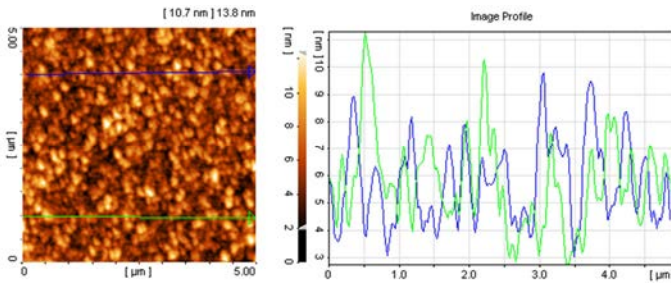


Figure VII-32. AFM profile measurement of coating with high sample holder bias

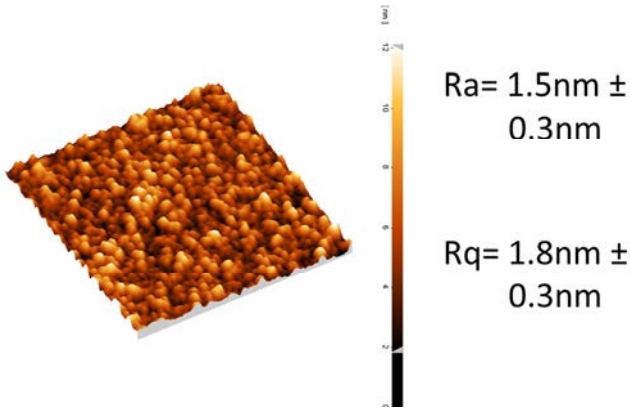


Figure VII-33. AFM morphology of coating with high sample holder bias

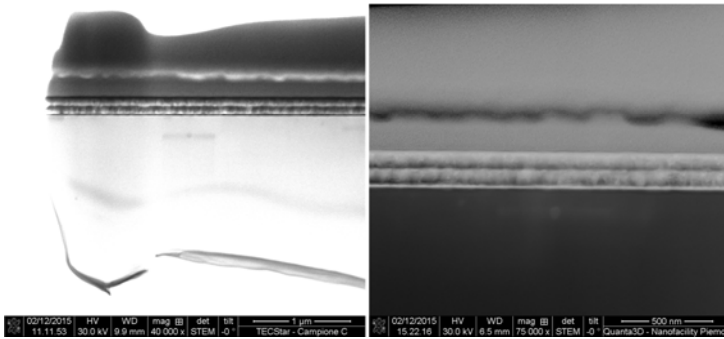


Figure VII-34. Cross section STEM image of high bias multilayer sample

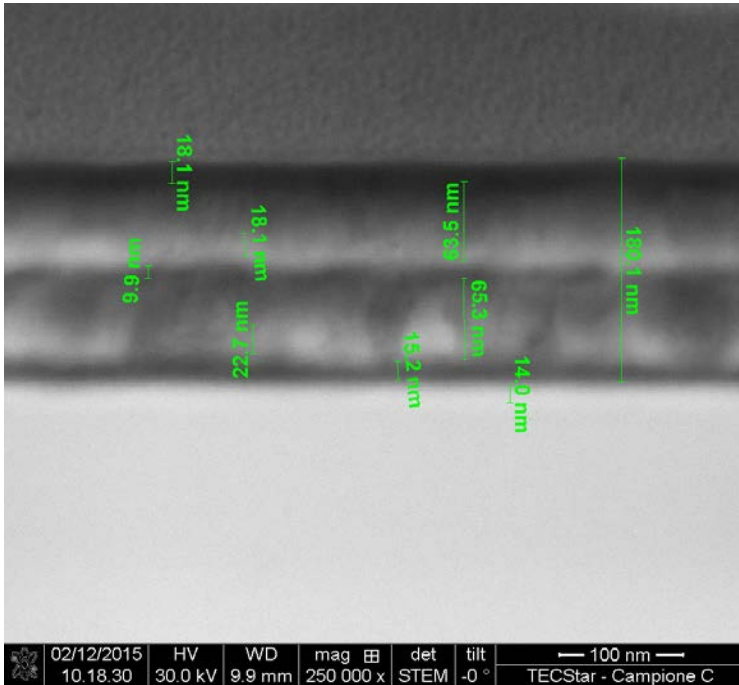


Figure VII-35. Cross section STEM image of high bias multilayer sample

Unfortunately in this case the image quality is lower than in other sample, that doesn't depend by the coating, but it is caused by the complicate preparation of STEM sample. Few hundreds nanometer thickness discriminate the quality of image.

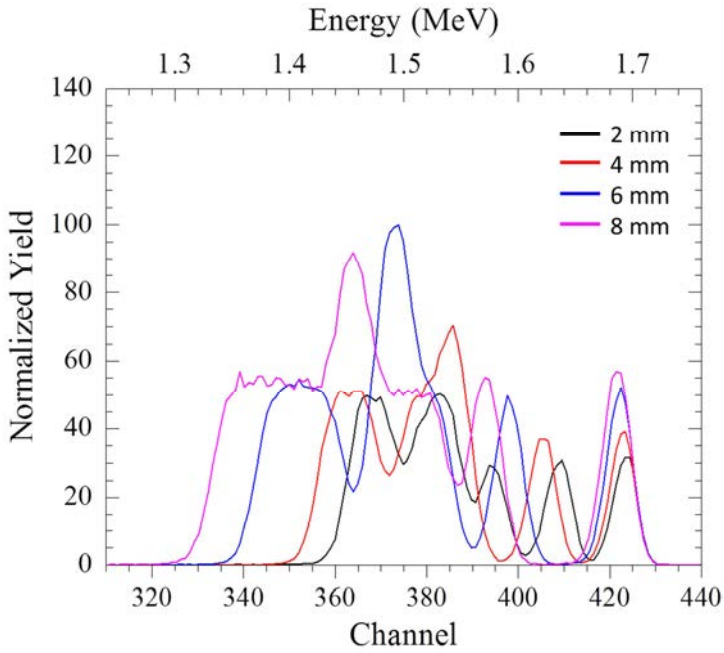


Figure VII-36.RBS spectra of - 100V biased sample groove wall

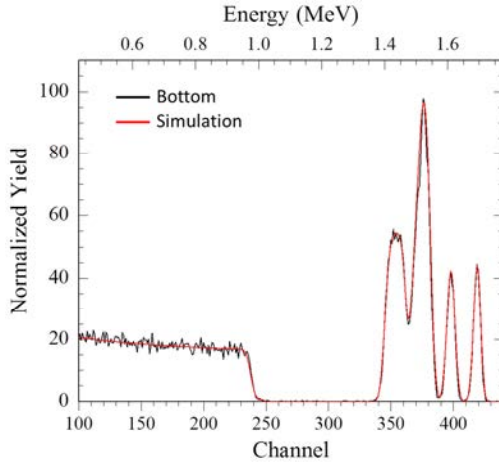


Figure VII-37. RBS spectra of - 100V biased groove bottom

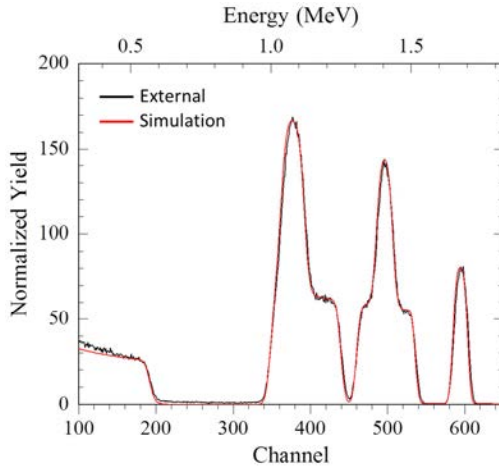


Figure VII-38. RBS spectra of - 100V biased of external position

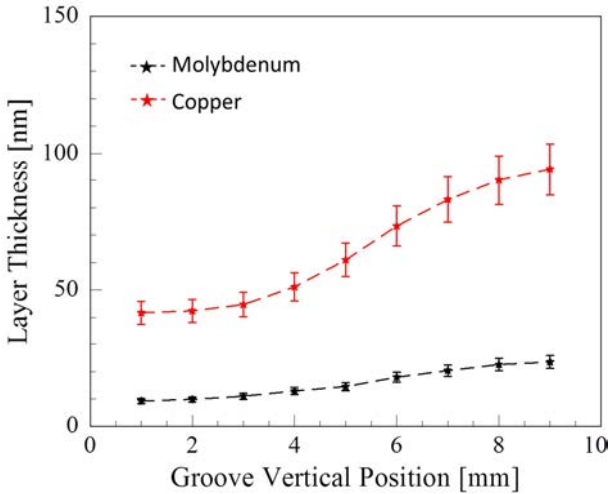


Figure VII-39. Layer thickness profile on groove vertical wall (-100V)

Position [μm]	Cu Thickness [atoms/cm^2]	Mo Thickness [atoms/cm^2]
1000	$7.10\text{E}+17 \pm 7.10\text{E}+16$	$1.09\text{E}+17 \pm 1.09\text{E}+16$
2000	$7.22\text{E}+17 \pm 7.22\text{E}+16$	$1.15\text{E}+17 \pm 1.15\text{E}+16$
3000	$7.61\text{E}+17 \pm 7.61\text{E}+16$	$1.29\text{E}+17 \pm 1.29\text{E}+16$
4000	$8.71\text{E}+17 \pm 8.71\text{E}+16$	$1.51\text{E}+17 \pm 1.51\text{E}+16$
5000	$1.03\text{E}+18 \pm 1.04\text{E}+17$	$1.70\text{E}+17 \pm 1.70\text{E}+16$
6000	$1.25\text{E}+18 \pm 1.25\text{E}+17$	$2.10\text{E}+17 \pm 2.10\text{E}+16$
7000	$1.41\text{E}+18 \pm 1.41\text{E}+17$	$2.38\text{E}+17 \pm 2.38\text{E}+16$
8000	$1.53\text{E}+18 \pm 1.53\text{E}+17$	$2.64\text{E}+17 \pm 2.64\text{E}+16$
9000	$1.60\text{E}+18 \pm 1.60\text{E}+17$	$2.75\text{E}+17 \pm 2.75\text{E}+16$

Table VII-9. Copper and Molybdenum layer thickness [atoms/cm^2] groove vertical wall position (-100V)

Position [μm]	Cu Thickness [nm]	Mo Thickness [nm]
1000	41.69 ± 4.17	9.28 ± 0.93
2000	42.39 ± 4.24	9.81 ± 0.98
3000	44.70 ± 4.47	10.97 ± 1.10
4000	51.14 ± 5.11	12.89 ± 1.29
5000	60.94 ± 6.09	14.48 ± 1.45
6000	73.27 ± 7.33	17.91 ± 1.79
7000	82.93 ± 8.29	20.29 ± 2.03
8000	90.10 ± 9.01	22.51 ± 2.25
9000	94.00 ± 9.40	23.45 ± 2.35

Table VII-10. Copper and Molybdenum layer thickness [nm] groove vertical wall position (-100V)

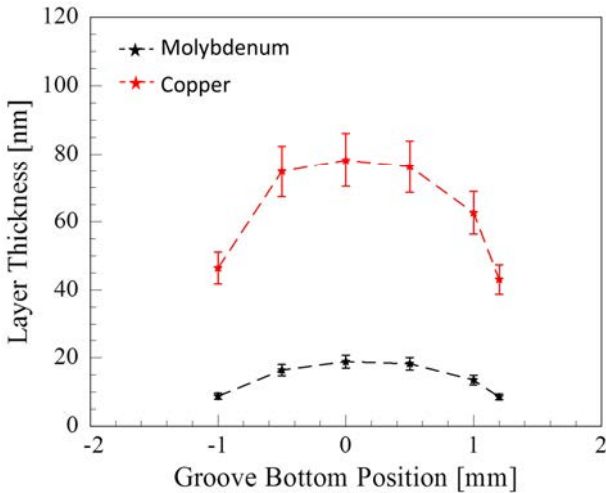


Figure VII-40. Layer thickness profile onto the groove bottom (-100V)

Position [μm]	Cu Thickness [atoms/cm²]	Mo Thickness [atoms/cm²]
-1000	$7.88\text{E}+17 \pm 7.88\text{E}+16$	$1.12\text{E}+17 \pm 1.12\text{E}+16$
-500	$1.27\text{E}+18 \pm 1.27\text{E}+17$	$2.09\text{E}+17 \pm 2.09\text{E}+16$
0	$1.33\text{E}+18 \pm 1.33\text{E}+17$	$2.41\text{E}+17 \pm 2.41\text{E}+16$
500	$1.29\text{E}+18 \pm 1.29\text{E}+17$	$2.33\text{E}+17 \pm 2.33\text{E}+16$
1000	$1.06\text{E}+18 \pm 1.06\text{E}+17$	$1.72\text{E}+17 \pm 1.72\text{E}+16$
1200	$7.32\text{E}+17 \pm 7.32\text{E}+16$	$1.09\text{E}+17 \pm 1.09\text{E}+16$

Table VII-11. Copper and Molybdenum layer thickness [atoms/cm²] onto groove bottom (-100V)

Position [μm]	Cu Thickness [nm]	Mo Thickness [nm]
-1000	46.45 ± 4.64	8.75 ± 0.88
-500	74.87 ± 7.49	16.34 ± 1.63
0	78.27 ± 7.83	18.84 ± 1.88
500	76.30 ± 7.63	18.20 ± 1.82
1000	62.65 ± 6.27	13.46 ± 1.35
1000	43.13 ± 4.31	8.52 ± 0.85

Table VII-12. Copper and Molybdenum layer thickness [nm] onto groove bottom (-100V)

7.4.4 Bias effect on coating, low and high voltage bias multilayer comparison

Later to the individual analysis of the samples deposited using different bias voltage, it has been started to study the bias effect on the deposition rate.

In this paragraph will be reported essentially the comparison of RBS analysis results already introduced previously.

The first investigated point is the external point, where the material flux and ion flux is maximum.

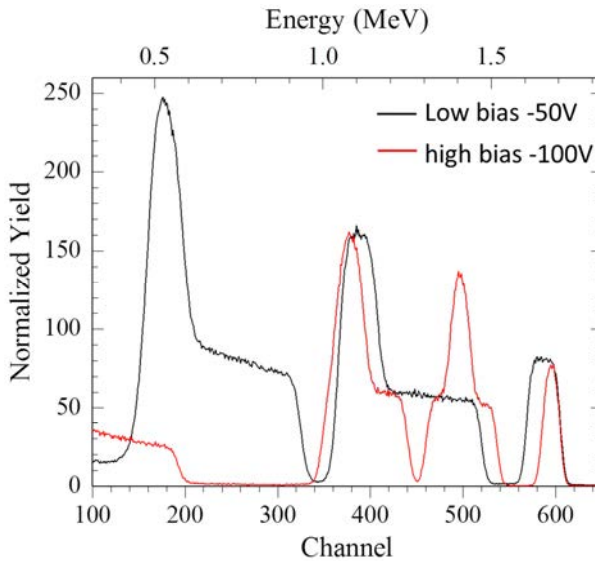


Figure VII-41. External point RBS spectra

n° layer	Material	low bias -50V [nm]	high bias -100V [nm]
5	Mo	82 ± 8.2	42 ± 4.2
4	Cu	375 ± 37.5	189 ± 18.9
3	Mo	84 ± 8.4	47 ± 4.7
2	Cu	390 ± 39.0	216 ± 21.6
1	Mo	90 ± 9.0	55 ± 5.5
Substrate	Si	-----	-----

Table VII-13. Layer thickness of external point

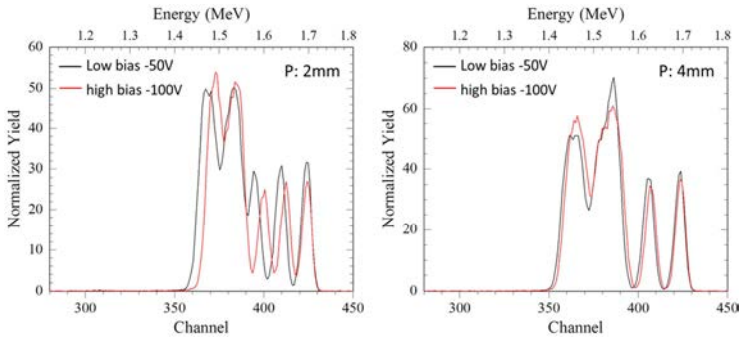


Figure VII-42. RBS spectra of 2mm and 4mm on groove wall

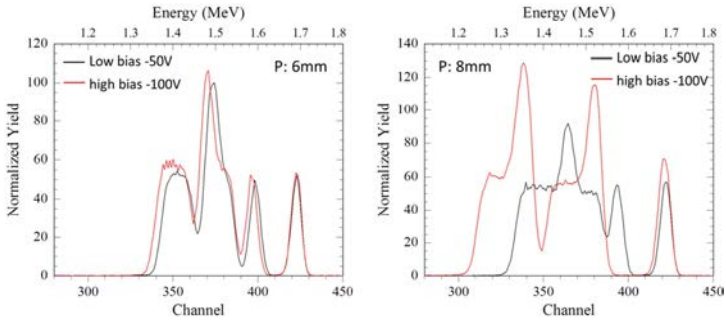


Figure VII-43. RBS spectra of 6mm and 8mm on groove wall

n° layer	Material	P: 2mm [nm]	P: 4mm [nm]	P: 6mm [nm]	P: 8mm [nm]
5	Mo	6.4 ± 0.6	10.1 ± 1.0	16.3 ± 1.6	24.7 ± 2.5
4	Cu	47.9 ± 4.8	64.5 ± 6.5	99.7 ± 10.0	154.5 ± 15.5
3	Mo	6.4 ± 0.6	9.9 ± 1.0	16.1 ± 1.6	24.4 ± 2.4
2	Cu	47.9 ± 4.8	64.5 ± 6.5	99.6 ± 10.0	154.5 ± 15.5
1	Mo	6.4 ± 0.6	9.9 ± 1.0	16.1 ± 1.6	24.4 ± 2.4
Substrate	Si	-----	-----	-----	-----

Table VII-14. Multilayer Low Bias (-50V) groove wall layer thickness

n° layer	Material	P: 2mm [nm]	P: 4mm [nm]	P: 6mm [nm]	P: 8mm [nm]
5	Mo	7.3 ± 0.7	12.2 ± 1.2	13.42 ± 1.3	14.48 ± 1.4
4	Cu	41.4 ± 4.1	70.6 ± 7.0	77.6 ± 7.7	83.44 ± 8.3
3	Mo	7.4 ± 0.7	12.0 ± 1.2	14.00 ± 1.4	15.95 ± 1.6
2	Cu	41.4 ± 4.1	70.6 ± 7.1	79.9 ± 8.0	90.2 ± 9.0
1	Mo	7.4 ± 0.7	12.0 ± 1.2	16.1 ± 1.6	18.6 ± 1.8
Substrate	Si	-----	-----	-----	-----

Table VII-15. Multilayer high Bias (-100V) groove wall layer thickness

In previous tables and figures is clear that the bias has a strong effect on layer thickness. More in detail has been observed an intense thickness reduction on external sample, instead inside the groove wall, the thickness variation induces an increment of thickness homogeneity Figure VII-44 and Figure VII-45.

This behavior may be explained introducing the re-sputtering effect [138]. Indeed with the increment of bias voltage the ions energy is incremented too. The strong bombardment induces a consequential material emission from the sample surface, finally the re-sputtered emitted materials may be lost, ad example in external sample and close to groove aperture, or it may be re-deposits in another point inside the groove.

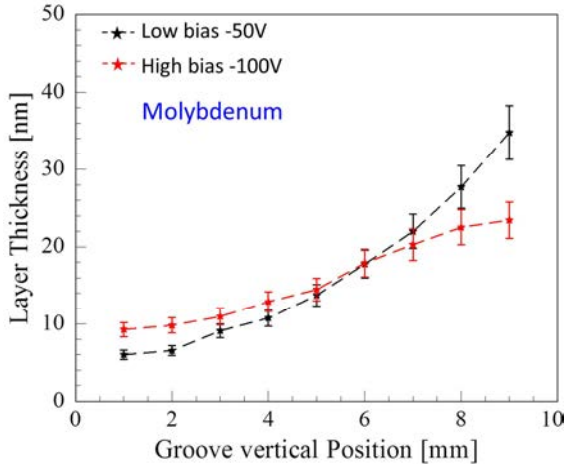


Figure VII-44. Molybdenum layers vertical wall thickness

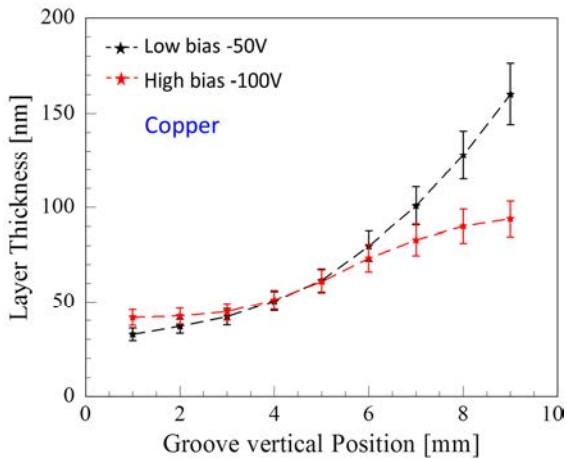


Figure VII-45. Copper layers vertical wall thickness profile

A similar effect has been observed on groove bottom.

n° layer	Material	P: -1mm [nm]	Center [nm]	P: +1mm [nm]
5	Mo	12.4±1.2	17.9±1.8	14.8±1.5
4	Cu	87.8±8.8	116.2±11.6	95.6±9.6
3	Mo	12.2±1.2	17.6±1.7	14.6±1.4
2	Cu	88.7±8.9	117.4±11.7	96.6±9.6
1	Mo	12.2±1.2	17.6±1.8	14.6±1.5
Substrate	Si	-----	-----	-----

Table VII-16. Multilayer Low Bias (-50V) groove bottom layer thickness

n° layer	Material	P: -1mm [nm]	Center [nm]	P: +1mm [nm]
5	Mo	6.6±0.7	13.7±1.4	9.7±1.0
4	Cu	44.9±4.5	74.1±7.4	59.5±6.0
3	Mo	6.5±0.6	14.1±1.4	10.2±1.0
2	Cu	45.4±4.5	74.1±7.4	60.7±6.1
1	Mo	6.7±0.7	13.5±1.3	10.5±1.1
Substrate	Si	-----	-----	-----

Table VII-17. Multilayer Low Bias (-100V) groove bottom layer thickness

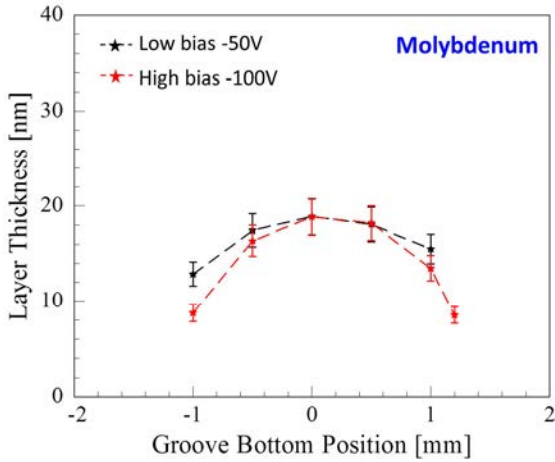


Figure VII-46. Molybdenum layers groove bottom thickness profile

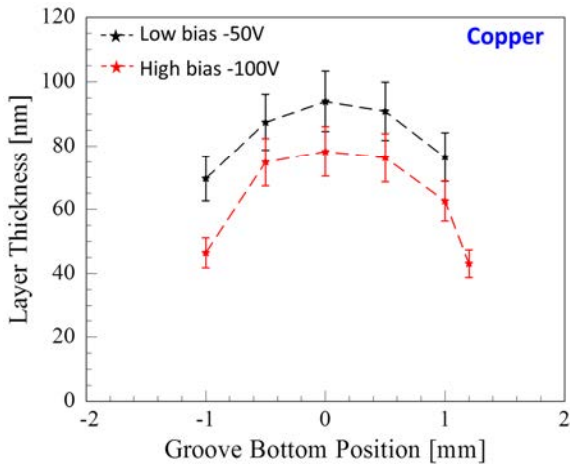


Figure VII-47. Copper layers groove bottom thickness profile

In Figure VII-46 and Figure VII-47 are reported the bottom thickness profile using different bias for both materials.

As supposed close to the bottom angle of mockup groove the rate deposition is lower than in the bottom center, due to the wall shadowing.

Unexpectedly the high biased coating the worst homogeneity and low thickness than the other.

There is not a clear explanation about this phenomenon and it is already under study.

There are two hypothesis that can clarify the anomalous deposition rate.

The first may be describe the higher thickness spread in high bias condition. As a matter of fact the re-sputtered materials is approximatively totally neutral, this material doesn't have intrinsic kinetic energy that permits the adatom mobility on surface. That means it follows basically the ballistic cosine distribution. Based on this reasoning the groove corners have low probability of coating.

The second hypothesis concerns the lower mean thickness of high biased sample. The ions propensity to reach the groove wall depends basically by the ion vector and by the electric field intensity.

The ion vector may be considered identical in both bias voltage case, because that depends mainly by the plasma glow. Instead increase the electric field, reduce the probability of ions to reach the groove bottom, because are more attracted and intercepted by vertical wall.

Any case, the real groove bottom (iris profile) is not flat like in mockup, but it is rounded with 1.2mm radius. That means the thickness profile in final sample will be more homogeneous thanks to the absence of right angle Figure VII-6.

Chapter VIII

Different Analysis Technique Correlation

The different analytical analysis technique used in this thesis individually may provide only to a partial information about the coating process.

The OES-TR is an essential method for the study of HiPIMS discharge evolution but it is not quantitative.

Thus is due to the unknown excitation and emission probability that allows the quantification of each specie.

On the other side the electrical diagnostics allow for a quantification of the charged particles amount, but it can't discriminate the different ionized species.

The same is true for RBS analysis, that allows the thickness quantification but it can't provide information about the original particles nature, neutral or ionized, that reach the substrate.

From each technique it possible to have only partial information, but combining them together, these will provide to give knowledge about the quality of HiPIMS discharge and a reasonable value of ions-neutral ratio.

The data shown below are referred to the low bias deposition (-50V).

The sample holder current pickup integral corresponds to the total charge absorbed by sample holder during the pulse. This charge is caused by:

- Single and double charged Argon ions
- Single charged sputtered materials
- Double charged sputtered materials
- Secondary electron emission induced by ion impact

The charge density absorbed by the sample holder (400cm^2) in a single pulse is:

- $6.9 \cdot 10^{13} \text{ e}^-/\text{cm}^2$ for Molybdenum per pulse
- $8.6 \cdot 10^{13} \text{ e}^-/\text{cm}^2$ for Copper per pulse

The materials deposited correspond to the amount of ionized metal and neutrals, in this case it is necessary a correction due to re-sputtering induced by the ions. Moreover the material measured expressed in atoms/cm² is the result of some minutes of depositions at defined frequency. A final correction is necessary due to sample holder rotation.

After these corrections it has been established a total material amount for each HiPIMS pulse is:

- 3.54*10¹³ atoms/cm² of Molybdenum per pulse
- 1.39*10¹⁴ atoms/cm² of Copper per pulse

OES-TR allows to discriminate the Argon contribution in the pulse charge. This means that excluding an initial Ar⁺ contribution, the sample holder charge absorption may be considerate caused by only metal ions.

In support of this assertion observing the time resolved spectra (Figure VI-18 and Figure VI-21) the ionized Argon peak appears mainly in the first part of discharge, before the sample holder current peak formation.

Comparing the different OES-TR spectra it has been calculated an Argon contribution on total sample holder charge equal to:

- 2% for Molybdenum
- 7% for Copper

Following the previous considerations it is possible to define a system of equations where the fraction of neutral metal (A), single charge metal (B), double charge ion (C) and deposited material (N_a) are correlated to the re-sputtering K₁, K₂ and secondary electron emission coefficients K_{se1} and K_{se2}:

$$\left\{ \begin{array}{l} N_f = A \cdot N_a + B \cdot N_a + C \cdot N_a + \\ \quad - B \cdot N_a \cdot K_1 - C \cdot N_a \cdot K_2 \\ \\ N_f \cdot (1 - Ar) = B \cdot N_a + 2 \cdot C \cdot N_a + \\ \quad + B \cdot N_a \cdot K_{se1} + C \cdot N_a \cdot K_{se2} \\ \\ A + B + C = 1 \end{array} \right. \quad \text{VIII-1)}$$

Where:

- A is neutral metal fraction (Me)
- B is single charge metal ions fraction (Me⁺)
- C is double charge metal ions fraction (Me⁺⁺)
- N_f is the number of atoms (atoms/cm²) measured in RBS analysis
- N_a is the effective deposited particles (neutral and ionized)
- K₁ is the sputtering yield of single charge ion
- K₂ is the sputtering yield of double charge ion
- K_{se1} is secondary electron emission coefficient of single charge ion
- K_{se2} is secondary electron emission coefficient of double charge ion
- Ar is the correction coefficient for sample holder charge integral ascribed to Argon ions

Furthermore it may be supposed that the amount of double charge ions is lower than single charge ions

$$B > C \quad \text{VIII-2)}$$

Kipping C as independent variable, and resolving the previous system we obtain:

$$B = \frac{\frac{N_e}{N_a} - \frac{N_e}{N_a} \cdot C \cdot k_2 - C \cdot (2 + k_{se2})}{1 + k_{se1} + \frac{N_e}{N_a} * k_1} \quad \text{VIII-3)}$$

The SEE and re-sputtering coefficients are extrapolated by the literature [124], [139] and calculated (Figure VII-8) respectively.

For copper, due to the lower power density of the discharge, we may assume C=0: the fraction of single charged Cu⁺ ions is than about 27%.

For Molybdenum the presence of Mo^{++} ions cannot be neglected ($C \neq 0$). In this case the fraction of single charged Mo^+ follows from the estimated value of C (Figure VIII-1).

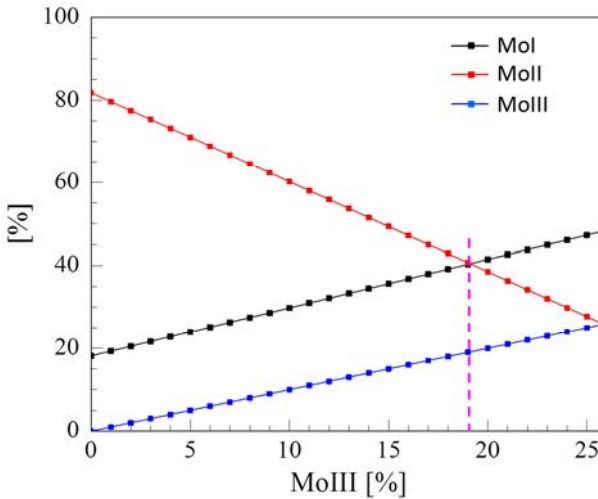


Figure VIII-1. Different solution of eq.VIII-3) relative to low bias deposition

There are few literature data reporting the relation of the content of single and double charged ions in HiPIMS discharges. In [140] similar experimental conditions and the same power supply were used in the case of Titanium. The results are shown in Figure VIII-2.

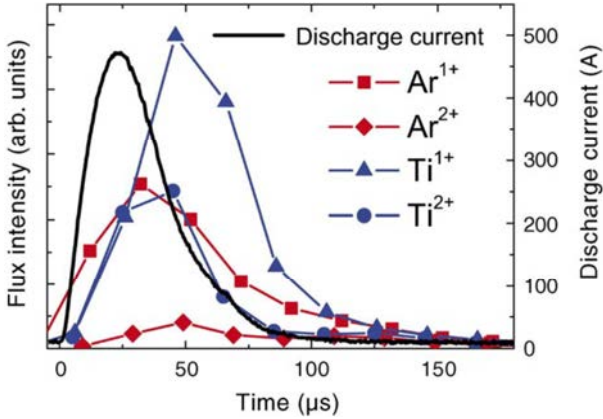


Figure VIII-2. The relative flux composition of singly and doubly ionized Ar and Ti from the HIPIMS plasma [140]

As it can be seen in Figure VIII-1 (assuming again $C < B$) quite reasonable value of $\text{Mo}^+/\text{Mo}^{++}$ may be obtained.

For the deposition at higher bias (-100V) similar results are obtained after changing the sputtered and SEE coefficients to account for the increased Mo^{++} energy.

Chapter IX

General conclusions and Future perspectives

The damaged cavity iris has been analyzed using electron scanning microscope, in order to investigate the damage level after accelerated test. The analysis confirms, as reported in literature, the degradation of cavity surface due to thermal fatigue induced by cyclical RF pulse heating. The analysis show a high damage due to electrical discharge and thermal fatigue. On cavity surfaces are observed all fatigue damage types, roughness induced by dislocation pileup, grain boundary damages and cracks.

Throughout all the experimental work, the sputtering chamber has been continuously upgraded with ad hoc designed mechanical components. These components allowed to change the experimental configuration in order to improve the coating quality and deposition rate. The Titanium gettering subsystem prevent strong oxidation in metals coating. The absence of oxygen has been confirmed by RBS analysis. The cooled sample holder maintains the sample at low temperature ($T < 80^{\circ}\text{C}$) during the deposition.

The electrical study confirms the right generation of HiPIMS discharge, for both target materials and both HiPIMS power supplies. The discharge has been monitored during long time deposition, it maintains the electrical characteristics in time and the reproducibility, with a variation lower than 6% in the worst case of Sinex power supply. This study has been fundamental for the power supply parameter setting. The magnetron peak power density obtained in HiPIMS discharge in deposition configuration is $0.7\text{KW}/\text{cm}^2$ and $1.2\text{KW}/\text{cm}^2$ for Copper and Molybdenum respectively. The peak current density is $1\text{A}/\text{cm}^2$ for Copper target and $1.2\text{A}/\text{cm}^2$ for Molybdenum.

The ionization ratio of materials that reach the sample external point is higher than 60% for Molybdenum and close to 27% for Copper.

Copper HiPIMS discharge may be improved by increasing the power density which will increase the metallic ion fraction.

The low power density used in this work is due basically to arc formation on mockup structure (residual oxide and non-homogeneous electrical field due to silicon wafer and aluminum corners). Using a smoother sample, like the final mandrel, the increment of power density and Copper ions fraction is possible.

The sample holder pickup current measurements confirm the metallic ion bombardment on sample surfaces.

The designed DC bias RC filter maintains the sample negative polarization and bombardment during all the HiPIMS discharge. It has been measured that the voltage bias variation is lower than 5V.

Optical emission spectroscopy permitted to diagnose the presence of target metal ions created by HiPIMS discharge.

Moreover using the time resolved OES recorded the evolution of plasma species created in discharge.

The OES-TR measurement setup designed and developed allows the study of excited species in any position of chamber, also close to sample holder where it is known that the light signal is very weak.

It has been defined that the HiPIMS discharge evolves in self sputtering mode with the formation of gas depletions close to magnetron and in all the volume between target and sample holder.

Furthermore it has been demonstrated that a correlation between the sample holder current second peak and the intensification of metal ion flux exists.

About the coating the nanostructured multilayer coating has been successful realized onto all groove surface, using PVD HiPIMS technique.

The multilayers have been analyzed with different techniques, AFM, SEM, RBS.

The nanostructured multilayer shows a roughness mean value lower than 2nm in 0.5 μ m coating thick measured in external position in -100V sample holder bias.

SEM and STEM images show a complete material crystallization in each layer. Moreover it is not observed thickness variations or wave modulations typical in low quality multilayer. Furthermore the interfaces are well defined without material intermixing. It is also confirmed by RBS analysis observing the absence of tails between peaks.

Using RBS techniques the thickness of each layer in different sample points has been measured, in order to evaluate the deposition rate variations induced by groove shadowing effect.

The bias voltage has a strong influence on layer thickness. Re-sputtering is the main effect of increasing the voltage bias. This involves material loss relative to sample positioned externally to groove and relative to the point close groove aperture.

Despite the deposition loss, the use of high bias voltage it is recommended due to the higher thickness homogeneity onto groove vertical wall.

As a matter of fact the thickness ratio between deeper point (1mm) and the point close groove aperture (9mm) onto vertical wall decrease strongly in high voltage bias configuration. The thickness ratio is close to 5.3 in -50V bias configuration and 2.4 in -100V configuration.

The research in this specific sputtering application is still at the beginning. Future studies on the mechanical and electrical characteristics of multilayer are planned.

About mechanical testing, it would be necessary to design ad hoc high frequency device that allow to investigate the multilayer fatigue damage in the same cycle range of cavity final application, up to 10^8 cycles.

To complete the feasibility study it will be essential to realize a complete X-band cavity in order to test it at the SLAC accelerator facility.

About time resolved optical emission spectroscopy, it is demonstrated that it is a great tool for plasma composition analysis.

Coupling this technique with sample holder current pickup measurements, it will possible to discern the type and the amount of each specie that reaches the sample.

Unfortunately the OES-TR is not efficient for afterglow phenomena study, because the light emission is directly related to free electrons energy and density, that generally drop after the end of pulse.

Finally it is demonstrate that the HiPIMS technique has proved to be suitable to produce good quality nanostructured multilayer coatings in all points of mandrel mockup, and it is suitable for X-band cavity protective multilayer coating.

References

- [1] S. Calatroni, S. Heikkinen, T. Ramsvik, S. Sgobba, M. Taborelli, and W. Wuensch, “Material Selection and Characterization for,” *PAC07*, no. June, 2007.
- [2] M. Fenger and G. C. Stone, “Progress in understanding the nature,” no. March 2007, pp. 363–368.
- [3] B. Spataro *et al.*, “High-power comparison among brazed, clamped and electroformed X-band cavities,” *Nucl. Instruments Methods Phys. Res. Sect. A Accel. Spectrometers, Detect. Assoc. Equip.*, vol. 657, no. 1, pp. 88–93, 2011.
- [4] a. Misra, H. Kung, D. Hammon, R. Hoagland, and M. Nastasi, “Damage Mechanisms in Nanolayered Metallic Composites,” *Int. J. Damage Mech.*, vol. 12, no. 4, pp. 365–376, 2003.
- [5] M. R. Stoudt, R. C. Cammarata, and R. E. Ricker, “Nanometer-Scale Multilayered Coatings,” *Scr. Mater.*, vol. 43, pp. 491–496, 2000.
- [6] R. B. Palmer, “Q;JL—313 93 DCS2 Oil211,” in *AIP conference*, 1982, vol. 91, p. 179.
- [7] W. Gai, G. Hoffstaetter, M. Hogan, and V. Shiltsev, “Accelerator Technology Test-Beds and Test Beams,” pp. 1–56, 2013.
- [8] J. W. Kovermann, “Comparative studies of high-gradient RF and DC breakdowns,” 2010.
- [9] CERN, “CLIC WEBSITE <http://clic-study.web.cern.ch/>.” .
- [10] R. Ruber, “CLICintroRuber.” .
- [11] I. S. Ko, “Beam Dynamics Newsletter 63,” no. 63, 2014.
- [12] S. Boucher *et al.*, “Compact, inexpensive X-band linacs as radioactive isotope source replacements,” *IPAC 2013 Proc. 4th Int.*

- Part. Accel. Conf.*, no. May, pp. 3746–3748, 2013.
- [13] T. Yamamoto, T. Natsui, F. Sakamoto, and M. Uesaka, “Development of Portable X-Band Linac X-Ray Source for Non-Destructive Testing,” *Corrosion*, pp. 1–6, 2008.
- [14] C. Tang, H. Chen, Y. Liu, and X. Wang, “Low-Energy Linacs and Their Applications in Tsinghua University,” *Proc. LINAC 2006*, pp. 256–258, 2006.
- [15] Y. Seki, J. M. Bereder, and M. Uesaka, “DEVELOPMENT OF MOBILE NEUTRON SOURCES DRIVEN BY X-BAND ELECTRON LINACS FOR INFRASTRUCTURE MAINTENANCE AND NUCLEAR SECURITY,” *Proc. IPAC2016*, pp. 2–4, 2016.
- [16] “rapidscan.” .
- [17] G. D. Auria, “Application of X-Band Linacs,” pp. 724–728.
- [18] G. Burt, “Security_Discussion.” .
- [19] C. Tang, H. Chen, and Y. Liu, “Electron Linacs for Cargo Inspection and Other Industrial Applications,” *Int. Top. Meet. Nucl. Res. Appl. Util. Accel.*, no. May, pp. 4–8, 2009.
- [20] S. Hanna, “Applications of X-band technology in medical accelerators,” ... *Accel. Conf. 1999. Proc. ...*, pp. 2516–2518, 1999.
- [21] M. L. M. et Al., “The Mobetron: A New Concept for Intraoperative Radiotherapy,” in *6th International IORT Symposium*, 1996.
- [22] S. G. C. et Al, “The CyberKnife: Beta System Description and Initial Clinical Results,” *J. Radiosurgery*, vol. 1, no. 4, 1998.
- [23] J. Jang and M. Uesaka, “DEVELOPMENT OF A COMPACT X-BAND ELECTRON LINAC FOR PRODUCTION OF Mo-99 / Tc-99m DESIGNING A COMPACT X-BAND,” *Proc. IPAC2016*, pp. 1917–1920, 2016.

-
- [24] N. H. Quyet *et al.*, “Compact X-Band (11 . 424 Ghz) Linac for Cancer Therapy,” *World*, pp. 2670–2672, 2004.
- [25] Nuclear Energy Agency, “The Supply of Medical Radioisotopes: An Assessment of Long-term Global Demand,” *Radioisotopes*, no. June, 2011.
- [26] B. Spataro *et al.*, “Technological issues and high gradient test results on X-band molybdenum accelerating structures,” *Nucl. Instruments Methods Phys. Res. Sect. A Accel. Spectrometers, Detect. Assoc. Equip.*, vol. 657, no. 1, pp. 114–121, 2011.
- [27] V. A. Dolgashev, “Progress on high-gradient structures,” *AIP Conf. Proc.*, vol. 1507, pp. 76–84, 2012.
- [28] Heikkinen, *Thermally Induced Ultra High Cycle Fatigue of Copper Alloys of the High Gradient*. 2010.
- [29] S. Bini *et al.*, “Development of X-band accelerating structures for high gradients,” *Chinese Phys. C*, vol. 36, no. 7, pp. 639–647, 2012.
- [30] A. Marcelli *et al.*, “Characterization of thick conducting molybdenum films: Enhanced conductivity via thermal annealing,” *Surf. Coatings Technol.*, vol. 261, pp. 391–397, 2015.
- [31] V. Rigato, M. Campostrini, W. Raniero, G. Della Mea, and B. Spataro, “Deposition of Cu / Mo Multilayers by Bias HiPIMS for X-Band Accelerating Structures,” vol. 3, pp. 3–4.
- [32] G. Gatti *et al.*, “X-band accelerator structures: On going R&D at the INFN,” *Nucl. Instruments Methods Phys. Res. Sect. A Accel. Spectrometers, Detect. Assoc. Equip.*, 2015.
- [33] P. L. M. Klesnil, *Fatigue of metallic materials*, 2th ed. Academia/Elsevier, 1992.
- [34] H. Mughrabi, “On the life-controlling microstructural fatigue mechanisms in ductile metals and alloys in the gigacycle regime,”

- Fatigue Fract. Eng. Mater. Struct.*, vol. 22, no. 7, pp. 633–641, 1999.
- [35] H. Mughrabi, “Specific features and mechanisms of fatigue in the ultrahigh-cycle regime,” *Int. J. Fatigue*, vol. 28, no. 11, pp. 1501–1508, 2006.
- [36] S. Nishijima and K. Kanazawa, “Stepwise S-N curve and fish-eye failure in gigacycle fatigue,” *Fatigue Fract. Eng. Mater. Struct.*, vol. 22, no. 7, pp. 601–607, 1999.
- [37] N. Phung *et al.*, “Microplasticity and energy dissipation in very high cycle fatigue,” *PhD thesis*, 2013.
- [38] C. Bathias, “There is no infinite fatigue life in metallic materials,” *Fatigue Fract. Eng. Mater. Struct.*, vol. 22, no. 7, pp. 559–565, 1999.
- [39] S. V. Kuzikov and M. E. Plotkin, “Theory of thermal fatigue caused by RF pulsed heating,” *Int. J. Infrared Millimeter Waves*, vol. 29, no. 3, pp. 298–311, 2008.
- [40] Ristau Detlev, “Laser induced damage in optical materials,” 2015.
- [41] D. Pritzkau, “RF Pulsed Heating,” no. December, 2001.
- [42] M. Aicheler, “Influence of grain orientation on evolution of surface features in fatigued polycrystalline copper: A comparison of thermal and uniaxial mechanical fatigue results,” *J. Phys. Conf. Ser.*, vol. 240, p. 12051, 2010.
- [43] V. Dolgashev, “Recent High Gradient Tests at SLAC Presented on behalf of collaboration by,” no. April, pp. 17–20, 2012.
- [44] L. Laurent *et al.*, “Experimental study of rf pulsed heating,” *Phys. Rev. Spec. Top. - Accel. Beams*, vol. 14, no. 4, pp. 1–21, 2011.
- [45] S. Stanzl-Tschegg, H. Mughrabi, and B. Schoenbauer, “Life time and cyclic slip of copper in the VHCF regime,” *Int. J. Fatigue*, vol.

- 29, no. 9–11, pp. 2050–2059, 2007.
- [46] J. Pol?k and J. Man, “Initiation of stage i fatigue cracks - Experiments and models,” *Procedia Eng.*, vol. 101, no. C, pp. 386–394, 2015.
- [47] N. L. Phung *et al.*, “Very High Cycle Fatigue for single phase ductile materials: Slip band appearance criterion,” *Procedia Eng.*, vol. 66, pp. 615–625, 2013.
- [48] “1 2 1 + 2,” *October*, pp. 1–11, 2009.
- [49] Z. F. Zhang and Z. G. Wang, “Dependence of intergranular fatigue cracking on the interactions of persistent slip bands with grain boundaries,” *Acta Mater.*, vol. 51, no. 2, pp. 347–364, 2003.
- [50] D. P. Pritzkau and R. H. Siemann, “Experimental study of rf pulsed heating on oxygen free electronic copper,” *Phys. Rev. Spec. Top. - Accel. Beams*, vol. 5, no. 11, pp. 18–39, 2002.
- [51] S. V. Kuzikov and M. E. Plotkin, “Theory of Thermal Fatigue of a Copper Surface Under the Action of Pulsed Microwave Heating,” no. 4, pp. 0–2, 2008.
- [52] V. Dolgashev, “Experiments on Gradient Limits for Normal Conducting Accelerators,” *LINAC 2002, Korea*, no. August, pp. 264–268, 2002.
- [53] A. Descoedres, T. Ramsvik, S. Calatroni, M. Taborelli, and W. Wuensch, “Dc breakdown conditioning and breakdown rate of metals and metallic alloys under ultrahigh vacuum,” *Phys. Rev. Spec. Top. - Accel. Beams*, vol. 12, no. 3, pp. 1–8, 2009.
- [54] V. A. Dolgashev, S. G. Tantawi, M. Park, Y. Higashi, and B. Spataro, “Study of Basic Rf Breakdown Phenomena in High Gradient Vacuum Structures *,” *Proc. Linear Accel. Conf. LINAC2010*, pp. 1043–1047, 2010.

- [55] H. Timko *et al.*, “From field emission to vacuum arc ignition: A new tool for simulating copper vacuum arcs,” *Contrib. to Plasma Phys.*, vol. 55, no. 4, pp. 299–314, 2015.
- [56] K. Yokoyama *et al.*, “Breakdown Characteristics in Dc Spark Experiments of Copper Focusing on Purity and Hardness,” pp. 229–231.
- [57] A. Grudiev, S. Calatroni, and W. Wuensch, “New local field quantity describing the high gradient limit of accelerating structures,” *Phys. Rev. Spec. Top. - Accel. Beams*, vol. 12, no. 10, p. 102001, 2009.
- [58] B. R. H Fowler and L. Nordheim, “Electron Emission in Intense Electric Fields,” *Phys. Rev. Proc. Nat. Ac. Sci. Roy. Soc. Proc. Z. f. Phys.*, vol. 14, no. 47, pp. 80–51, 1923.
- [59] C. Z. Antoine, F. Peauger, and F. Le Pimpec, “Electromigration occurrences and its effects on metallic surfaces submitted to high electromagnetic field: A novel approach to breakdown in accelerators,” *Nucl. Instruments Methods Phys. Res. Sect. A Accel. Spectrometers, Detect. Assoc. Equip.*, vol. 665, pp. 54–69, 2011.
- [60] N. C. Shipman, “Experimental study of DC vacuum breakdown and application to high-gradient accelerating structures for CLIC,” *PhD thesis*, pp. 1–196, 2014.
- [61] D. I. P. G.A .Mesyats, *Pulsed Electrical Discharge in Vacuum*. 1989.
- [62] W. H. Hayward and A. R. Wolter, “Sputtering yield measurements with low-energy metal ion beams,” *J. Appl. Phys.*, vol. 40, no. 7, pp. 2911–2916, 1969.
- [63] H. Timko *et al.*, “Mechanism of surface modification in the plasma-surface interaction in electrical arcs,” *Phys. Rev. B - Condens.*

- Matter Mater. Phys.*, vol. 81, no. 18, pp. 1–8, 2010.
- [64] H. Cern, “SEM inspection of 30 GHz quadrant,” 2008.
- [65] H. Cern, “SEM inspection of 30CNSQ-Tk . Cu # 2 (NDS4 _ thick) structure after CTF-3 test,” vol. 2, 2008.
- [66] J. Lienig, “Introduction to electromigration-aware physical design,” *Proc. 2006 Int. Symp. Phys. Des. - ISPD '06*, no. 1, p. 39, 2006.
- [67] V. Dolgashev, S. Tantawi, Y. Higashi, and B. Spataro, “Geometric dependence of radio-frequency breakdown in normal conducting accelerating structures,” *Appl. Phys. Lett.*, vol. 97, no. 17, pp. 1–4, 2010.
- [68] A. Inspektor and P. A. Salvador, “Architecture of PVD coatings for metalcutting applications: A review,” *Surf. Coatings Technol.*, vol. 257, pp. 138–153, 2014.
- [69] E. Bousser, “Solid particle erosion mechanisms of protective coatings for aerospace applications,” *PhD thesis*, 2013.
- [70] J. R. Greer and J. T. M. De Hosson, “Plasticity in small-sized metallic systems: Intrinsic versus extrinsic size effect,” *Prog. Mater. Sci.*, vol. 56, no. 6, pp. 654–724, 2011.
- [71] O. A. Hammadi, “Fundamentals of Plasma Sputtering.”
- [72] D. M. Mattox, *The history of vacuum coating technology*. 2002.
- [73] A. Anders, “Discharge physics of high power impulse magnetron sputtering,” *Surf. Coatings Technol.*, vol. 205, no. SUPPL. 2, pp. S1–S9, 2011.
- [74] C. Christou and Z. H. Barber, “Ionization of sputtered material in a planar magnetron discharge,” *J. Vac. Sci. Technol. A Vacuum, Surfaces, Film.*, vol. 18, no. 6, p. 2897, 2000.
- [75] LIANG MENG, “Comparison of plasmas in high power pulsed and modulated pulse power magnetron sputtering,” *PhD thesis*, pp. 1–1,

- 2013.
- [76] F. M. M. B.A.Movchan, A.V. Demchishin, “No Title,” *Phys. Met. Metallogr.*, vol. 28, p. 653, 1969.
- [77] P. B. Barna and M. Adamik, “Fundamental structure forming phenomena of polycrystalline films and the structure zone models,” *Thin Solid Films*, vol. 317, pp. 27–33, 1998.
- [78] J. A. Thornton, “Influence of apparatus geometry and deposition conditions on the structure and topography of thick sputtered coatings,” *J. Vac. Sci. Technol.*, vol. 11, no. 4, p. 666, 1974.
- [79] V. Kouznetsov, K. Macák, J. M. Schneider, U. Helmersson, and I. Petrov, “A novel pulsed magnetron sputter technique utilizing very high target power densities,” *Surf. Coatings Technol.*, vol. 122, no. 2–3, pp. 290–293, 1999.
- [80] U. Helmersson, M. Lättemann, J. Bohlmark, A. P. Ehiasarian, and J. T. Gudmundsson, “Ionized physical vapor deposition (IPVD): A review of technology and applications,” *Thin Solid Films*, vol. 513, no. 1–2, pp. 1–24, 2006.
- [81] A. P. Ehiasarian, A. Vetushka, A. Hecimovic, and S. Konstantinidis, “Ion composition produced by high power impulse magnetron sputtering discharges near the substrate,” *J. Appl. Phys.*, vol. 104, no. 8, 2008.
- [82] J. Alami, J. T. Gudmundsson, J. Bohlmark, J. Birch, and U. Helmersson, “Plasma dynamics in a highly ionized pulsed magnetron discharge,” *Plasma Sources Sci. Technol.*, vol. 14, no. 3, pp. 525–531, 2005.
- [83] A. P. Ehisarian, R. New, W.-D. Münz, L. Hultman, U. Helmersson, and V. Kouznetsov, “Influence of high power densities on the composition of pulsed magnetron plasma,” *Vacuum*, vol. 65,

- no. 2, pp. 147–154, 2002.
- [84] S. Schiller, K. Goedicke, J. Reschke, V. Kirchhoff, S. Schneider, and F. Milde, “Pulsed magnetron sputter technology,” *Surf. Coatings Technol.*, vol. 61, no. 1–3, pp. 331–337, 1993.
- [85] A. Belkind, A. Freilich, and R. Scholl, “Using pulsed direct current power for reactive sputtering of Al₂O₃,” *J. Vac. Sci. Technol. A Vacuum, Surfaces, Film.*, vol. 17, no. 4, p. 1934, 1999.
- [86] A. Anders, “A structure zone diagram including plasma-based deposition and ion etching,” *Thin Solid Films*, vol. 518, no. 15, pp. 4087–4090, 2010.
- [87] A. P. Ehiasarian, J. G. Wen, and I. Petrov, “Interface microstructure engineering by high power impulse magnetron sputtering for the enhancement of adhesion,” *J. Appl. Phys.*, vol. 101, no. 5, 2007.
- [88] J. T. Gudmundsson, “The high power impulse magnetron sputtering discharge as an ionized physical vapor deposition tool,” *Vacuum*, vol. 84, no. 12, pp. 1360–1364, 2010.
- [89] V. Kouznetzov, “US Patent No. US 6296742 B1,” 2001.
- [90] J. Hopwood, “Ionized physical vapor deposition of integrated circuit interconnects *,” *Phys. Plasmas*, vol. 5, no. 5, pp. 1624–1631, 1998.
- [91] A. Anders, “A review comparing cathodic arcs and high power impulse magnetron sputtering (HiPIMS),” *Surf. Coatings Technol.*, vol. 257, pp. 308–325, 2014.
- [92] A. Hecimovic, V. Schulz-von der Gathen, M. Böke, A. von Keudell, and J. Winter, “Spoke transitions in HiPIMS discharges,” *Plasma Sources Sci. Technol.*, vol. 24, no. 4, p. 45005, 2015.
- [93] J. Andersson and A. Anders, “Gasless sputtering: Opportunities for ultraclean metallization, coatings in space, and propulsion,” *Appl.*

- Phys. Lett.*, vol. 92, no. 22, 2008.
- [94] J. Lin *et al.*, “Ion energy and mass distributions of the plasma during modulated pulse power magnetron sputtering,” *Surf. Coatings Technol.*, vol. 203, no. 24, pp. 3676–3685, 2009.
- [95] J. T. Gudmundsson, J. Alami, and U. Helmersson, “Spatial and temporal behavior of the plasma parameters in a pulsed magnetron discharge,” *Surf. Coatings Technol.*, vol. 161, no. 2–3, pp. 249–256, 2002.
- [96] A. Anders, J. Andersson, and A. Ehiasarian, “High power impulse magnetron sputtering: Current-voltage-time characteristics indicate the onset of sustained self-sputtering,” *J. Appl. Phys.*, vol. 102, no. 11, pp. 1–11, 2007.
- [97] S. M. Rossnagel, “Gas density reduction effects in magnetrons,” *J. Vac. Sci. Technol. A Vacuum, Surfaces, Film.*, vol. 6, no. 1, p. 19, 1988.
- [98] M. Palmucci, N. Britun, S. Konstantinidis, and R. Snyders, “Rarefaction windows in a high-power impulse magnetron sputtering plasma,” *J. Appl. Phys.*, vol. 114, no. 11, 2013.
- [99] D. W. Hoffman, “A sputtering wind,” *J. Vac. Sci. Technol. A Vacuum, Surfaces, Film.*, vol. 3, no. 3, p. 561, 1985.
- [100] K. B. Gylfason, J. Alami, U. Helmersson, and J. T. Gudmundsson, “Ion-acoustic solitary waves in a high power pulsed magnetron sputtering discharge,” *J. Phys. D. Appl. Phys.*, vol. 38, no. 18, pp. 3417–3421, 2005.
- [101] H. K. N. Hosokawa, T. Tsukada, “No Title,” *Proc. 8th Int. Vac. Congr.*, 1980.
- [102] E. Oks and A. Anders, “A self-sputtering ion source: a new approach to quiescent metal ion beams.,” *Rev. Sci. Instrum.*, vol.

- 81, no. 2, p. 02B306, 2010.
- [103] J. Alami *et al.*, “Phase tailoring of Ta thin films by highly ionized pulsed magnetron sputtering,” *Thin Solid Films*, vol. 515, no. 7–8, pp. 3434–3438, 2007.
- [104] K. Sarakinos, J. Alami, and M. Wuttig, “Process characteristics and film properties upon growth of {TiO} x films by high power pulsed magnetron sputtering,” *J. Phys. D. Appl. Phys.*, vol. 40, no. 7, p. 2108, 2007.
- [105] J. T. Gudmundsson, N. Brenning, D. Lundin, and U. Helmersson, “High power impulse magnetron sputtering discharge,” *J. Vac. Sci. Technol. A Vacuum, Surfaces, Film.*, vol. 30, no. May, pp. 30801–34, 2012.
- [106] D. Lundin, P. Larsson, E. Wallin, M. Lattemann, N. Brenning, and U. Helmersson, “Cross-field ion transport during high power impulse magnetron sputtering,” *Plasma Sources Sci. Technol.*, vol. 17, no. 3, p. 35021, 2008.
- [107] M. Samuelsson, D. Lundin, J. Jensen, M. A. Raadu, J. T. Gudmundsson, and U. Helmersson, “On the film density using high power impulse magnetron sputtering,” *Surf. Coatings Technol.*, vol. 205, no. 2, pp. 591–596, 2010.
- [108] S. Konstantinidis, J. P. Dauchot, M. Ganciu, A. Ricard, and M. Hecq, “Influence of pulse duration on the plasma characteristics in high-power pulsed magnetron discharges,” *J. Appl. Phys.*, vol. 99, no. 1, pp. 10–15, 2006.
- [109] E. Wallin and U. Helmersson, “Hysteresis-free reactive high power impulse magnetron sputtering,” *Thin Solid Films*, vol. 516, no. 18, pp. 6398–6401, 2008.
- [110] K. Wasa and S. Hayakawa, *Handbook of sputter deposition*

- technology*. 1992.
- [111] D. M. Mattox, *Front-matter*. 2010.
- [112] C. R. M. Grovenor, H. T. G. Hentzell, and D. A. Smith, “The Development of Grain Structure During Growth of Metallic Films,” *Acta Metall.*, vol. 32, no. 5, pp. 773–781, 1984.
- [113] W. Ensinger, “Low energy ion assist during deposition — an effective tool for controlling thin film microstructure,” *Nucl. Instruments Methods Phys. Res. Sect. B Beam Interact. with Mater. Atoms*, vol. 127–128, no. 97, pp. 796–808, 1997.
- [114] J. Alami, K. Sarakinos, F. Uslu, and M. Wuttig, “On the relationship between the peak target current and the morphology of chromium nitride thin films deposited by reactive high power pulsed magnetron sputtering,” *J. Phys. D. Appl. Phys.*, vol. 42, no. 1, p. 15304, 2009.
- [115] F. Ferreira, R. Serra, A. Cavaleiro, and J. C. Oliveira, “Additional control of bombardment by deep oscillation magnetron sputtering: Effect on the microstructure and topography of Cr thin films,” *Thin Solid Films*, vol. 619, pp. 250–260, 2016.
- [116] J. Alami, P. O. Å. Persson, D. Music, J. T. Gudmundsson, J. Bohlmark, and U. Helmersson, “Ion-assisted physical vapor deposition for enhanced film properties on nonflat surfaces,” *J. Vac. Sci. Technol. A Vacuum, Surfaces, Film.*, vol. 23, no. 2, p. 278, 2005.
- [117] P. Siemroth and T. Schülke, “Copper metallization in microelectronics using filtered vacuum arc deposition - principles and technological development,” *Surf. Coatings Technol.*, vol. 133–134, pp. 106–113, 2000.
- [118] J. Lu and M. J. Kushner, “Trench filling by ionized metal physical

- vapor deposition,” *J. Vac. Sci. Technol. A Vacuum, Surfaces, Film.*, vol. 19, no. 5, p. 2652, 2001.
- [119] K. Bobzin, N. Bagcivan, P. Immich, S. Bolz, J. Alami, and R. Cremer, “Advantages of nanocomposite coatings deposited by high power pulse magnetron sputtering technology,” *J. Mater. Process. Technol.*, vol. 209, no. 1, pp. 165–170, 2009.
- [120] a. P. Ehiasarian and W. D. Münz, “High power pulsed magnetron sputtered CrN x films,” *Surf. Coat. Technol.*, vol. 163–164, pp. 267–272, 2003.
- [121] M. Kildemo, S. Calatroni, and M. Taborelli, “Breakdown and field emission conditioning of Cu, Mo, and W,” *Phys. Rev. Spec. Top. - Accel. Beams*, vol. 7, no. 9, pp. 82–88, 2004.
- [122] S. V. Starikov and V. V. Pisarev, “Atomistic simulation of laser-pulse surface modification: Predictions of models with various length and time scales,” *J. Appl. Phys.*, vol. 117, no. 13, 2015.
- [123] A. V. Phelps and Z. L. Petrovic, “Cold-cathode discharges and breakdown in argon: surface and gas phase production of secondary electrons,” *Plasma Sources Sci. Technol.*, vol. 8, no. 3, pp. R21–R44, 1999.
- [124] P. C. Zalm and L. J. Beckers, “Ion-Induced Secondary Electron Emission from Copper and Zinc,” *Surf. Sci.*, vol. 153, pp. 135–141, 1985.
- [125] TAKASHI FUJIMOTO, “Plasma Spectroscopy,” *Profiles Drug Subst. Excip. Relat. Methodol.*, vol. 36, p. ii, 2011.
- [126] N. Britun, T. Minea, S. Konstantinidis, and R. Snyders, “Plasma diagnostics for understanding the plasma–surface interaction in HiPIMS discharges: a review,” *J. Phys. D. Appl. Phys.*, vol. 47, no. 22, p. 224001, 2014.

-
- [127] J. W. Kovermann, S. Calatroni, A. Descoedres, T. Lefèvre, and W. Wuensch, “Advanced Experimental Techniques for RF and DC Breakdown Research,” *Proc. EPAC08, Genoa, Italy*, pp. 775–777.
- [128] J. Kovermann, “CLIC Breakdown workshop May 20, 2008 Jan Kovermann,” 2008.
- [129] H. Walther, *Excitation of Atoms and Broadening of Spectral Lines*. .
- [130] verity instruments Inc., “Optical_emission_analysis.pdf,” <https://www.verityinst.com/>.
- [131] “<https://oceanoptics.com/>.” .
- [132] “<https://www.avantes.com/>.” .
- [133] “NIST atomic spectra database.” [Online]. Available: http://physics.nist.gov/PhysRefData/ASD/lines_form.html.
- [134] N. Britun, S. Konstantinidis, and R. Snyders, “An Overview on Time-Resolved Optical Analysis of HiPIMS Discharge,” *Plasma Process. Polym.*, vol. 12, no. 9, pp. 1010–1027, 2015.
- [135] J. Olejnicek *et al.*, “Optical emission spectroscopy of High Power Impulse Magnetron Sputtering (HiPIMS) of CIGS thin films,” *2014 IEEE 40th Photovolt. Spec. Conf. PVSC 2014*, pp. 1666–1669, 2014.
- [136] A. Anders, *Handbook of Plasma Immersion Ion Implantation and Deposition*. .
- [137] K. Sarakinos, J. Alami, and S. Konstantinidis, “High power pulsed magnetron sputtering: A review on scientific and engineering state of the art,” *Surf. Coatings Technol.*, vol. 204, no. 11, pp. 1661–1684, 2010.
- [138] P. M. V. Rigato, A. Patelli, G. Maggioni, G. Salmaso, V. Mattarello, M.G. Pelizzo, P. Nicolosi, L. Depero , E. Bontempi,

- “Investigation into the properties of titanium based films deposited using pulsed magnetron sputtering,” *Surf. Coatings Technol.*, vol. 174–175, pp. 720–724, 2003.
- [139] G. L. Cano and G. L. Cano, “Secondary electron emission from Au, Mo, and CuBe by high-charge-number laserproduced metal ions,” *J. Appl. Phys.*, vol. 44, p. 5293, 1973.
- [140] J. Bohlmark, M. Lattemann, J. T. Gudmundsson, A. P. Ehasarian, and Y. A. Gonzalvo, “The ion energy distributions and ion flux composition from a high power impulse magnetron sputtering discharge,” vol. 515, pp. 1522–1526, 2006.

Appendix

10.1 Instrumentations Details

10.1.1 PVD sputtering chamber

Rectangular steal chamber
designed at LNL laboratory

Access point:

- 2 covers
- 1 CF300
- 5 CF200
- 11 CF150
- 15 CF35
- 6 CF16



10.1.2 Pumping system

- One Varian V1200 (1200l/s)
- One Edwards double stage (80m³/h)

10.1.3 Power supply

- Hüttinger 4001 HiPIMS (4-1000Hz, 5-200 μ s, 0-1000V)
- Sinex 1.2 HiPIMS power supply (0-260Vac)
- Two Delta elektronica ES:03-5 DC (0-30V 0-4A)
- Kepco BOP100 DC (-100/+100V, 0-4A)
- MKS ENI RPG50 pulsed-DC/DC (0-250kHz, 0-800V, 0-10A)
- Senvac Maris GS-05 DC

10.1.4 Pressure Gauge

- One Pfeiffer Pirani Type010
- Two Balzer penning IKR020
- One Pfeiffer full range PKR251
- One Capacitance monometer MKS Baratron (50mTorr)

10.1.5 Optical emission spectroscopy

- Optical fiber cable, plastic-clad-silica (Verity Instruments Inc.)
- Optical head with collimating quartz lens (Verity Instruments Inc.)
- Vacuum Feedthroughs (Verity Instruments Inc.)
- Spectrometer Ocean Optics_Maya2000PRO (bi-dimensional CCD array, 0.9nm resolution, 200-1100nm range)
- Spectrometer Avantes AvaSpec Multichannel Spectrometers (0.2nm resolution, 344-736nm range)
- Monochromator Spectral Products DK240 (Grating:2400g.240nm, 1200g.500nm, unilateral slits in- out 10-1000 μ m, max resolution 0.1nm)
- Hamamatsu photomultiplier R1104
- NIM (Ortec SCA550, Ortec quad fast amplifier 535, Ortec DC-HV power supply 456, Caen dual attenuator 110)
- Digitizer Caen DT5751 (1GHz/s, 10bit)

10.1.6 Discharge diagnostic

- Lecroy wave runner 6030 oscilloscope
- Tektronix TCP404XL current probe applied to magnetron
- Tektronix TCPA400 amplifier (coupled to TCP404XL)
- Tektronix TM502A current probe applied to sample holder
- Tektronix A6303 amplifier (coupled to TM502A)
- Tektronix PPE 4kV 100x voltage probe applied to Hüttinger 4001 output
- Tektronix PPE 4kV 100x voltage probe applied to sample holder
- Tektronix P6015 1000x voltage probe applied to Sinex 1.2 output

10.1.7 Thin film analysis instrumentation

- AFM DME dual scope 98-50
- SEM Tescan Vega 3 (LNL-INFN)
- FEI Quanta 3D FEG Dual-Beam (INRIM)
- AN2000 accelerator (60° scattering chamber and μ -beam scattering chamber LNL-INFN)

10.2 Binning software

Here is reported the software code that has been written for the time resolved OES analysis. The software create the OES-TR spectra from the .txt file generated by Caen Digitizer.

```
package tot3;

import java.io.BufferedReader;
import java.io.BufferedWriter;
import java.io.FileNotFoundException;
import java.io.FileReader;
import java.io.FileWriter;
import java.io.IOException;
import java.util.StringTokenizer;
import javax.swing.JOptionPane;

public class Tot3 {

    static int bit_clock=8;
    static int bina[]=new int [32];
    static String file0;
    static String file1;
    static String cartella;
```

```
static String cartella2;
static int soglia_amp=55;
static evento0 vet_event0[];
static evento1 vet_event1[];
static elem_x_bin ampiezza[];
static elem_x_bin binny[];
static elem_x_bin binny_cont[];
static elem_x_bin molty[];
static int valori0[];
static int valori1[];
static double tempo_impulso=0;
static double frequenza=48;
static double primo_trigger=0;
static double ultimo_trigger=0;
static int shift=-100;
static int bin_t=2; //ampiezza bin
static int inizio_bin=0; // bin
static int fine_bin=500; // bin
static int indice_primo_trigger;
static int numero_picchi_scartati;
static int numero_picchi_originali;
static int numero_picchi_processati;
static int numero_trigger_processati;
static int numero_trigger_originali;
static int numero_doppio_trigger_eliminati;
static double time_ultimo_trigger;
static double time_primo_trigger;

public static void main(String[] args) throws IOException{
    soglia_amp=130;
    cartella
="C:\\Users\\NORCIA\\Desktop\\WaveDump\\bin\\mo_sinex\\";
    cartella2
="C:\\Users\\NORCIA\\Desktop\\WaveDump\\bin\\mo_sinex\\";
    file0="prova109_wave0.txt";
    file1="prova109_wave1.txt";
```

```

    complex();
}

private static void complex() throws IOException{
    cancella_variabili();
    calcola_tempo_impulso();
    String percorso_file0=cartella+file0;
    String percorso_file1=cartella+file1;
    BufferedReader wave0 = new BufferedReader( new
FileReader(percorso_file0));
    BufferedReader wave1 = new BufferedReader( new
FileReader(percorso_file1));
    double cont=apri_prima(percorso_file0);
    vet_event0=new evento0[(int)cont];
    vet_event1=new evento1[(int)cont];
    crea_vettore_eventi(wave0,wave1);
        correggi_falsi_tr1();
    azzera_time_wave0();
    azzera_time_wave0_continuo();
    crea_binning_ampiezza();
    crea_binning_isto();
    crea_binning_molteplicita();
    calcola_ampiezza();
    int sogliola=sogliola_amp;
    correggi_picchi(sogliola);
    primo_ultimo_trigger();
    binning_continuo(sogliola);
    BufferedWriter c1_2 = new BufferedWriter( new
FileWriter(cartella2+"binning_"+sogliola+"mV_"+file0));
    stampa_bin(c1_2);
}

public static double apri_prima(String percorso){
    int cont=0;
    double event=0;
    try {

```

```

try ( BufferedReader fis = new BufferedReader( new
FileReader(percorso)) ) {
    String line=fis.readLine();
    StringTokenizer stT;
    String st;
    while(line!=null){
        stT = new StringTokenizer(line, ":", "\\t\\r\\n");
        st=stT.nextToken();
        if(st.compareTo("Event")==0){
            st=stT.nextToken();
            st=stT.nextToken();
            event=Double.parseDouble(st);
        }
        cont++;
        line=fis.readLine();
    }
    fis.close();
}
}
catch (FileNotFoundException e)
{OptionPane.showMessageDialog(null, "pd1"+cont+" "+event);}
catch (IOException e) {OptionPane.showMessageDialog(null,
"pd2"+cont);}
return event;
}
public static void crea_vettore_eventi(BufferedReader
fis2,BufferedReader fis3) throws IOException{//String percorso}{
    String line=fis2.readLine(); StringTokenizer stT; String st;
    String line3=fis3.readLine(); StringTokenizer stT3; String st3;

    for(int i=0; i<vet_event0.length;i++){
        vet_event0[i]=new evento0();
        vet_event0[i].crea_picco();
        vet_event1[i]=new evento1();
        //vet_event1[i].crea_picco();
        stT = new StringTokenizer(line, ":", "\\t\\r\\n");

```

```
st=stT.nextToken();
    stT3 = new StringTokenizer(line3, ":", "\\t\\r\\n");
st3=stT3.nextToken();

    if(st.compareTo("Record")==0){
//-----blocco_inizializzazione_wave0
        st=stT.nextToken();st=stT.nextToken();
        vet_event0[i].record_length =Integer.parseInt(st);
        valori0=new int [vet_event0[i].record_length];

line=fis2.readLine();line=fis2.readLine();line=fis2.readLine();
        stT = new StringTokenizer(line, ":", "\\t\\r\\n");

st=stT.nextToken();st=stT.nextToken();st=stT.nextToken();//event
        vet_event0[i].event_number=Double.parseDouble(st);
        line=fis2.readLine();line=fis2.readLine();
        stT = new StringTokenizer(line, ":", "\\t\\r\\n");

st=stT.nextToken();st=stT.nextToken();st=stT.nextToken();st=stT.nextToker
n();

vet_event0[i].time_tag_originale=correggi(Double.parseDouble(st));
        line=fis2.readLine(); //DC offset
        for(int j=0;j<vet_event0[i].record_length;j++){
            line=fis2.readLine();
            stT = new StringTokenizer(line, ":", "\\t\\r\\n");
            st=stT.nextToken();
            valori0[j]=Integer.parseInt(st);
        }
//-----fine blocco_inizializzazione_wave0
        analisi_vettore0(i);

//-----blocco_inizializzazione_wave1
        st3=stT3.nextToken();st3=stT3.nextToken();
        vet_event1[i].record_length =Integer.parseInt(st3);
        valori1=new int [vet_event1[i].record_length];
```

```
line3=fis3.readLine();line3=fis3.readLine();line3=fis3.readLine();
    stT3 = new StringTokenizer(line3, ":\t\r\n");

st3=stT3.nextToken();st3=stT3.nextToken();st3=stT3.nextToken();//event
    vet_event1[i].event_number=Double.parseDouble(st3);
    line3=fis3.readLine();line3=fis3.readLine();
    stT3 = new StringTokenizer(line3, ":\t\r\n");

st3=stT3.nextToken();st3=stT3.nextToken();st3=stT3.nextToken();st3=stT3.
nextToken();

vet_event1[i].time_tag_originale=correggi(Double.parseDouble(st3));
    line3=fis3.readLine();
    for(int j=0;j<vet_event1[i].record_lenght;j++){
        line3=fis3.readLine();
        stT3 = new StringTokenizer(line3, ":\t\r\n");
        st3=stT3.nextToken();
        valori1[j]=Integer.parseInt(st3);
    }
//-----fine blocco_inizializzazione_wave0
    analisi_vettore1(i);
}
    line=fis2.readLine();
    line3=fis3.readLine();
}
    fis2.close();
    fis3.close();
}

public static void calcola_tempo_impulso(){
    tempo_impulso=1000/frequenza;
    tempo_impulso=tempo_impulso-1;
    tempo_impulso=tempo_impulso*1000*1000;
}
```

```
public static void analisi_vettore0(int index){
    int var=1000;
    double sx=0;
    double dx=0;
//trova massimo picco
    for(int v=0;v<valori0.length;v++){
        if(var>valori0[v]){
            var=valori0[v];
        }
    }
    vet_event0[index].max=var;
//trova media sinistra e destra
    for(int v=0;v<5;v++){
        sx=sx+valori0[v];
    }
    sx=sx/5;
    vet_event0[index].media_sx=sx;
    for(int v=valori0.length-5; v<valori0.length;v++){
        dx=dx+valori0[v];
    }
    dx=dx/5;
    vet_event0[index].media_dx=dx;
//trova setta baseline
    double media=0;
    double diff=Math.abs(dx-sx);
    if(diff<(dx/100)){
        media=((dx+sx)/2);
    }else{
        media=Math.max(dx, sx);
    }
    vet_event0[index].base_line=media;
    int numero_picco=0;
    for(int i=3;i<valori0.length-3;i++){
//cerca picchi multipli
//soglia rumore 5% della media
        if(valori0[i]<((int)media-((int)media/100*5))){
```

```
        if(valori0[i]<valori0[i-3]){
            if(valori0[i]<valori0[i+3]){
                vet_event0[index].pic[numero_picco].massimo=valori0[i];
                vet_event0[index].pic[numero_picco].posizione=i;
                numero_picco++;
                i=i+2;
            }
        }
    }
}
vet_event0[index].multiplo=(numero_picco);
//fine picchi multipli
//
//calcolo delle retivate
for(int i=0;i<valori0.length;i++){
}
}
public static void analisi_vettore1(int index){
    int soglia=700;
    //boolean flag=true;
    for(int i=0;i<valori1.length;i++){
        if(valori1[i]>soglia){
            vet_event1[index].trigger1=true;
            vet_event1[index].index_trigger1=i;
            vet_event1[index].tempo=i;
            i=valori1.length;
            numero_trigger originali++;
        }
    }
    double sx=0;
    double dx=0;
    for(int v=0;v<5;v++){
        sx=sx+valori1[v];
    }
    sx=sx/5;
    vet_event1[index].media_sx=sx;
```

```
for(int v=valori1.length-5; v<valori1.length;v++){
    dx=dx+valori1[v];
}
dx=dx/5;
vet_event1[index].media_dx=dx;
}

private static void correggi_falsi_tr1(){
    for(int i=0;i<vet_event1.length-2;i++){
        if(vet_event0[i].time_tag_continuo<0){
            vet_event0[i].trigger1=false;
        }
        if(vet_event1[i].trigger1){
            if(vet_event1[i+1].trigger1){
                vet_event1[i+1].trigger1=false;
                vet_event1[i+2].trigger1=false;
                numero_doppio_trigger_eliminati++;
            }/*
            if(vet_event1[i].event_number<ultimo_trigger){
                int j=0;
                while(vet_event1[i+j].time_tag_continuo-
vet_event1[i].time_tag_continuo<20000000){
                    vet_event1[i+j].trigger1=false;
                    j++;
                }
            }*/
        }
    }
}

private static void azzera_time_wave0(){

    String str="";
    int conti_v=0;
    for(int i=0; i<vet_event1.length;i++){
        if(vet_event1[i].trigger1){
```

```

        conti_v++;
    }
}
wave1_true veri1[] = new wave1_true[conti_v+5];
int as=0;
for(int i=0;i<vet_event1.length;i++){
    if(vet_event1[i].trigger1){
        veri1[as]=new wave1_true();
        veri1[as].event_n=vet_event1[i].event_number;
        veri1[as].tempo0=vet_event1[i].time_tag_originale;
        as++;
    }
}
for(int i=0; i<conti_v-1;i++){
    double prece=veri1[i].event_n;
    double succe=veri1[i+1].event_n;
    double tempo_di_0=veri1[i].tempo0;

    for(int j=0;j<(succe-prece);j++){
        vet_event0[j+(int)prece].time_tag_azzerato_teo =
vet_event0[j+(int)prece].time_tag_originale - tempo_di_0;

vet_event1[j+(int)prece].time_tag_azzerato_teo=vet_event0[j+(int)prece].ti
me_tag_azzerato_teo;
    }
}
}
}

private static void cancella_variabili(){
    indice_primo_trigger=0;
    primo_trigger=0;
    ultimo_trigger=0;
    numero_picchi_scartati=0;
    numero_picchi_originali=0;
    numero_picchi_processati=0;
    numero_trigger_processati=0;
}

```

```

numero_trigger originali=0;
numero_doppio_trigger_eliminati=0;
time_ultimo_trigger=0;
time_primo_trigger=0;
}

private static void azzera_time_wave0_continuo(){
    for(int i=0; i<vet_event0.length;i++){
        vet_event0[i].time_tag_continuo=vet_event0[i].time_tag_originale;
    }
    double precedente=0;
    for(int i=0; i<vet_event0.length-1;i++){

if(vet_event0[i].time_tag_originale>vet_event0[i+1].time_tag_originale){
        precedente=vet_event0[i].time_tag_continuo;
    }

vet_event0[i+1].time_tag_continuo=vet_event0[i+1].time_tag_continuo+pre
cedente;

vet_event1[i+1].time_tag_continuo=vet_event0[i+1].time_tag_continuo;
    }
}

private static void calcola_ampiezza(){
    for(int i=0; i<vet_event0.length;i++){
        vet_event0[i].trigger1=vet_event1[i].trigger1;
    }
    for(int i=0; i<vet_event0.length;i++){
        for(int j=0; j<vet_event0[i].pic.length;j++){
            if(vet_event0[i].pic[j].massimo!=-1){
                vet_event0[i].pic[j].ampiezza
                =
Math.abs(vet_event0[i].pic[j].massimo-vet_event0[i].base_line);
                numero_picchi originali++;
            }
        }
    }
}

```

```

    }
}

private static void correggi_picchi(int sogliola){
    for(int i=0; i<vet_event0.length;i++){
        for(int j=0; j<vet_event0[i].pic.length;j++){
            if(vet_event0[i].pic[j].ampiezza<sogliola){
                if(vet_event0[i].pic[j].ampiezza!=
1){numero_picchi_scartati++;vet_event0[i].multiplo--;}
                vet_event0[i].pic[j].ampiezza= -1;
                vet_event0[i].pic[j].massimo= -1;
                vet_event0[i].pic[j].posizione=-1;
            }
            vet_event0[i].pic[j].ampiezza
Math.abs(vet_event0[i].pic[j].massimo-vet_event0[i].base_line);
        }
    }
    //correggi_molty();
}

private static void crea_binning_ampiezza(){
    int passo=5;
    int inizio=0;
    int fine=500;
    int numero_intervalli=(fine-inizio)/passo;
    ampiezza=new elem_x_bin[numero_intervalli];
    for(int i=0;i<ampiezza.length;i++){
        ampiezza[i]=new elem_x_bin();
    }
    for(int i=0;i<ampiezza.length;i++){
        ampiezza[i].estremo_inf=(inizio+i*passo);
        ampiezza[i].estremo_sup=(inizio+passo+i*passo);
    }
}

private static void crea_binning_molteplcita(){

```

```
int passo=1;
int inizio=0;
int fine=50;
int numero_intervalli=(fine-inizio)/passo;
moly=new elem_x_bin [numero_intervalli];
for(int i=0;i<moly.length;i++){
    moly[i]=new elem_x_bin();
}
for(int i=0;i<moly.length;i++){
    moly[i].estremo_inf=(inizio+i*passo);
    moly[i].estremo_sup=(inizio+passo+i*passo);
}
}

private static void crea_binning_isto(){
    int numero_intervalli=(int)((fine_bin-inizio_bin)/bin_t);
    binny=new elem_x_bin[numero_intervalli];
    binny_cont=new elem_x_bin[numero_intervalli];
    int passo=bin_t;
    for(int i=0;i<binny.length;i++){
        binny[i]=new elem_x_bin();
        binny_cont[i]=new elem_x_bin();
    }
    for(int i=0;i<binny.length;i++){
        binny[i].estremo_inf=((inizio_bin+i*passo)+shift);
        binny[i].estremo_sup=(inizio_bin+passo+i*passo+shift);
        binny_cont[i].estremo_inf=((inizio_bin+i*passo)+shift);
        binny_cont[i].estremo_sup=(inizio_bin+passo+i*passo+shift);
    }
}

private static void binning_ampiezza(double value){
    for(int j=0; j<ampiezza.length;j++){
        if(value>=ampiezza[j].estremo_inf){
            if(value<ampiezza[j].estremo_sup){
                ampiezza[j].contatore_picchi++;
            }
        }
    }
}
```

```

    }
  }
}

private static void binning_molteplicità(double value){
  for(int j=0; j<molty.length;j++){
    if(value>=molty[j].estremo_inf){
      if(value<molty[j].estremo_sup){
        molty[j].contatore_picchi++;
      }
    }
  }
}

private static void binning_continuo(int soglia_ampiezza){
  double scarto_inf=Math.abs(shift*1000);
  double scarto_sup=fine_bin*1000;
  //int primo=0;
  //if(primo_trigger==0){
  //  primo=1;
  //}else {primo=0;}
  for(int i=(int)primo_trigger+1; i<vet_event0.length-1; i++){
    if(vet_event0[i].event_number<ultimo_trigger){
      if(vet_event0[i].trigger1){
        numero_trigger_processati++;
        int j=0;
        while((Math.abs(vet_event0[i].time_tag_continuo-vet_event0[i-
j].time_tag_continuo)<scarto_inf){
          //if(vet_event0[i-j]!=null){
            vet_event0[i-j].trigger_cont=true;
            vet_event0[i-j].time_tag_continuo_shift=vet_event0[i-
j].time_tag_continuo-vet_event0[i].time_tag_continuo;
            j++;
          //}
        }
      }
    }
  }
}

```

```

        int z=0;
        while(Math.abs(vet_event0[i].time_tag_continuo-
vet_event0[i+z].time_tag_continuo)<scarto_sup){
            if(vet_event0[i+z]!=null){
                vet_event0[i+z].trigger_cont=true;

vet_event0[i+z].time_tag_continuo_shift=vet_event0[i+z].time_tag_continuo-
o-vet_event0[i].time_tag_continuo;
                z++;
            }else{
                scarto_sup=-1;
            }
        }
    }
}
}
for(int i=0;i<vet_event0.length;i++){
    if(vet_event0[i].trigger_cont){
        for(int j=0; j<binny_cont.length;j++){

if(vet_event0[i].time_tag_continuo_shift>binny_cont[j].estremo_inf*1000){

if(vet_event0[i].time_tag_continuo_shift<binny_cont[j].estremo_sup*1000)
{
            if(vet_event0[i].multiplo>0){
                binny_cont[j].contatore_picchi++;
                binning_molteplicità(vet_event0[i].multiplo);
                for(int z=0;z<vet_event0[i].pic.length;z++){
                    if(vet_event0[i].pic[z].ampiezza>=soglia_ampiezza){
                        if(vet_event0[i].pic[z].posizione>0){
                            binny_cont[j].contatore_picchi_multi++;

binning_ampiezza(vet_event0[i].pic[z].ampiezza);

                                numero_picchi_processati++;

```

```
    }
    }
    }
    }
    }
    }
    }
}

private static void correggi_molto(){
    int cella=0;
    for(int i=0; i<vet_event0.length; i++){
        cella=0;
        for(int j=0; j<vet_event0[i].pic.length;j++){
            if(vet_event0[i].pic[j].ampiezza!=-1){
                cella++;
            }
        }
        vet_event0[i].multiplo=cella;
    }
}

private static int max_molt(){
    int moltepli=0;
    for(int i=0; i<vet_event0.length; i++){
        if(moltepli<vet_event0[i].multiplo){
            moltepli=vet_event0[i].multiplo;
        }
    }
    return moltepli;
}

private static void primo_ultimo_trigger(){
    //int j=0;
```

```
boolean flag=true;
while(flag){
    for(int i=0;i<vet_event0.length;i++){
        if(vet_event0[i].trigger1){
            if(flag){
                indice_primo_trigger=i;
                primo_trigger=vet_event0[i].event_number;
                time_primo_trigger=vet_event0[i].time_tag_continuo;

                if(time_primo_trigger>2*Math.abs(shift*1000)){
                    flag=false;
                }

            }
        }
    }
}
ultimo_trigger=0;
for(int i=0; i<vet_event0.length; i++){
    if(vet_event0[i].trigger1==true){
        ultimo_trigger=vet_event0[i].event_number;
        time_ultimo_trigger=vet_event0[i].time_tag_continuo;
    }
}

private static void stampa_bin(BufferedWriter b) throws IOException{
    String stampa_veri="";
    stampa_veri=stampa_veri+numero_trigger_processati+"\n";
    stampa_veri=stampa_veri+numero_trigger_originali:
    \t"+numero_trigger_originali+"\n";
    //stampa_veri=stampa_veri+"tempo           primo           trigger:
    \t"+time_primo_trigger+"\n";
    //stampa_veri=stampa_veri+"tempo           ultimo           trigger:
    \t"+time_ultimo_trigger+"\n";
```

```

        stampa_veri=stampa_veri+"numero          tot          eventi
\t"+vet_event0.length+"\n";
        stampa_veri=stampa_veri+"numero_trigger originali:
\t"+numero_trigger originali+"\n";

stampa_veri=stampa_veri+"numero_trigger_processati:\t"+numero_trigger_
processati+"\n";

stampa_veri=stampa_veri+"numero_doppio_trigger_eliminati:\t"+numero_d
oppio_trigger_eliminati+"\n";

stampa_veri=stampa_veri+"numero_picchi_processati:\t"+numero_picchi_p
rocessati+"\n";
        stampa_veri=stampa_veri+"molteplicità_max \t"+max_molt()+"\n";
        b.write(stampa_veri);
        b.flush();
        stampa_veri="\n";
        for(int i=0; i<binny.length;i++){
            //stampa_veri=stampa_veri+binny[i].estremo_inf+"\t";
            //stampa_veri=stampa_veri+binny[i].contatore_picchi+"\t";
            //stampa_veri=stampa_veri+binny[i].estremo_inf+"\t";

//stampa_veri=stampa_veri+binny[i].contatore_picchi_multi+"\t"+"t";

            //stampa_veri=stampa_veri+binny_cont[i].estremo_inf+"\t";
            //stampa_veri=stampa_veri+binny_cont[i].contatore_picchi+"\t";
            stampa_veri=stampa_veri+binny_cont[i].estremo_inf+"\t";

stampa_veri=stampa_veri+binny_cont[i].contatore_picchi_multi+"\t";
        stampa_veri=stampa_veri+"\n";
        b.write(stampa_veri);
        b.flush();
        stampa_veri="";
    }
    b.close();
}

```

```
private static void stampa_ampi(BufferedWriter b) throws IOException{
    String stampa_veri="";
    for(int i=0; i<ampiezza.length;i++){
        stampa_veri=stampa_veri+ampiezza[i].estremo_inf+"\t";
        stampa_veri=stampa_veri+ampiezza[i].contatore_picchi+"\t";
        stampa_veri=stampa_veri+"\n";
        b.write(stampa_veri);
        b.flush();
        stampa_veri="";
    }
    b.close();
}

private static void stampa_molty(BufferedWriter b) throws IOException{
    String stampa_veri="";
    int tot=0;
    for(int i=0; i<molty.length;i++){
        stampa_veri=stampa_veri+molty[i].estremo_inf+"\t";
        stampa_veri=stampa_veri+molty[i].contatore_picchi+"\t";
        tot=tot+molty[i].contatore_picchi;
        stampa_veri=stampa_veri+"\n";
        b.write(stampa_veri);
        b.flush();
        stampa_veri="";
    }
    stampa_veri="\ntotale picchi:"+ tot;
    b.close();
}

private static void stampa0_tempi(BufferedWriter b) throws
IOException{
    String stampa_veri= "event_number"+"\\t"+
        "time_tag_ori"+"\\t"+
        "time_tag_teo"+"\\t"+
        "time_tag_cont"+"\\t"+
        "time_tag_cont_sh"+"\\t"+
```

```

        "trigger_vero"+"\\t"+
        "trigger_cont"+"\\t"+
        "\\n";
//b.write(stampa_veri);
//b.flush();
//stampa_veri="";
for(int i=0; i<vet_event0.length;i++){
    stampa_veri=stampa_veri+vet_event0[i].event_number+"\\t";
    stampa_veri=stampa_veri+vet_event0[i].time_tag_originale+"\\t";
    stampa_veri=stampa_veri+vet_event0[i].time_tag_azzerato_teo+"\\t";
    stampa_veri=stampa_veri+vet_event0[i].time_tag_continuo+"\\t";

stampa_veri=stampa_veri+vet_event0[i].time_tag_continuo_shift+"\\t";
    stampa_veri=stampa_veri+vet_event0[i].trigger1+"\\t";
    stampa_veri=stampa_veri+vet_event0[i].trigger_cont+"\\t";
    stampa_veri=stampa_veri+"\\n";
    b.write(stampa_veri);
    b.flush();
    stampa_veri="";
}
b.close();
}

private static void stampa0_picchi(BufferedWriter b) throws
IOException{
    String ss="enent\\t"+
        "time_tag_continuo_shift"+"\\t"+
        "multiplo"+"\\t"+
        "trigger_cont"+"\\t"+
        "base_line"+"\\t"+
        "media_sx"+"\\t"+
        "media_sx"+"\\t";
    for(int i=0;i<vet_event0[1].pic.length;i++){
        ss=ss+"pic("+i+")_pos"+"\\t"+"\\t"+
            "pic("+i+")_amp"+"\\t"+
            "pic("+i+")_max"+"\\t";
    }
}

```

```

String stampa_veri= ss+"\n";
//b.write(stampa_veri);
//b.flush();
//stampa_veri="";
for(int i=0; i<vet_event0.length;i++){
    if(vet_event0[i].trigger_cont){
        stampa_veri=stampa_veri+vet_event0[i].event_number+"\t";

stampa_veri=stampa_veri+vet_event0[i].time_tag_continuo_shift+"\t";

stampa_veri=stampa_veri+vet_event0[i].time_tag_azzerato_teo+"\t";
        stampa_veri=stampa_veri+vet_event0[i].time_tag_originale+"\t";
        stampa_veri=stampa_veri+vet_event0[i].time_tag_continuo+"\t";

        stampa_veri=stampa_veri+vet_event0[i].multiplo+"\t";
        stampa_veri=stampa_veri+vet_event0[i].trigger_cont+"\t";
        stampa_veri=stampa_veri+vet_event0[i].base_line+"\t";
        stampa_veri=stampa_veri+vet_event0[i].media_sx+"\t";
        stampa_veri=stampa_veri+vet_event0[i].media_dx+"\t";

        for(int                                     j=0;
j<vet_event0[i].pic.length;j++){//vet_event0[i].pic.length
            if(vet_event0[i].pic[j].posizione!=-1){

stampa_veri=stampa_veri+(int)vet_event0[i].pic[j].posizione+"\t";

stampa_veri=stampa_veri+(int)vet_event0[i].pic[j].ampiezza+"\t";

stampa_veri=stampa_veri+(int)vet_event0[i].pic[j].massimo+"\t";
                }
            }
            stampa_veri=stampa_veri+"\n";
        }
    }
    b.write(stampa_veri);
    b.flush();
    stampa_veri="";

```

```

    }
    b.close();
}

private static void stampa1_statistica(BufferedWriter b) throws
IOException{
    String stampa_veri="";
    double precedente=0;
    for(int i=0; i<vet_event1.length-1;i++){
        if(vet_event0[i].multiplo>0){
            if(vet_event1[i].trigger1){

                stampa_veri=stampa_veri+vet_event1[i].event_number+"\t";

stampa_veri=stampa_veri+vet_event1[i].time_tag_originale+"\t";
                stampa_veri=stampa_veri+(vet_event1[i].time_tag_originale-
precedente)+"\t";
                stampa_veri=stampa_veri+(vet_event1[i].index_trigger1)+"\t";
                stampa_veri=stampa_veri+vet_event0[i].event_number+"\t";

stampa_veri=stampa_veri+vet_event0[i].time_tag_continuo_shift+"\t";
                stampa_veri=stampa_veri+vet_event0[i].multiplo+"\t";
                for(int j=0;
j<vet_event0[i].pic.length;j++){//vet_event0[i].pic.length
                    if(vet_event0[i].multiplo>0){
                        if(vet_event0[i].pic[j].posizione!=-1){

stampa_veri=stampa_veri+(int)vet_event0[i].pic[j].posizione+"\t";
stampa_veri=stampa_veri+(int)vet_event0[i].pic[j].ampiezza+"\t";
stampa_veri=stampa_veri+(int)vet_event0[i].pic[j].massimo+"\t";
                            }
                        }
                    }
                }
                stampa_veri=stampa_veri+"\n";
                precedente=vet_event1[i].time_tag_originale;
            }
            b.write(stampa_veri);

```

```
        b.flush();
        stampa_veri="";
    }
}
}
b.close();
}

private static void stampa1(BufferedWriter c) throws IOException{
    String stampa_veri= "event_number"+"\\t"+
        "time_tag_originale"+"\\t"+
        "time_tag_azzerato_teo"+"\\t"+
        "time_tag_continuo"+"\\t"+
        "picco_max"+"\\t"+
        "multiplo"+"\\t"+
        "trigger1"+"\\t"+
        "media_sx"+"\\t"+
        "media_dx"+"\\t"+
        "\\n";

    //b.write(stampa_veri);
    //b.flush();
    //stampa_veri="";
    for(int i=0; i<vet_event1.length;i++){
        stampa_veri=stampa_veri+vet_event1[i].event_number+"\\t";
        stampa_veri=stampa_veri+vet_event1[i].time_tag_originale+"\\t";
        stampa_veri=stampa_veri+vet_event1[i].time_tag_azzerato_teo+"\\t";
        stampa_veri=stampa_veri+vet_event1[i].time_tag_continuo+"\\t";
        stampa_veri=stampa_veri+vet_event1[i].max+"\\t";
        stampa_veri=stampa_veri+vet_event1[i].multiplo+"\\t";
        stampa_veri=stampa_veri+vet_event1[i].trigger1+"\\t";
        stampa_veri=stampa_veri+vet_event1[i].media_sx+"\\t";
        stampa_veri=stampa_veri+vet_event1[i].media_dx+"\\t";
        stampa_veri=stampa_veri+"\\n";
        c.write(stampa_veri);
        c.flush();
        stampa_veri="";
    }
}
```

```
    }
    c.close();
}

private static void stampa_trigger_w1(BufferedWriter b) throws
IOException{
    String stampa_veri="";
    for(int i=0; i<vet_event1.length;i++){
        if(vet_event1[i].trigger1){
            stampa_veri=stampa_veri+vet_event1[i].event_number+"\t";
            stampa_veri=stampa_veri+vet_event1[i].trigger1+"\t";
            stampa_veri=stampa_veri+vet_event1[i].time_tag_originale+"\t";
            stampa_veri=stampa_veri+vet_event1[i].time_tag_continuo+"\t";
            stampa_veri=stampa_veri+vet_event1[i].tempo+"\t";
            stampa_veri=stampa_veri+"\n"; b.write(stampa_veri);
            b.flush();
            stampa_veri="";
        }
    }
    b.close();
}

private static double binarioToIntero(){
    double valore=0;
    for(int i=0;i<bina.length;i++){
        valore= valore +(double)(bina[i]*(Math.pow(2,(i))));
    }
    valore=valore*bit_clock;//1000000000;
    return valore;
}

private static void interoToBinario(double num1){
    for (int i=0; i<bina.length-1; i++){
        //stampa_testa();
        bina[i]=(int)num1%2;
        num1=(int)Math.floor(num1/2);
    }
}
```

```
    }  
}  
private static double correggi(double nu){  
    interoToBinario(nu);  
    return binarioToIntero();  
}
```

```
package tot3;  
public class elem_x_bin {  
    double estremo_inf=-1;  
    double estremo_sup=-1;  
    int contatore_picchi=0;  
    int contatore_picchi_multi=0;  
    public void setta(double inf, double sup, int vall, int max){  
        estremo_inf=inf;  
        estremo_sup=sup;  
        contatore_picchi=vall;  
        contatore_picchi_multi=max;  
    }  
}
```

```
public class evento0 {  
    int record_lenght=0;  
    int numero_picchi=50;  
    int multiplo=0;  
    int index_trigger1=0;  
    double event_number=0;  
    double time_tag_originale=-1;  
    double time_tag_azzerato_teo=-1;  
    double time_tag_continuo=-1;  
    double time_tag_continuo_shift=-1;  
    double base_line=0;  
    double max=0;  
    double media_sx=0;  
    double media_dx=0;  
    boolean trigger1=false;  
    boolean trigger_cont=false;  
    picco pic[]=new picco[numero_picchi];
```

```
public void crea_picco(){
    for(int p=0;p<pic.length;p++){
        pic[p]=new picco();
    }
}
```

```
package tot3;
public class picco {
    int massimo=-1;
    int posizione=-1;
    double ampiezza=-1;
    double derivata_pos;
    double derivata_neg;
}
```

```
public class trigger_1 {
    boolean bool=false;
    double event_n=-1;
    double time=-1;
    double posizione_soglia=-1;
}
```

Publications on peer reviewed journals

- W. Raniero, G. Maggioni, G. Della Mea, M. Campostrini, S. Marigo, and M. Nardo: “Rutherford backscattering spectrometry (RBS) analysis of dichroic systems for optical application”, AIP Conference Proceedings 1530, Vol. 133 (2013), AIP Publishing.
- W. Raniero, M. Campostrini, G. Maggioni, G. Della Meaa, A. Quaranta: “Physical vapour deposition reactive magnetron sputtering for the production and application of dichroics in photovoltaic system with solar spectral splitting”, Applied Surface Science, Vol. 308, pp. 170–175 (2014), Elsevier.
- W. Raniero, G. Della Mea, M. Campostrini “Functionalization of surfaces with optical coatings produced by PVD magnetron sputtering”, Research Perspectives on Functional Micro- and Nanoscale Coatings, pp. 170-207 (2016), IGI-Global
- G. Gatti, A. Marcelli, B. Spataro, V. Dolgashev, J. Lewandowski, S.G. Tantawi, A.D. Yeremian, Y. Higashi, J. Rosenzweig, S. Sarti, C. Caliendo, G. Castorina, G. Cibin, L. Carfora, O. Leonardi, V. Rigato, M. Campostrini “X-band accelerator structures: On going R&D at the INFN” , Nuclear Inst. and Methods in Physics Research, A, Volume 829, pp. 206-212, (2016), Elsevier.

Participation to congresses, schools and workshops

- ION Beam Conference, INFN-LNL 2012.
- 14th International Conference on Plasma Surface Engineering (PSE) September, 15 -19, 2014, tutorial: “HiPIMS technology”, Garmisch-Partenkirchen, Germany.
- 14th ICNMTA (international Conference on nuclear microprobe technology and application) July, 3-4, 2014, Training course, Legnaro, Padova, Italy
- 14th ICNMTA (international Conference on nuclear microprobe technology and application) July, 6-11, 2014, Conference, Legnaro, Padova, Italy
- 3rd international SPES workshop, October 10-12, 2016, Workshop, Legnaro, Padova, Italy
- 7th HiPIMS conference, June, 27-28, 2016 SVC tutorials, Sheffield, England
- 7th HiPIMS conference, June, 29-30, 2016 SVC tutorials, Sheffield, England
- 16th International Conference on Plasma Surface Engineering (PSE) September, 17 -21, 2016, Conference Garmisch-Partenkirchen, Germany